Optimization of the CBM-RICH detector geometry and its use for the reconstruction of neutral mesons using conversion method

Dissertation

zur Erlangung des akademischen Grades eines
Doktors der Naturwissenschaften (Dr. rer. nat.)

der Fakultät Mathematik und Naturwissenschaften
Fachgruppe Physik
der Bergischen Universität Wuppertal

vorgelegt von
M. Sc. Ievgenii Kres
(aus der Ukraine)

January 2019

Die Dissertation kann wie folgt zitiert werden:

urn:nbn:de:hbz:468-20190408-114416-1
[http://nbn-resolving.de/urn/resolver.pl?urn=urn%3Anbn%3Ade%3Ahbz%3A468-20190408-114416-1]

1. Gutachter:
Prof. Dr. Karl-Heinz Kampert
Bergische Universität Wuppertal

2. Gutachter
Prof. Dr. Claudia Höhne
Justus-Liebig-Universität Gießen

Contents

List of Figures

List of Tables

Abstract

The reconstruction of photons is an essential task for modern heavy ion experiments, since they are emitted during the entire space-time evolution of the colliding system and they leave the medium unaffected. Reconstructed photons allow experimentalists to explore every single step of such an evolution. Since years the conversion analysis method is applied in modern experiments as ALICE or CMS to reconstruct particles decaying into photons. The obtained results show better resolution of particle reconstruction than direct measurements, but with much smaller efficiency. The large geometrical acceptance of the CBM detector allows to reconstruct particles decaying in photons as well.

There are two main sources of photons in heavy ion collisions: π^0 and η mesons. Those particles give the major background contribution to the measurements of rare dilepton decays of ρ, ω, and J/ψ, therefore it is very essential to reconstruct them with high precision.

The CBM-RICH detector is the main tool for the electron identification. Therefore, in this work, a geometry optimization of the RICH detector in the CBM experiment is studied first. In order to improve the electron identification of the converted lepton pairs a new cylindrically shaped geometry is proposed. The performance of the proposed geometry is compared to the default geometry using simulation of dilepton channels of ρ and ω mesons as signal events and π^0 decays as background events.

By using this proposed geometry the reconstruction efficiency of π^0 and η mesons using conversion analysis of photons with conversion in the target and in the detector material is studied. Different cut values for particle reconstruction are discussed and the most suitable cuts are suggested. Later on, obtained π^0 results are tested in order to extract the slope parameter from the transverse momentum spectrum of reconstructed particles. Received results are compared to the expected value from the UrQMD generator.

The reconstruction of η mesons using double conversion method requires data sample of large statistics. Due to the limited storage space, one can not manage sufficient statistics using the present simulation software framework. In this work several alternative ways of simulation are considered, which allow users to get high statistics simulation in conditions with a limited storage space. The obtained results from the η analysis show the ability of the CBM experiment to reconstruct η mesons via double conversion method from central Au+Au collisions.

1 Introduction

Since a long time ago people began to ask the question of origin of everything surrounding. The very first theoretical guesses appeared at 460 BC, when Democritus and his teacher Leucippus speculated that matter is composed of smallest indivisible units, atoms. After a long time the same idea was picked up again. In 1803 John Dalton suggested that all matter is composed of small indivisible particles, termed "atoms". With the help of experiments during the last century, in particular due to experiments by Rutherford, scientists discovered that the atom consists of electrons and a positively charged nucleus, containing most of the atomic mass. Making more and more researches they have found a large number of particles, today classified as hadrons. In the middle of the 20^{th} century the study of interactions of these particles by scattering and decays provided a new fundamental theory called Standard Model. According to this model all hadrons have an internal structure and thus they are not elementary particles. Hadrons, as well as their properties, could be explained as combinations of two or three quarks bound together with gluons [1].

According to present knowledge, quarks are considered as elementary particles. There are six quarks (see Figure 1.1), which are the smallest strongly interacting particles: up (u), down (d), charm (c), strange (s), bottom (b), and top (t).

In the Standard Model [2], at normal conditions, quarks and gluons can not be observed as free particles. This effect is known as confinement. The Quantum Chromodynamics (QCD) has predicted, that at certain conditions the confinement of quarks in hadrons vanishes, forming a new state of matter, the Quark-Gluon Plasma (QGP), where the quarks and gluons can move freely in the region where a QGP exists, on the scales larger than the size of hadrons (about 10^{-15} m). The nuclear matter under such extreme conditions may exist also nowadays in the interior of compact stellar objects like neutron stars.

To create this deconfined partonic matter, one needs to increase the energy density of the nuclear system above a certain critical energy density (E_c), where the average distance between quarks becomes sufficiently small (asymptotic freedom) so that confinement to nucleons disappears. There are several possible ways to achieve this: either by compressing cold nuclear matter, by heating the matter at zero net baryon density, or by compressing and heating matter at the same time. The heating process consists of increasing the temperature of the system, which can be achieved at high energy particle collisions. In the compressing mode, one tries to increase

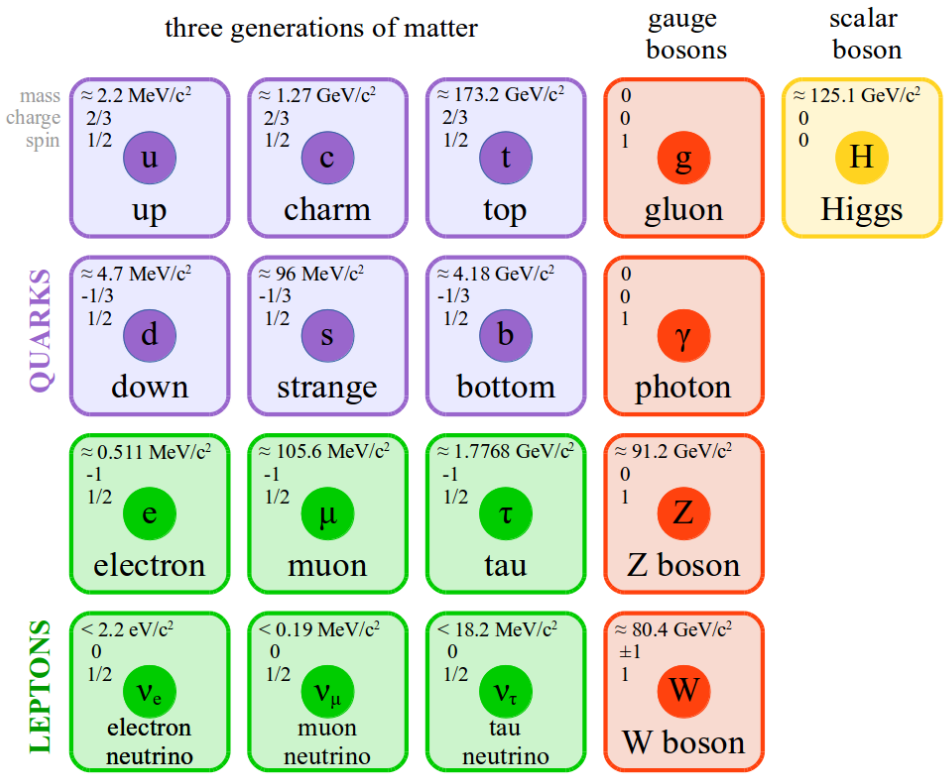

Figure 1.1: Schematic depiction of elementary particles in Standard model. Parameters of particles for the picture are taken from Particle Data Group 2018 [3].

the baryon number density in a given volume. High-energy heavy ion collision experiments provide the unique possibility to create and investigate these extreme states of matter, and address fundamental aspects of QCD.

In 1970 such conditions have been realized in heavy ion collisions at BEVALAC at the Lawrence Berkeley National Laboratory (LBNL) in Berkeley, USA. A group of about 30 physicists settled at the LBNL Bevatron-Bevalac facility to start exploitation of relativistic nucleus-nucleus collisions at fixed target energies ranging up to 2 GeV per nucleon (AGeV) [4].

A little bit later the Schwerionen-Synchrotron (SIS18) accelerator at GSI Helmholtz Centre for Heavy Ion Research in Darmstadt, Germany, started to operate as a fixed target experiment at energies up to 2 AGeV. They both discovered the collective flow of nucleons, and studied in detail the production of pions and strange particles. In particular the data on strangeness production at SIS18 provided evidence for a soft nuclear matter equation-of-state and for the modification of kaon properties in dense nuclear matter [5].

Later on, an experiment with fixed target was operated at BNL-AGS using gold beams of energies between 2 and 11 AGeV. The major achievement of these experiments at AGS was the measurement of the excitation of collective flow of protons as a probe of the equation-of-state of dense nuclear matter. Nowadays, the AGS is used as pre-accelerator for the Relativistic Heavy Ion Collider (RHIC) with a maximum energy for uranium ions of 200 AGeV [6].

Experiments at the SPS accelerator at the European Organization for Nuclear Research (CERN) in Geneva, Swiss, extended the list of hadrons observed in heavy ion collisions up to multi-strange hyperons due to his ability to reach energies between 10 and 160 AGeV with lead beams, and confirmed the picture of a chemically equilibrated fireball. Nowadays, it is also used as a pre-accelerator for the Large Hadron Collider (LHC) with a maximum energy for lead ions of 5.52 ATeV [7].

From theoretical considerations and according to transport simulations [8], the highest energies of LHC and RHIC do not allow to study a fireball with highest densities during the collision. The high energy density and large number of matter-antimatter pairs at these energies do not contribute to the net-baryon densities, and quickly dilute the system after creation. Highest densities of the fireball can only be accessed at lower energies. From these considerations the SIS18 experiment is currently being extended to the Facility for Antiproton and Ion Research (FAIR) at GSI in Darmstadt, Germany (see Figure 1.2).

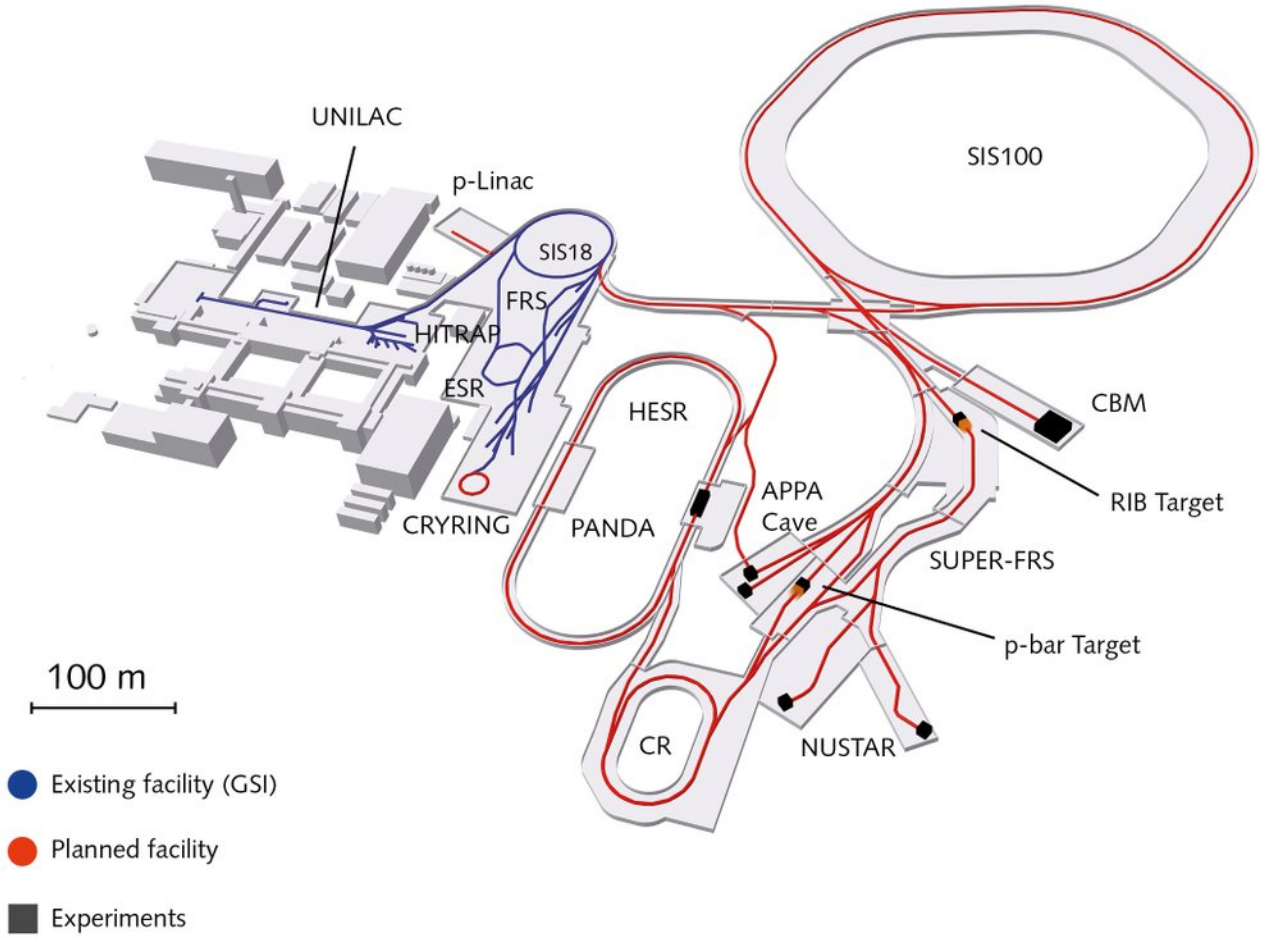

Figure 1.2: Layout of the Facility for Antiproton and Ion Research in Darmstadt. With blue lines the existing GSI facilities (UNILAC and SIS18 accelerators) are shown, and the red lines represent the new accelerator complex (e.g. superconducting synchrotron SIS100 and CBM experiment) [9].

The Compressed Baryonic Matter (CBM) experiment is designed for the investigation of strongly interacting matter under highest densities in heavy ion collisions. Suitable probes to investigate the properties of the created medium are, for example, dileptons, charmonium production, and hyperons. Some details about the physics and the detector itself are presented in the next chapters.

The work presented in this thesis aims at an optimization of the CBM Ring Imaging Cherenkov Detector (RICH) photon detection camera and its use in the reconstruction of π^0 and η mesons via their decay into $\gamma\gamma$ and further conversion of both γ in the target or in detector material into e^+e^- pairs. These leptons are identified using the CBM-RICH detector. The work describes optimal conditions for π^0 and η reconstruction, its use in the reconstruction of direct photons, and the possibility to derive the fireball temperature from these measurements.

1.1 Thesis outline

This thesis includes several chapters starting with an introductory part. The remaining chapters are organized in the following way:

- **Chapter 2** gives a short overview of the CBM experiment as a part of the FAIR facility, including its physics motivation, goals, and challenges. Some general overview of experiments and detector systems to be installed at FAIR is given.

- **Chapter 3** focuses on the conceptual design of the Ring Imaging Cherenkov detector of CBM. The description mentions technical details of the RICH, which are later referred to in the discussion of the optimization procedure.

- **Chapter 4** describes the optimization procedure for the position of Photo Multiplier Tubes. As a result, a new geometrical design of the PMT plane for the RICH detector is proposed.

- **Chapter 5** includes a short introduction to the CbmRoot framework used for the simulation, a basic description of the conversion method, and its use for the reconstruction of converted photons. Important aspects needed for the efficient reconstruction of signal with moderate background are discussed.

- **Chapter 6** shows the obtained results from the double conversion analysis for the π^0 reconstruction. The background in the resulting spectrum is estimated with the help of Event Mixing technique, and later on subtracted resulting in a background-subtracted spectrum of neutral pions. With help of MCtrue information the reconstruction efficiency of π^0 within the available acceptance is derived.

- **Chapter 7** covers the double conversion analysis of η meson reconstruction. Due to the low efficiency reconstruction of double conversion analysis and poor amount of η per event, the proper η analysis requires high statistics data. In this chapter, several methods to get high statistics are considered, also their advantages and disadvantages are discussed in details.

- **Chapter 8** checks the possibility to use the conversion method for the temperature estimation of the emitted source in the central Au+Au collision in the CBM experiment. This chapter describes analysis procedure to reconstruct transverse mass spectrum of π^0 and direct photons, which can be later on used for temperature estimation.

2 The CBM experiment

The CBM experiment, which will be located at FAIR in Darmstadt, is dedicated to explore the behavior of nuclear matter under conditions of high net baryonic densities and moderate temperatures. Among the main goals of CBM are the exploration of the first order deconfinement phase transition, the experimental validation of a critical point in the QCD phase diagram, and the study of the modifications of hadron properties in dense matter. These experimental discoveries would be a major breakthrough in our understanding of the properties of nuclear matter.

In this chapter a short description of the FAIR project and its main scientific objectives will be presented. Then will be described the research program of the CBM experiment, its main goals, and the various relevant observables. Later, the theoretical motivation of this work is given in relation to the research program of the experiment. Finally a focus will be put on the description of the CBM detector setup and its different components.

2.1 The FAIR facility

The CBM experiment will be one of several experiments at the FAIR facility. FAIR is a new accelerator complex currently under construction next to the GSI Helmholtz Centre for Heavy Ion Research in Darmstadt, Germany. The main focus of the FAIR research program is the basic investigation of the field of nuclear physics and atomic physics organized in four scientific pillars [10]:

- **APPA**

  The "Atomic, Plasma Physics and Applications" (APPA) pillar consists of several collaborations, who investigate plasma physics at high pressures and low temperatures, effects of radiation on materials and cells, and also includes material research.

- **CBM**

  The Compressed Baryonic Matter (CBM) experiment is designed for the investigation of highly compressed nuclear matter in order to search for a first order deconfinement phase

transition together with the critical point of the QCD phase diagram, and to study modifications of hadron properties in dense matter. More details about the physics and the detector itself are presented further down in this chapter.

- **NUSTAR**

  NUSTAR is devoted to studies of Nuclear Structure, Astrophysics, and Reactions. The research interest of the NUSTAR collaboration is focused on the use of beams of radioactive species separated and identified by the Superconducting Fragment Separator (SFRS), which will be built as part of the FAIR facility.

- **PANDA**

  The Proton Anti-Proton Annihilation at Darmstadt (PANDA) experiment is doing basic physics research on various topics around the weak and strong forces, exotic states of matter and the structure of hadrons.

A sketch of the FAIR facility is presented in Figure 1.2. The blue part corresponds to the present facility and the red one to the future installations. A detailed description of this new facility can be found in reference [11].

The heavy ion synchrotron SIS100 is the central part of the FAIR accelerator facilities. It has a circumference of 1084 meters. It is planned to build in future an additional synchrotron SIS300, which will be located in the same tunnel as SIS100. The difference between two synchrotrons is in magnetic rigidity of 100 Tm and 300 Tm respectively. The main motivation for the double synchrotron is the possibility for parallel operation of up to four research programs. This will ensure high beam availability for the experiments and in particular for CBM, for which this feature is extremely important. The research program will start with primary beams from the SIS100 synchrotron, and may be continued with beams from the SIS300 synchrotron. The beam intensity is up to 10^9 ions per second resulting in 10^7 interactions using a 1 % interaction probability in target. The minimal available ion beam energy is about 2 AGeV.

The available kinetic beam energy per nucleon (E/A) depends on the bending power, provided by dipole magnets, and can be calculated as [12]:

$$\frac{E}{A} = \sqrt{(0.3 \cdot B \cdot r \cdot \frac{Z}{A})^2 + m^2} - m, \tag{2.1}$$

where Z and A are charge and atomic number of the ion, $B \cdot r$ is the maximum beam rigidity, and m is the mass of the nucleon. For example, the gold ion ^{197}Au ($Z = 79$ and $A = 197$) at SIS100 will have a maximum energy of 11 GeV per nucleon while at SIS300 it can reach an energy up to 35 GeV per nucleon.

The possible beam energies for different ions are listed in Table 2.1.

2.2 Physics program of the CBM experiment

All nuclei at normal conditions are composed from protons and neutrons (i.e. nucleons) only. At higher temperatures and densities it is known, that nucleons are excited to short-lived states (baryonic resonances), which decay by the emission of mesons, and also baryon-antibaryon pairs are created. The mixture of baryons, antibaryons, and mesons is generally called hadronic matter. At very high temperatures or densities the hadrons melt. At this time quarks and gluons, from which hadrons are made, form a new phase: the Quark-Gluon-Plasma (partonic matter) [13]. The

Beam	Z	A	E/A in GeV SIS100	E/A in GeV SIS300
p	1	1	29	89
d	1	2	14	44
Ca	20	40	14	44
Ni	28	58	13.6	42
In	49	115	11.9	37
Au	79	197	11	35
U	92	238	10.7	34

Table 2.1: Ion species and their kinetic energy per nucleon for synchrotrons SIS100 and SIS300.

inverse process of melting into QGP happened in the universe during the first few microseconds after the Big Bang: the quarks and gluons were confined into hadrons.

Rolf Hagedorn, while studying the mass spectra of the discovered numerous hadronic resonant states, made a prediction, that hadrons dissolve into quarks and gluons above a temperature of about 160 MeV [14]. In this low density region of the phase diagram the transition is expected to be a smooth crossover from partonic to hadronic matter. For larger values of net-baryon densities (and for lower temperatures), one expects a phase transition from hadronic to partonic matter with a phase coexistence region in between. A new phase of so called quarkyonic matter has been proposed to exist beyond the first order phase transition at large baryon chemical potentials μ_B and moderate temperatures T. Effective model calculations suggest a critical endpoint at relatively large values of the baryon chemical potential [15], separating crossover from 1^{st} order phase transition. The illustration of possible phases of nuclear matter can be seen in Figure 2.1.

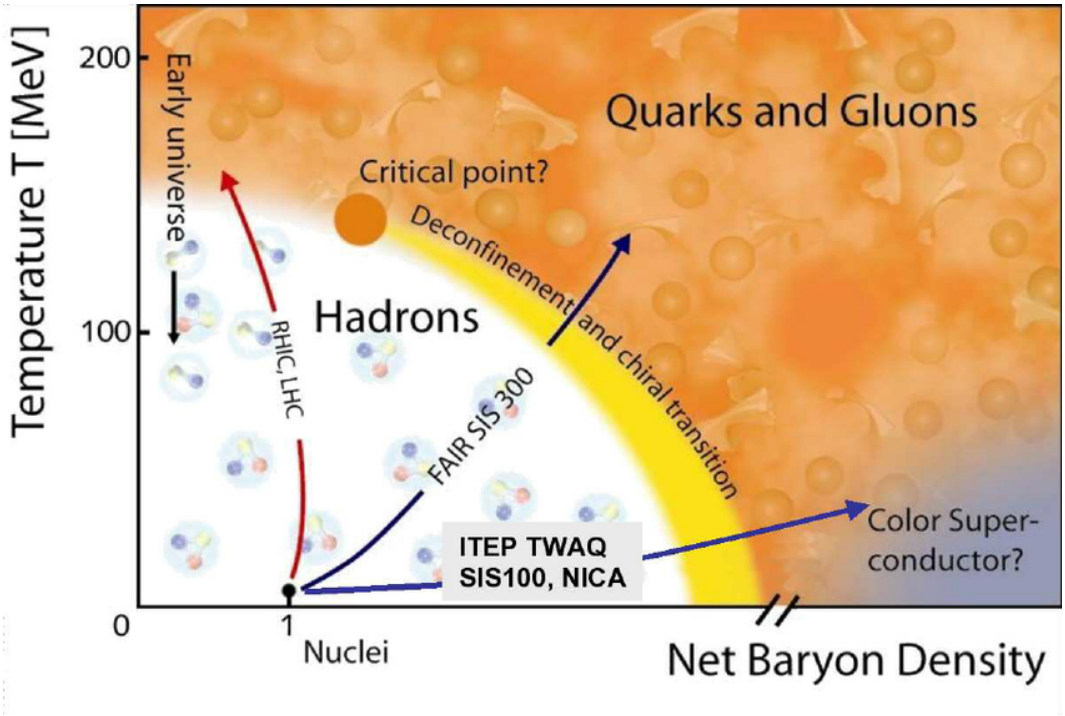

Figure 2.1: The illustration of possible phases of nuclear matter and their boundaries in a diagram of temperature T versus the net-baryon density ρ_B [10].

CBM is devoted to the exploration of the phase diagram of nuclear matter in the region of high net-baryon densities and moderate temperatures complementary to experiments at RHIC and

LHC, which aim to investigate the phase diagram at very high temperatures and nearly vanishing net-baryon densities. Heavy-ion beams in the energy range between 2 and 35 AGeV are ideally suited to explore the properties of dense baryonic matter.

According to analysis of particle yields in heavy-ion collisions the maximum net-baryon densities at freeze-out is reached at FAIR energies. This can be seen in Figure 2.2, where the chemical freeze-out line is shown as a function of temperature and net-baryon density. The chemical freeze-out line is depicted for Au+Au collisions. The numbers refer to beam energies in GeV per nucleon. The available energy at the RHIC collider (red solid squares) is expressed as a sum of the energy of each beam in the laboratory (from 2+2 to 100+100 AGeV). For FAIR (blue solid diamonds) the numbers refer to the kinetic energy of the incident beam on a fixed target.

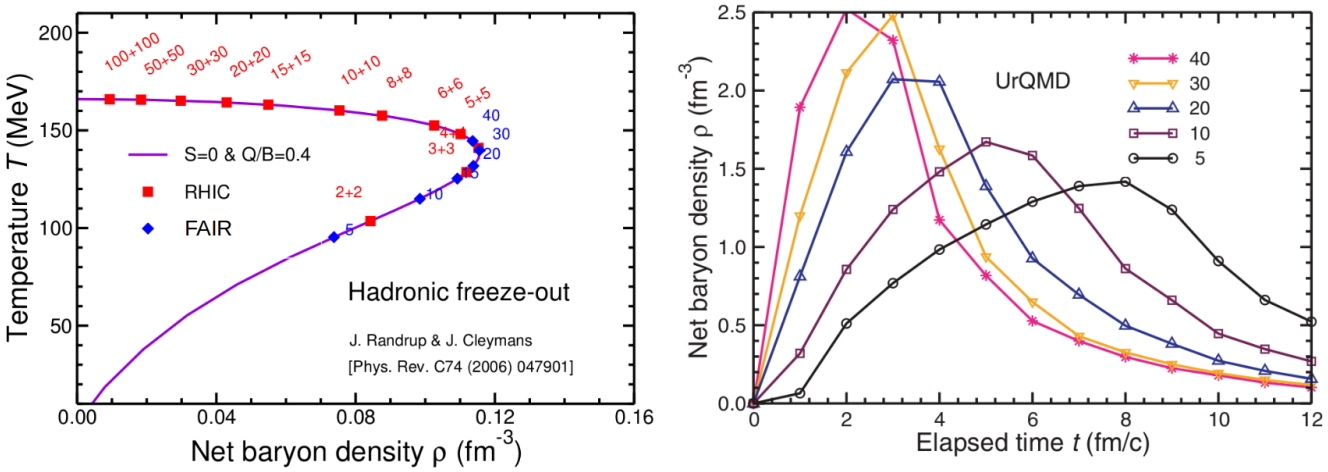

Figure 2.2: The hadronic freeze-out line in the plane of temperature versus net baryon density (left) [16] and the time evolution of the net baryon density versus time (right) [8] in a central Au+Au collision at various bombarding energies according to UrQMD model.

In this region CBM will search for the equation-of-state of QCD matter at densities similar to the densities in the core of neutron stars, a phase transition from hadronic to quark-gluon matter, a critical point of the QCD phase diagram, existence of quarkyonic matter, and signatures of chiral symmetry restoration.

The most promising observables to answer these questions are [12]:

- **Collective Flow:**

  In order to study collective flow and being sensitive to the effective degrees of freedom, one needs to study the directional distribution of particles, their distribution of energies and momenta. The measured Fourier coefficients (ν_1 is interpreted as directed flow, and ν_2 as elliptic flow) of emitted and identified (e.g. Kaon flow) particles can be interpreted in a context of a possible phase transition to the quark-gluon plasma.

- **Charm production:**

  Since CBM is focused on the measurements of diagnostic probes of the early and dense phase of the fireball evolution where hadrons containing charm quarks can be created, the relative abundance of such hadrons will be one of the key observables to be measured. At CBM energies, charm can only be produced in hard collisions at early stages of the fireball evolution. The charm production plays a particular role since charmonium (a bound state of $\bar{c}c$), D mesons (a bound state of a heavy c quark and a light quark), and charmed hyperons are created at beam energies close to the kinematic threshold. The production of hidden

charm (J/ψ) is expected to be sensitive to the properties of the created dense matter. The J/ψ suppression due to Debye color screening is generally considered as a signature of the QGP formation. The ratio between J/ψ and $(D + \bar{D})$ is often considered as a smoking gun signature for the formation of a QGP.

- **Multi-strange hyperons:**

  The yield, momentum, and angular distributions of multi-strange hyperons (baryons, which contain at least one strange quark: Λ, Σ, Ξ, and Ω) are interesting observables, which will be measured with CBM. The production of multi-strange hyperons at threshold energies, which is the case at the CBM energies, and at high densities is not yet completely understood.

- **Event-by-event fluctuations:**

  The search of non-statistical fluctuations via analysis of conserved quantities like baryon number, strangeness, electrical charge, particle yields, ratios, or kinematic properties is an important task of CBM. Such fluctuations have been predicted to occur, when the system passes through the first order deconfinement phase transition close to critical end point.

- **Low-mass vector mesons and their decays into dilepton pairs:**

  Short lived vector mesons can decay into dilepton pairs ($\rho, \omega, \phi \rightarrow e^+e^-$ and $\rho, \omega, \phi \rightarrow \mu^+\mu^-$), which interact with particles in the collision region only via electromagnetic interaction. Dileptons are emitted from the fireball during all stages of the collision. Those leptons do not further interact with the surrounding medium and, hence, carry information of the thermodynamical state of the medium at the moment of their production. From the invariant mass distribution of the dilepton pairs one can extract the in-medium spectral functions of the vector mesons, which contain information on the effect of chiral symmetry restoration.

- **Direct photons:**

  Another interesting observable are direct photons which leave the hot and dense medium unscathed. Thermal photons from the partonic phase are predicted to be the dominant source of direct photons at low transverse momenta in Au+Au collisions. Due to the very high interaction rate, the CBM experiment offers the possibility to measure the yield of thermal photons with high statistical accuracy. The experimental challenge is to extract a direct-photon signal above the large decay-photon background.

2.3 Importance of π^0, η, and direct γ reconstruction within the CBM physics context

Collisions of heavy ions make it possible to create and study in the laboratory strongly-interacting matter under extreme conditions. In such collisions the QGP is formed at the early stage of collision, when the system is very hot and dense. During the fireball evolution, the system dilutes and cools down. In different stages of cooling process different particles are formed and emitted (see Figure 2.3). Therefore, it is crucial to reconstruct emitted particles in order to get experimental access to the entire space-time evolution of the colliding system.

It was suggested, that studying QGP matter one can gain insight into the basic features of QCD matter in its normal state, namely, confinement and chiral symmetry breaking [17]. Ideal probes to study the created fireball in the collision are virtual photons and direct photons.

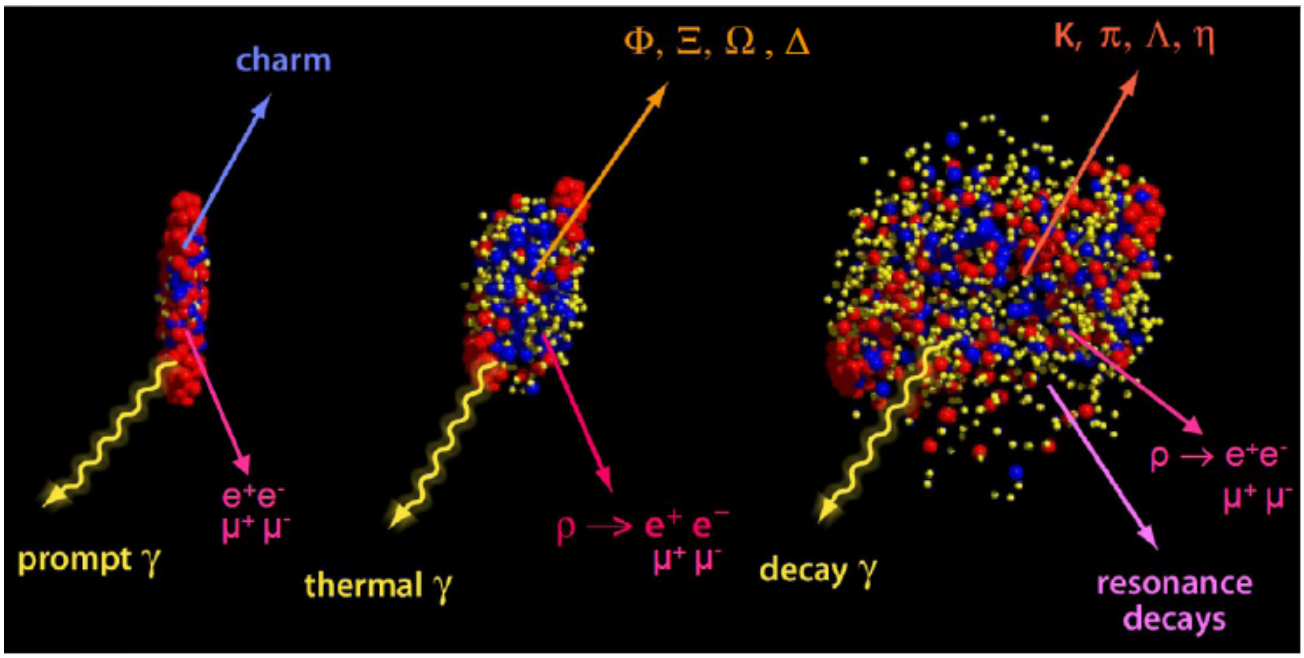

Figure 2.3: Schematic view of space-time evolution of the colliding system and its different stages, where different types of particles are produced [12].

In the quark-gluon plasma a quark and an antiquark can interact to form a virtual photon γ^*, which can then decay into a dilepton pair (i.e. $q + \bar{q} \rightarrow \gamma^* \rightarrow l^+ + l^-$). In addition to the annihilation of a quark-antiquark pair, there are other sources of dileptons: hadron-hadron interactions ($\pi^+ + \pi^- \rightarrow l^+ + l^-$), decays of hadronic resonances like ρ, ω, ϕ, and J/ψ, Drell-Yan processes populating different regions in the dilepton invariant mass spectrum. Leptons as well as photons have a large mean free path in comparison to the strongly interacting particles and thus provide an undistorted information about the environment in which they are produced. The dilepton measurements may provide information about lifetime and temperature of the created fireball [18], chiral symmetry restoration [19] via in-medium modification of spectral function [20], and charm suppression [21].

The dilepton measurement is characterized mainly by the invariant mass of the lepton pair, which is derived from 4-momenta of two particles:

$$m_{inv}^2 c^2 = (\boldsymbol{p}_{e^+} + \boldsymbol{p}_{e^-})^2 \tag{2.2}$$

Another important variable is the transverse momentum p_t. The combination of these two measured variables give access to the thermodynamic state of the medium at the moment of their production: 1) dileptons with a large invariant mass and high p_t are created when the temperature of the system is very high (early stages of the collision) 2) dileptons with smaller invariant masses and lower p_t are emitted when the temperatures of the system is low (late stages of the collision).

The experimental measurement of dileptons is challenging. First of all, leptons have to be clearly identified and separated from the large background of hadrons, mainly pions. Then, other sources of physical and combinatorial backgrounds have to be determined and subtracted from the invariant mass spectrum. A schematic view of a dilepton invariant mass spectrum can be seen in Figure 2.4.

The main sources of background to the dilepton spectrum in the low mass region are Dalitz decays of π^0 and η. Therefore, it is essential to determine the yield of these particles with high precision. The reconstruction of π^0 and η mesons is the main motivation of this thesis.

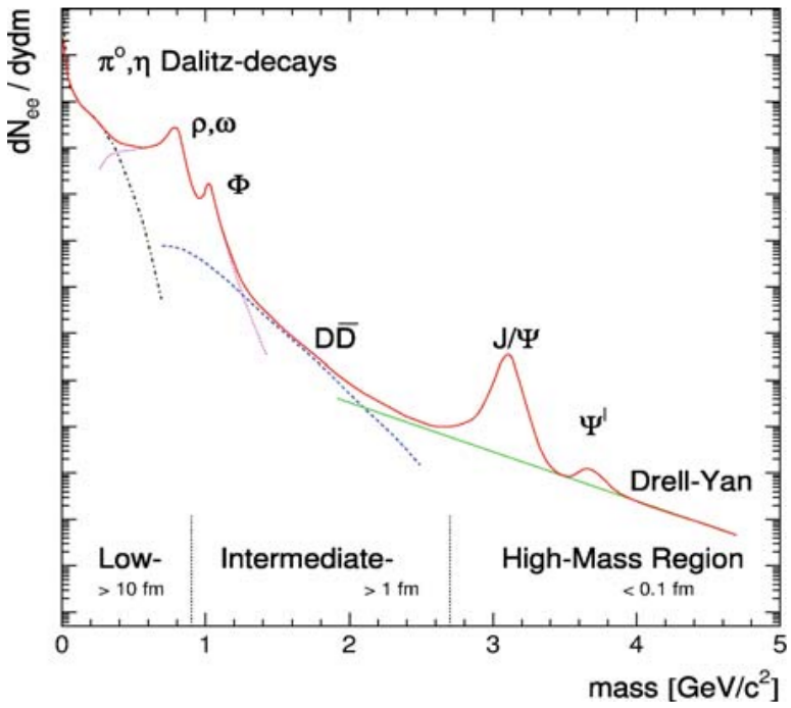

Figure 2.4: Schematic view of the expected sources of dilepton production as function of the invariant mass in relativistic heavy-ion collisions [22].

π^0 meson

The neutral pion has a special status in the family of elementary particles. It is the lightest strongly interacting particle observed in nature: $m_{\pi^0} = 134.97$ MeV. It was discovered in 1950 at the Berkeley synchrocyclotron by Bjorklund et al. [23], who measured the yield of γ-rays for protons incident on several nuclear targets. The π^0 was the first particle to be discovered with an accelerator and, therefore its discovery was an important milestone in the development of experimental particle physics.

According to the Particle Data Group (PDG) report [3] the particle mean life time equals to $\tau_{\pi^0} = 8.52 \times 10^{-17}$ s, what is far too short to measure by electronic means. Therefore, it is always reconstructed using its decay products.

The π^0 gives the biggest contribution to the background in the low mass region of the dilepton invariant mass spectrum. The main decay nodes of neutral pions are following:

(a) $\pi \rightarrow \gamma + \gamma$ 98.8 %

(b) $\pi \rightarrow e^+ + e^- + \gamma$ 1.2 %

The three body decay channel contributes to the dilepton invariant mass spectrum, therefore it is essential to count neutral pions with high precision. This channel, so called Dalitz decay, is performed through an intermediate state with an imaginary photon, which is decaying later in lepton-antilepton pair. In the CBM experiment it is impossible to separate imaginary photon from the real converted photon due to the detector accuracy and energy loss during the photon conversion, therefore both channels are reconstructed together.

Depending on the collision energy, it is expected to have $\sim 100-200\,\pi^0$ per one central Au+Au scattering event in CBM.

η meson

The η meson has been discovered in pion–nucleon collisions at the Bevatron in 1961 by A. Pevsner et al. [24] at a time when the proposal of the Eightfold Way was leading to predictions and discoveries of new particles from symmetry considerations. The η meson is associated with a wide variety of interesting nuclear and particle physics. It is a Goldstone boson, so this symmetry constrains its QCD dynamics. All its additive quantum numbers are zero: that includes the spin, isospin, electric charge, strangeness and other quark-flavor numbers, lepton number, baryon number and, therefore its decays are not influenced by a current changing the flavor.

The decay modes of the η meson are in particular interest by itself. All its possible strong decays are forbidden in lowest order: $\eta \to 2\pi$ and $\eta \to 4\pi^0$ by P and CP invariance, $\eta \to 3\pi$ because of G parity conservation as well as isospin and charge symmetry invariance [25]. First order electromagnetic η decays are forbidden as well: $\eta \to \pi^0\gamma$ by conservation of angular momentum, $\eta \to 2\pi^0\gamma$ and $\eta \to 3\pi^0\gamma$ by C invariance. Only $\eta \to \pi^+\pi^-\gamma$ occurs, but at a suppressed rate. The first allowed decay is the second-order electromagnetic transition $\eta \to \gamma\gamma$ [26].

Detailed studies of these decays may lead to "New Physics" that goes beyond the Standard Model, which has been successfully described a large fraction of physical processes, but does not explain such basic features as the existence of three families of fundamental fermions, the absence of the charge conjugates of the left-handed neutrinos and right-handed antineutrinos, or the origin of CP violation. Unfortunately, it is impossible to do these studies using only simulations and, therefore it is not a topic of this thesis.

The main decay channels of η meson together with their branching ratios from the most recent issue of the PDG report [3] are:

(a) $\eta \to \gamma + \gamma$ 38.8 %

(b) $\eta \to \pi^0 + \pi^0 + \pi^0$ 31.9 %

(c) $\eta \to \pi^+ + \pi^- + \pi^0$ 23.6 %

(d) $\eta \to \pi^+ + \pi^- + \gamma$ 4.88 %

(e) $\eta \to e^+ + e^- + \gamma$ 0.5 %

The PDG book presents many more decay channels, but due to their very low branching ratios they are not listed here. In addition, one can find there the mass of the particle $m_\eta = 547.85$ MeV together with a mean life time $\tau_\eta = 5 \times 10^{-19}$ s. Such relatively short life time means that particle will decay immediately after its formation. Therefore, the only way to reconstruct η meson is to use its decay products.

The Dalitz decay of η meson is the second biggest background contribution in the dilepton invariant mass spectrum, although the probability to have such decay is quite small. Therefore, this background must be determined through independent measurements of η mesons.

The η meson was already measured in other heavy ion experiments but only at much higher energies. Some experiments also tried to reconstruct η mesons at low energies, but the result was not achieved due to lack of statistics. Currently, the data obtained about η mesons from high energy experiments is fitted and extrapolated to the low energy region. The CBM experiment with its high interaction rate capability may clarify the correctness of such extrapolation. The extrapolation shows, that in central Au+Au collision at CBM energies it is expected to have $\sim 5 - 15$ η mesons per event depending on the collision energy.

Direct photons

Direct photons have long been considered as an essential probe of the dynamics in heavy ion collisions. The term "direct photons" stands for the photons which emerge directly from a particle collision. They can be classified into different categories depending on their origin from different stages of the expanding fireball formed after the collision.

During the early phase of the fireball evolution photons are produced by quark gluon Compton scattering processes and quark anti-quark annihilation processes [22]. They are defined as *prompt* photons. The following scattering and annihilation processes with photon emission are most abundant:

- $q + g \rightarrow \gamma + q$,
- $q + \overline{q} \rightarrow \gamma + g$,
- $q + \overline{q} \rightarrow \gamma + \gamma$,
- $g + g \rightarrow \gamma + \gamma$,
- $g + g \rightarrow \gamma + g$,

where q refers to any flavor of quarks, and g refers to gluons.

As the system expands quarks and gluons must hadronize, and these hadrons may undergo several scatterings and resemble for a while a hot hadronic gas. In this stage the *thermal* photon production reactions are happening. There are several dominant two-body reactions with photon emission:

- $\pi + \pi \rightarrow \rho + \gamma$
- $\pi + \rho \rightarrow \pi + \gamma$
- $\pi + \eta \rightarrow \pi + \gamma$
- $\pi + \pi \rightarrow \gamma + \gamma$

These photons will dominate in the spectrum at lower p_t (< 1 GeV/c). The first ever calculation of production of thermal photons from hadronic matter was performed by Kapusta et al. [28].

Photons arising from the electromagnetic interactions of the constituents of the plasma will provide information on the properties of matter at the time of their production. Since photons hardly re-interact in the produced medium, they form a relatively "clean" probe to study the QGP state. The combination of *promt* photons and *thermal* photons is usually called "***direct* photons**", since experimentally it is impossible to distinguish the difference between these sources.

However, in a heavy ion collision experiment, the detector captures all emitted photons including those from decays of final state hadrons. The measured spectrum is called the "*inclusive photon spectrum*". More than 90 % of photons in this spectrum are produced by hadron decays and are **not** categorized as *direct* photons. Therefore, measured photons from π^0 or η decays are called "*decay* photons", which must be subtracted from the inclusive photon spectrum in order to get a clean spectrum of *direct* photons. Subtraction of the decay background from inclusive photon spectrum, however, is a very challenging task due to missing experimental signature to distinguish them.

The *direct* photon spectrum can be used to infer the temperature of the system, evolution of the system size by intensity interferometry [29], momentum anisotropy of the initial partons [30] as well as formation time of the quark-gluon plasma [31] using elliptic flow of *direct* photons.

Temperature of the colliding system at different stages

In order to extract the properties of the produced matter different experimental observables are used to probe the dynamical evolution of the system and characterize the different stages of the collision. The temperature (T) of the colliding system in this case is one of the important parameters.

At ultra-relativistic energies ($E/m >> 1$) during the collision of the two nuclei dense gluon fields create a strongly-interacting medium, which then rapidly expands and very quickly thermalizes [32]. As the thermalized QGP continues to expand it cools down till its temperature decreases below the critical temperature of the QCD phase transitions T_c, at which point it hadronises and converts into a hadron-resonance gas. At this moment the composition of the produced particles is approximately fixed, at a temperature called the chemical freeze-out temperature (which is presumably close to the critical temperature of the phase transition). After the chemical freeze-out hadrons continue to interact. However, only their momentum distributions are modified as their relative energy is below the inelastic production threshold. At kinetic freeze-out, characterized by the kinetic freeze-out temperature, the medium is so dilute that the final state hadrons cease interacting and decouple. At this moment their momenta are fixed.

It is mostly from this final state that hadrons are measured in the experimental apparatus, from where one tries to deduce information about the initial state and the collision history, as it is not possible to detect directly the QGP. Spectra of measured particles produced in collisions of relativistic nuclei are usually displayed in "transverse" variables: transverse momentum $p_t = p \sin\theta$, where θ is the emission angle with respect to collision axis, or "transverse mass" $m_t = \sqrt{p_t^2 + m_0^2}$, where m_0 is the particle rest mass. Both these variables are Lorenz-invariant. The use of m_t is suggested by thermal emission models, which predict a simple exponential shape of spectra in m_t. Also, some experiments at colliders can measure identified particle spectra only in a narrow angular interval around the central value of rapidity, and thus the measured energy spectra are, in fact, the m_t spectra, as $E = \sqrt{p^2 + m_0^2} = \sqrt{p_l^2 + p_t^2 + m_0^2} \approx m_t$ for a small values of longitudinal momentum component p_l.

When combining spectra of m_t for several particles with different masses, it is convenient to replace m_t by $(m_t - m_0)$. When plotted in this variable, spectra of different particle species will begin at zero on the horizontal scale, and their slopes and detailed shapes can be well compared.

Spectra of produced particles are usually fitted with the formula:

$$\frac{1}{m_t^{3/2}} \frac{d\sigma}{dm_t} = C \exp[-(m_t - m_0)/T], \tag{2.3}$$

where the inverse slope parameter T is commonly called "temperature" of the emitting source [33].

The experimental data from the NA44 collaboration have shown the absent of a dependence of the inverse slope parameter T on the particle mass of the ejecta in p+p collisions [34]. At the same time their result identified the presence of such dependence in heavy ion collisions, and it becomes stronger with increasing masses of the colliding nuclei. This dependence is suggestive of a transversely expanding source. The relevant phenomenological model is called "blast wave" model [35], with the expansion velocity assumed to increase with the radius r: $\beta_T = \beta_s \, r/R_G$, where β_s is the velocity at the surface, and R_G is outer radius of the expanding fireball. Therefore, a fit to the experimental spectra gives an effective temperature (T_{eff}), which does not take into account radial expansion. Having the information about the evolution of the fireball one can extract the

thermal temperature (T_{th}) using formula:

$$T_{eff} = T_{th}\sqrt{\frac{1+ < \beta_T >}{1- < \beta_T >}} \tag{2.4}$$

The theoretical predictions distinguish several different stages for temperature measurement depending on measured particles:

- *Initial temperature*

  The initial temperature of an equilibrated QGP state can be estimated by studying electromagnetic probes, which do not interact strongly with the medium and, therefore carry information from the early stages of the collision. Information about initial temperature in the quark-gluon plasma can be derived from *prompt* photons. A recent discussion of theoretical aspects of photon production in high-energy nuclear collisions can be found in [36]. Measurements of direct photons are notoriously demanding. Their successful measurement can give information about the properties of matter on the earliest stages of nuclear-nuclear collisions.

- *Chemical freeze-out temperature*

  Assuming the simple statistical nature of the hadronization process and assuming further that the created medium is in thermodynamic equilibrium, thermal (statistical) models based on the grand canonical ensemble can be successfully employed to describe the particle abundances [37]. Within the framework of such models, the conditions at chemical freeze-out (where particle composition is fixed) can be determined from the measured particle yields and described by the fit parameters corresponding to the chemical freeze-out temperature (T_{ch}) and baryochemical potential (μ_B). Well suited candidates for such measurements are dilepton probes from ρ or J/ψ decays.

- *Kinetic freeze-out temperature*

  The kinetic freeze-out can be described by hydrodynamics-inspired blast-wave models. Such models allow experimentally to extract the associated temperature T_{kin} and the average transverse flow velocity β_T (reflecting the transverse expansion of the medium) from the low region in p_t spectra of identified charged hadrons. Usually for this type of measurement the spectra of π, K, p are used from almost zero p_t up to the highest possible p_t at midrapidity. Because of the common radial expansion velocity the p_t spectra of different particle species reflect the differences of their masses, which results in a characteristic mass ordering. The experimental results show the good agreement with hydrodynamic model calculations [38], which include viscous corrections and rescattering during the hadronisation phase.

2.4 The CBM detector system

The CBM physics program of measurement of rare probes imposes the need for very high beam intensities and long running periods. The aim of the CBM experiment is to operate the detectors at reaction rates up to 10 MHz with multiplicity up to 1000 charged particle in central Au+Au collisions. The technical challenge for the experiment is to identify all hadrons and leptons, and filter out interesting rare probes. The high interaction rate will induce problems of high particle flux and radiation hardness. Moreover, the high particle track multiplicity environment requires highly granular detectors.

The detectors have to be fast and radiation hard, provide efficient particle identification, provide high-resolution determination of decay vertices, and cover a large geometrical acceptance with full azimuthal coverage. The data acquisition system should be efficient and fast.

The above mentioned requirements should be fulfilled in a wide range of energies (2−45 AGeV) and for various system sizes (p+p, p+A, A+A) in order to achieve the physics goals of the experiment.

The CBM detector system has two detector configurations: the first is specialized for electron identification (electron configuration) and the second is specialized for muon identification (muon configuration). A schematic view of both proposed detector concepts is shown in Figure 2.5.

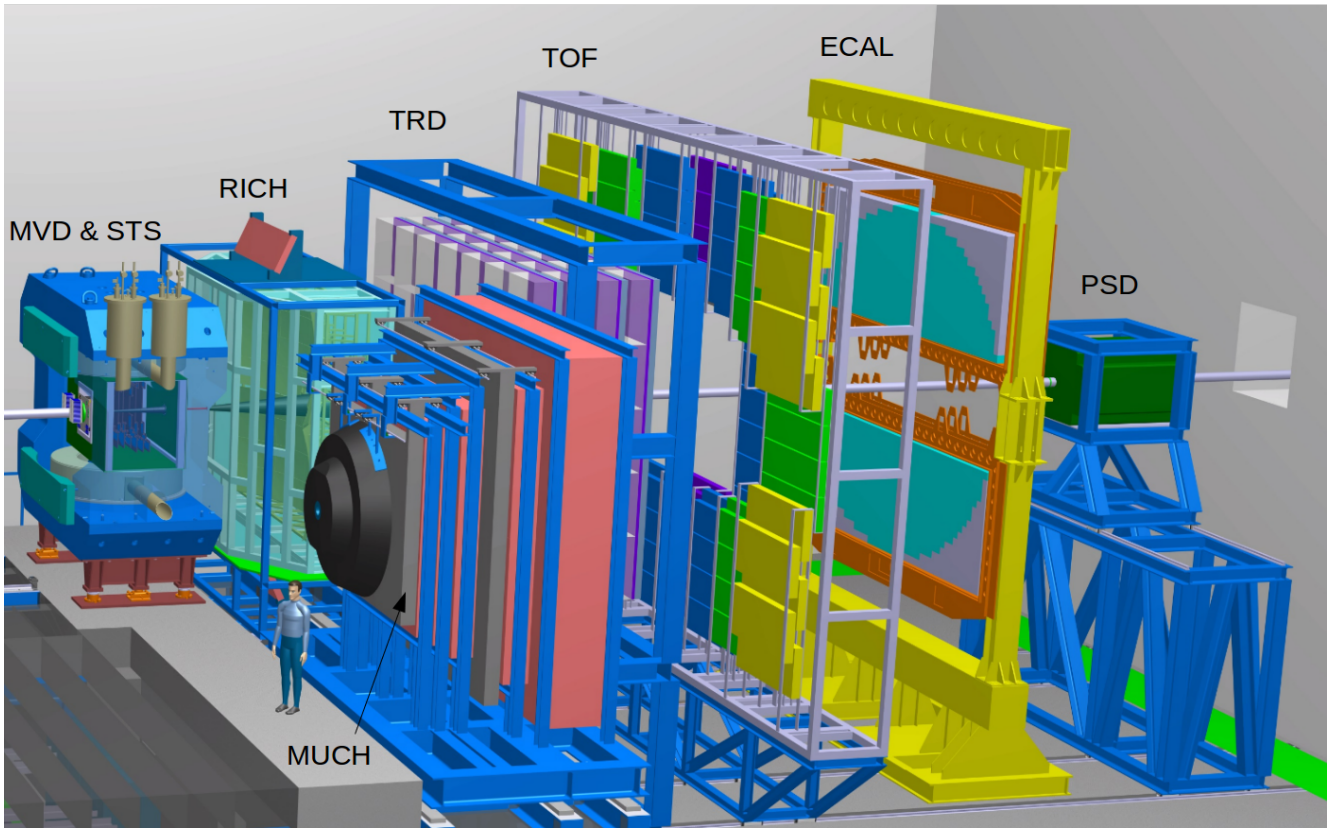

Figure 2.5: Two CBM detector configurations for electron identification (electron configuration) and for muon identification (muon configuration) [39].

The first detectors downstream after the target are the Micro Vertex Detector (MVD) and the Silicon Tracking Station (STS), which are located within a superconducting CBM dipole magnet. The MVD is needed to determine secondary vertices with good spatial precision for D meson identification. The STS allows high-resolution tracking and momentum reconstruction for all charged particles.

The next detector downstream after STS is different for both setups in Figure 2.5. In the electron configuration the RICH detector will be used for electron identification with momenta below 10 GeV/c and will provide suppression of pions coming directly from the target or from low-mass vector-meson decays in the same momenta range. In the muon configuration the Muon tracking Chamber (MUCH) will be used for muon measurements. MUCH and RICH detectors will be interchanged on a roughly yearly basis.

Further downstream will be placed the Transition Radiation detector (TRD) as complementary detector for charged particle tracking and identification of high energy electrons and positrons with momenta above 1.5 GeV/c. Directly after the TRD, the Time-Of-Flight (TOF) detector system

will be located. The TOF will perform the identification of charged hadrons via measuring their time-of-flight through the detector.

Penultimate detector in CBM experiment is the Electromagnetic Calorimeter (ECAL). The ECAL will measure photon energies in selected regions of the phase space. The last detector in the detector system of the experiment is the Projectile Spectator Detector (PSD). The PSD is needed to determine the collision centrality and the orientation of the reaction plane.

The various detector components of CBM are designed to cover laboratory polar angles from 2.5° to 25°.

Below, a short summary of the important properties of the different sub-detectors is given.

2.4.1 The superconducting dipole magnet

The dipole magnet of the CBM experiment will be superconducting [40] in order to reduce the operation costs. The superconducting dipole magnet bends all charged particles created in the collision. The curvature radius of the bending is then used to reconstruct the particle momenta with high precision. The maximum nominal field value of the magnet is 1 Tm. Field clamps at the downstream side of the magnet limit the stray field into the RICH detector system, which is of importance for the photomultipliers used for the RICH photon detector. The schematic view of the magnet can be seen in Figure 2.6

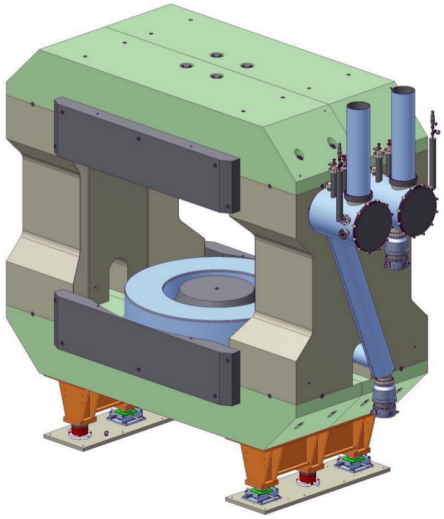

Figure 2.6: Schematic view of the superconducting magnet, used in the CBM experiment [40].

2.4.2 The Micro Vertex Detector (MVD)

The MVD is the first detector behind the collision vertex and is located as close to the target as possible. It is used for the reconstruction and identification of D mesons via their weak hadronic decay into pions and kaons (e.g. $D^0 \rightarrow K^- + \pi^+$). Also, MVD will help to reduce background in dielectron decay channels of low mass vector mesons.

The mean lifetime of the D^0 meson is $\tau = 123$ μm/c, and it is $\tau = 314$ μm/c for the $D^{\pm}$ meson. In order to suppress background contributions of promptly emitted pions and kaons one has to determine the secondary decay vertex of D mesons with an excellent resolution. In order to reduce multiple scattering the detector must have very low material budget. These requirements can be achieved by silicon detectors based on ultra-thin Monolithic Active Pixel Sensors (MAPS).

The MVD stations will be highly granular with a pixel size of 20×20 μm^2, resulting in a position resolution of 4 μm. The total thickness of the detector stations will be about 300 μm silicon equivalent, including all sensors and also support structures [41].

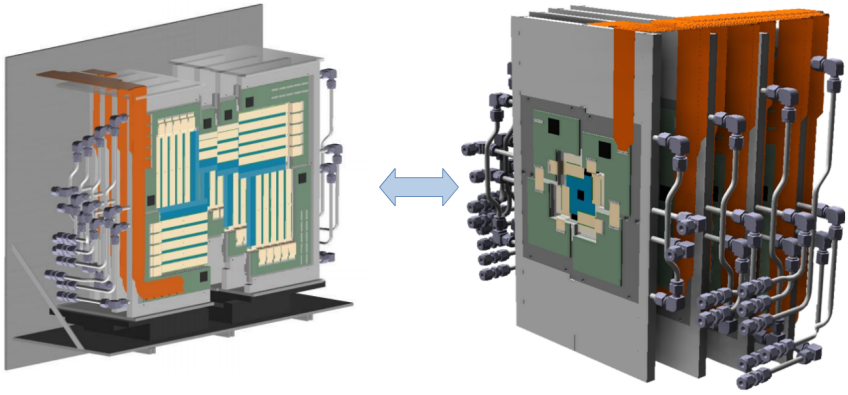

Figure 2.7: Schematic view of the Micro Vertex Detector (MVD), used in the CBM experiment [41].

The MVD has two slightly different detector geometries. Both geometries will have four stations, but located at different distances [42]. One is dedicated for better vertex resolution, therefore the detector stations are located as close to the target as possible: at distances 5 cm, 10 cm, 15 cm, and 20 cm. The second geometry is dedicated for better tracking reconstruction of charged tracks, therefore its stations are located at distances 8 cm, 12 cm, 16 cm, and 20 cm from the target. To reduce the amount of material in the active volume, the detector will be placed in vacuum. Figure 2.7 illustrates the detector geometry with four stations.

2.4.3 The Silicon Tracking System (STS)

The Silicon Tracking System is the central component of the CBM experiment. The task of the STS is to provide track reconstruction and momentum determination of charged particles. A technical challenge for the STS is to achieve high track reconstruction efficiency in a high track density environment (up to 700 tracks per event within the detector acceptance). The STS consists of 8 tracking layers of silicon strip detectors, placed at 30, 40, 50, 60, 70, 80, 90, 100 cm distance from the target [43] (see Figure 2.8). All stations will be located inside the magnetic dipole field of about 1 Tm bending power.

For successful reconstruction of the particles of interest, a relative momentum resolution of $\Delta p/p = 1$ % is required. Such resolution can only be achieved with an ultra-low material budget of the stations. To minimize the amount of material in the active volume, the electronics of the detector will be placed at the periphery of the stations. Signals from detector modules will be transported to the electronics through multi-line micro-cables. Each station consists of double-sided micro-strip sensors mounted onto lightweight mechanical support ladders, made of carbon fibers. The strips on the front side are tilted by 7.5 degrees and on the back side by –7.5 degrees creating a stereo angle of 15 degrees. The typical hit resolution achieved will be of the order of 25 μm.

2.4.4 The Ring Imaging Cherenkov detector (RICH)

The RICH detector is designed to provide identification of electrons and suppression of pions in the momentum range below 10 GeV/c. According to simulations the RICH detector will provide

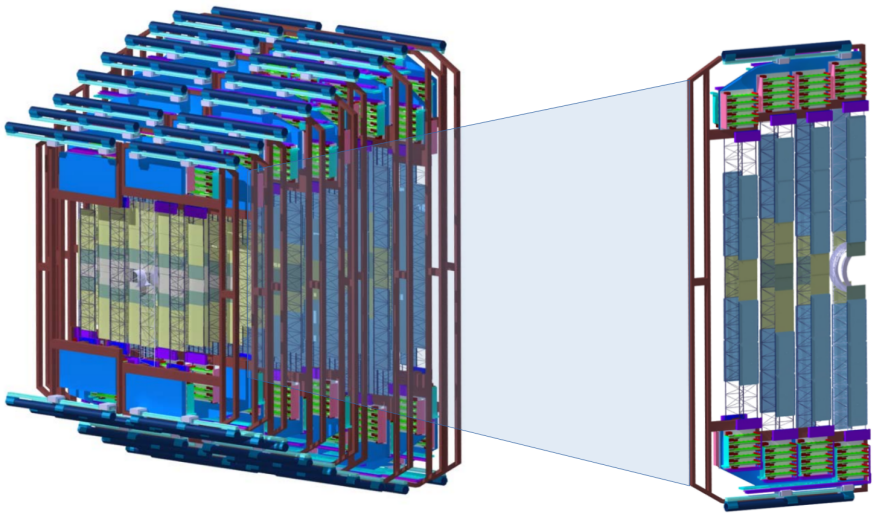

Figure 2.8: Schematic view of the Silicon Tracking System (STS), used in the CBM experiment [43].

electron identification with efficiency of about 90 % and pion suppression up to factor of 1000 for low particle momenta.

All Cherenkov counters have two main elements: a radiator through which the charged particle passes and a photodetector. The idea of counters is based on the detection of radiation emitted under a fixed angle forming a cone of Cherenkov light. In a RICH detector, this cone of light is reflected and focused by a spherical mirror to a position sensitive photodetector plane, which allows to reconstruct the projected photon ring images. Particles with the same momentum but different masses form rings with different radii, since the emission angle of the cone is determined by the speed of the particle. Due to their small mass all electrons produced in the collision, even with low momenta, emit Cherenkov light, while pions start to radiate at momenta of about $p > 4.7$ GeV/c in the CBM-RICH detector [44].

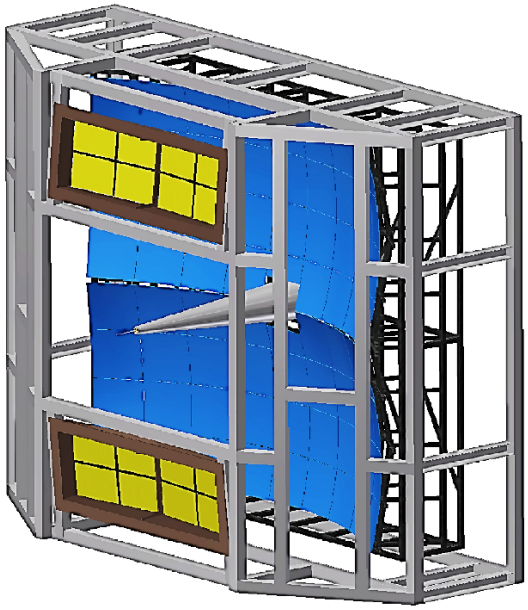

Figure 2.9: Schematic view of the Ring Imaging Cherenkov detector (RICH), used in the CBM experiment [44].

The proposed design of the RICH detector for CBM (see Figure 2.9) includes a radiator filled with CO_2 gas, two spherical glass mirrors, two planes of photodetectors, and corresponding support structures. More detailed description of the CBM-RICH detector with its parameters will be given in the next chapter.

2.4.5 The Muon Chambers (MUCH)

One of the focuses of the CBM experiment is the measurement of rare particles decaying into muons. The Muon Chamber together with STS will be the main components in the detector configuration to study such dimuon decay channels of vector mesons like ρ, ω, ϕ and J/ψ. Reconstruction of such particles requires an accurate muon identification. A setup for the Muon Chamber system is presented in Figure 2.10.

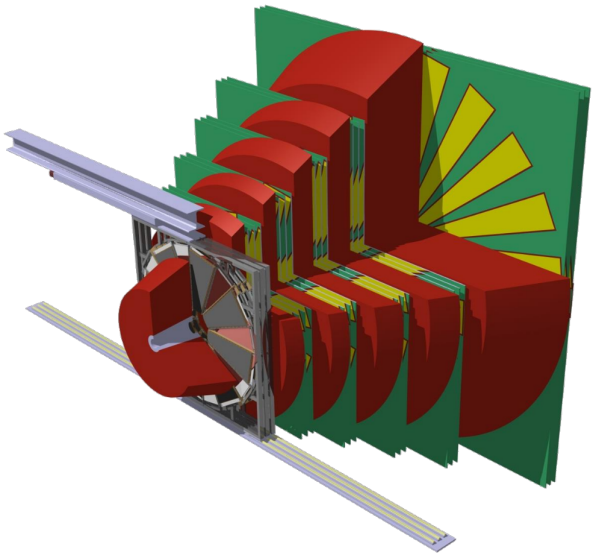

Figure 2.10: Schematic view of the Muon Chambers (MUCH), used in the CBM experiment [45].

Being minimum ionizing particles in a wide momentum range from 100 MeV/c to 100 GeV/c, muons, unlike all other particles, can penetrate several meters of iron: as electrons, they do not interact strongly but have large enough mass not to be significantly scattered inside the material and do not suffer Bremsstrahlung energy losses.

The MUCH detector will be placed just after the STS tracking system. The actual design of the muon detector system consists of 6 hadron absorber layers (first absorber is planned to be build from carbon, the other 5 from iron) and 18 gaseous tracking chambers, located in triplets behind each absorber layer [45]. The total thickness of six hadron absorbers will be about 250 cm. Candidates for the fast and highly granulated detectors are gaseous detectors based on GEM technology and straw tubes.

2.4.6 The Transition Radiation Detector (TRD)

The TRD contributes to the electron identification and tracking of charged particles. The main working principal of the TRD detector is, that a charged relativistic particle emits transition radiation (TR) when passing through the boundary between two different media with different dielectric constants ε. The intensity of the radiation depends on the energy of the particle and its type. For the expected particle momenta at CBM energies, TR is produced only by electrons and

positrons, and this offers the possibility of separating them from pions. This will help to reduce the background of short-lived particles, like vector mesons (ρ, ω, ϕ and J/ψ), decaying by their electron channel.

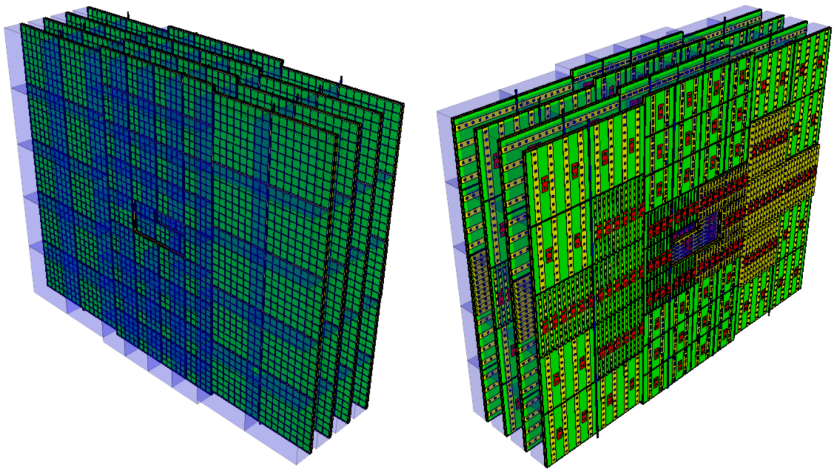

Figure 2.11: Schematic view of the Transition Radiation Detector (TRD), used in the CBM experiment [46].

Currently, the TRD is envisaged to be a system composed of one station with four layers (see Figure 2.11). The station will be located at a distance of approximately 5 m from the target [46]. Each layer consists of a radiator, in which the TR is produced by the electrons only, and of a gaseous detector, in which the deposited energy of charged particles and the TR can be measured. The gas mixture of the readout detector is based on Xe in order to maximize the absorption of TR.

2.4.7 The Time Of Flight detector (TOF)

The TOF detector is dedicated for identification of hadrons: poins, kaons, and protons. Different types of particles can have the same momentum, but due to different masses, they will have different speed. The determination of the particle mass is done by measuring its momentum p within STS detector, and its time of flight within TOF detector:

$$m = \frac{p}{\gamma \beta c} = \frac{p\sqrt{1-\beta^2}}{\beta c}, \tag{2.5}$$

where:

$$\beta = \frac{L}{c\Delta t}, \tag{2.6}$$

L is the flight path length of the particle, and Δt is the time difference between the start and stop signal of the TOF detector, c is the speed of light in vacuum.

The geometry of the detector is shown in Figure 2.12. The TOF wall consists of approximately 60,000 independent cells providing a time resolution of about 80 ps. The active area of the detector will be about 120 m^2 [47]. It is based on Resistive Plate Chambers (RPC). RPCs consist of parallel plates made of glass or ceramics and separated by the gas volume. A high voltage is applied to the external surfaces of the plates. A charged particle ionizes the gas and the electric field amplifies this ionization by an electron avalanche. The avalanche is stopped by the resistive plates and induces a fast signal on the pickup electrodes. The detector will be placed in a distance of 6 m from the target.

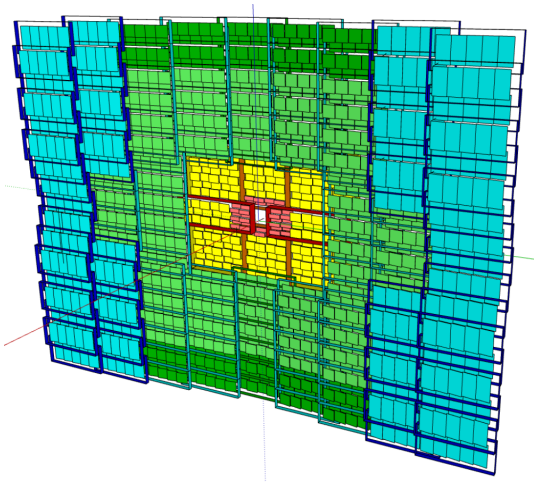

Figure 2.12: Schematic view of the Time Of Flight detector (TOF), used in the CBM experiment [47].

2.4.8 The Electromagnetic Calorimeter (ECAL)

The task of ECAL is the detection of direct photons, and photons from decays of neutral mesons like π^0 and η, which later are used for their reconstruction.

Interacting with the material of the calorimeter a photon produces a particle shower, which consists of electrons, positrons and secondary photons. In such way the energy of the initial photon is deposited in the ECAL, where it is converted to scintillation light and finally measured. This is a complementary approach to the detection of converted photons into leptons, which will be studied in Chapter 5.

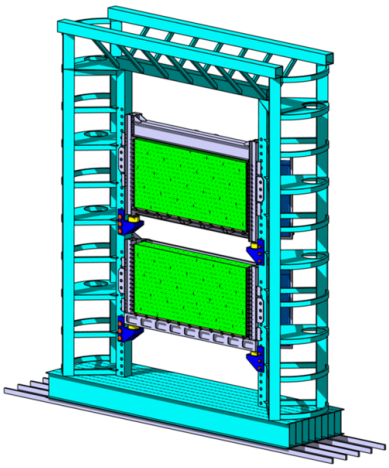

Figure 2.13: Schematic view of the Electromagnetic Calorimeter (ECAL), used in the CBM experiment [48].

The ECAL for CBM will consist of absorbers and scintillation detectors. It is a "shashlik"-type detector consisting of 140 layers made from 1 mm lead and 1 mm scintillator stacks with cell size of 6 cm $\times$ 6 cm [48] (see Figure 2.13). Such technology of ECAL is also operated in the PHENIX experiment at RHIC, in LHCb at LHC, and in many other universal particle detectors.

2.4.9 The Projectile Spectator Detector (PSD)

The PSD is the most downstream sub-detector of CBM. It will provide an experimental measurement of a heavy-ion collisions centrality and orientation of the reaction plane. Good knowledge about the impact parameter is particularly important for analyzing event-by-event fluctuations of particle yields, and in order to study collective properties of a collision, like flow, a well defined reaction plane is also important.

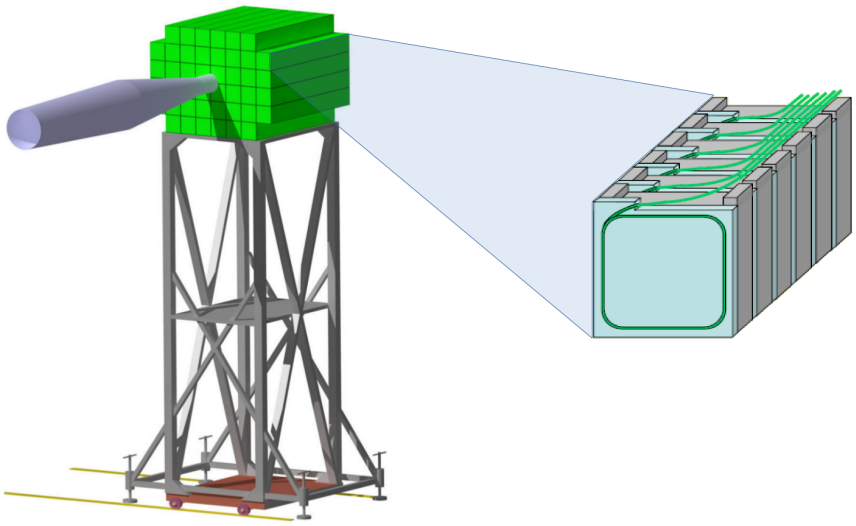

Figure 2.14: Schematic view of the Projectile Spectator Detector (PSD), used in the CBM experiment [49].

The PSD detector is a calorimeter, which will consist of 44 individual modules with a transverse size of 20×20 cm^2 [49]. Each module includes 60 lead scintillator sandwiches (see Figure 2.14). The detector will measure the number of non-interacting nucleons (spectators) from a projectile nucleus in the collision. The resolution of the impact parameter for peripheral collisions is determined as $\Delta b/b = 0.1$, and for most central collisions it is $\Delta b/b = 0.5$.

2.4.10 Data Acquisition System (DAQ)

The measurement of rare signals is an essential part of the CBM physics program, and requires high statistics, which can be achieved only at high interaction rates. The data acquisition system in CBM is designed to operate at extremely high collision rates up to 10 MHz. If one considers the highest recording speed of the modern storage media about 1 GB/s, and data flow per event of about 40 kB from a single central Au+Au collisions, it is possible to store all produced data with the collision frequency of only 25 kHz. Therefore, measurements with the collision rates of 10 MHz require additional algorithms for on-line event selection, that can reduce the number of background collisions, which do not contain interesting signals. Such algorithms reject background events by a factor of 400 or more, what allows to operate the experiment at extreme rates.

The event selection system will be based on a fast on-line event reconstruction running on a dedicated computer farm, equipped with many-core CPUs and graphics cards (see Figure 2.15). Track reconstruction, which is the most time consuming combinatorial stage of the event reconstruction, will be based on parallel track finding and fitting algorithms, implementing the Cellular Automaton and Kalman Filter methods.

Figure 2.15: Decicated computer farm (green IT Cube at GSI), used for online event reconstruction during the operation of the CBM experiment [50].

3

The CBM Ring Imaging Cherenkov detector

Electron identification is a fundamental requirement of the CBM experiment. The ability to distinguish between electrons and pions is essential for the physics, which the CBM experiment is designed to study. Electron identification is achieved by the RICH detector and several layers of TRD detector. The RICH detector will be placed directly behind the dipole magnet, covering the same acceptance as Silicon Tracking System for particles with high and medium momenta. Low momentum tracks might be bent out of the RICH acceptance due to the magnetic field.

This chapter is dedicated to the Ring Imaging Cherenkov detector. It is divided on several parts, where the key aspects of the detector are discussed. In the first section a short information about the Cherenkov radiation is given. Section 3.2 is dedicated to main technical details of designed detector. In the last section the most important settings and requirements are outlined.

3.1 Cherenkov Radiation

The Ring Imaging Cherenkov detectors work by measuring emission of Cherenkov radiation, when a charged particle passes through a certain medium faster than light does. The speed of light in the medium can be expressed by:

$$c_n = \frac{c}{n}, \tag{3.1}$$

where n is the refractive index of the medium, and c is the speed of light in vacuum.

The vacuum has a refractive index of $n = 1$. This implies, that a charged particle in uniform, unaccelerated motion in vacuum does not radiate. However, if a particle is moving with uniform constant velocity in a medium, its electric field will interact with the medium and, in case of $v > c/n$, this interaction can result in the emission of real photons, the so-called Cherenkov radiation. All known up to now media have a refractive index n greater than 1, thus, the light travels in these media with smaller speed than in vacuum. If the velocity of the particle inside such environment is larger than the velocity of light in the same medium ($v > c_n$), a wave front is formed in the medium. The shape of the cone of light depends on the particle velocity, allowing to determine its speed. Figure 3.1 shows a schematic picture of the Cherenkov radiation and its emission angle θ_c.

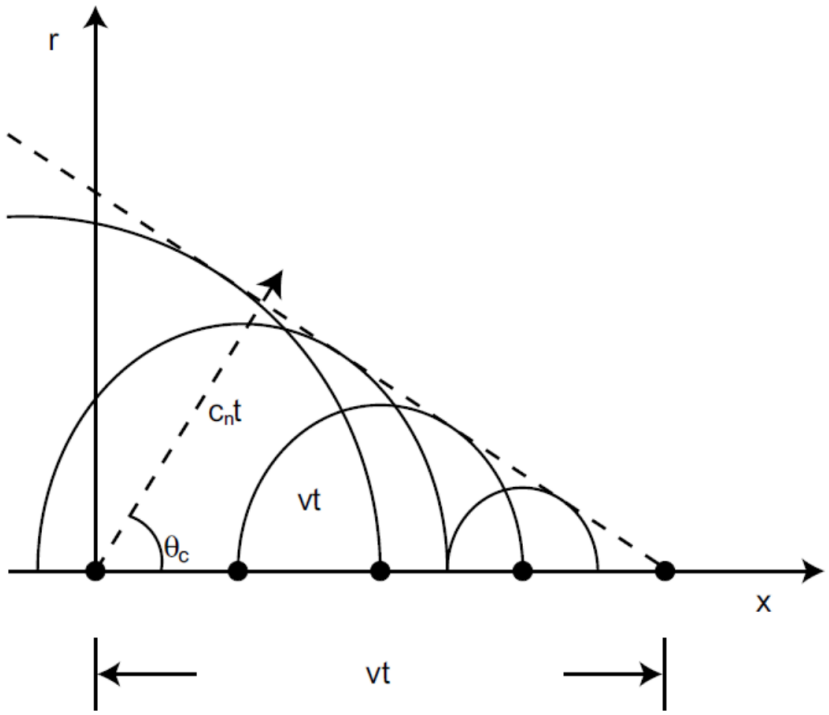

Figure 3.1: Schematic representation of the emitted Cherenkov light from the charged particle, which travel in the medium with velocity larger than the speed of light in the same medium.

The Cherenkov radiation was first experimentally discovered in 1934 by sowjet physicist Pavel Cherenkov and his supervisor Sergei Wawilow. To honor both discoverers the effect is still called Wawilow-Cherenkov radiation in Russia. Pavel Cherenkov in his first article [51] showed that all liquids without exception give off a blue-violet glow. In his research he bombarded several liquids by fast electrons, such as β-electrons or Compton electrons produced by γ-rays. The radioactive radium in this case served as a source of γ-rays. The open end of the container with a liquid was scanned with a help of an optical system and the human eye served as a radiation detector. The glow of blue light was very weak, therefore the observer was required to have "phenomenally keen vision".

Only three years later in 1937 sowjet physicists Ilja Frank and Igor Tamm performed the theoretical description and developed the so-called Frank-Tamm formula [52], which describes the whole spectrum completely. They considered, that a charged particle on its way through the medium emits the wavelets from each point in time, which add up constructively along a line defined by the emission angle. The angle of emitted photons can be derived with the geometry construction from Figure 3.1 like:

$$\cos\theta_c = \frac{c_n}{v} = \frac{c}{nv} = \frac{1}{\beta n} \tag{3.2}$$

Frank and Tamm demonstrated, that the amount of energy emitted from Cherenkov radiation per unit length and per unit of frequency is given by the law:

$$\frac{d^2E}{dxd\omega} = \mu(\omega)\frac{q^2}{4\pi}\omega\left(1 - \frac{1}{\beta^2 n^2(\omega)}\right), \tag{3.3}$$

where ω is photon frequency, q is electric charge, and $\mu(\omega)$ is permeability. Later on, as a consequence of Frank-Tamm formula, different modification appeared. For example, the mean number

of photons produced by a particle with the charge z at a given wavelength λ and at a given energy E can be given as:

$$\frac{d^2N}{dxd\lambda} = \frac{2\pi\alpha z^2}{\lambda^2}\left(1 - \frac{1}{\beta^2 n^2(\lambda)}\right) = \frac{2\pi\alpha z^2}{\lambda^2}\sin^2\theta_c, \tag{3.4}$$

$$\frac{d^2N}{dxdE} = \frac{\alpha z^2}{\hbar c}\left(1 - \frac{1}{\beta^2 n^2(\lambda)}\right) = \frac{\alpha z^2}{\hbar c}\sin^2\theta_c, \tag{3.5}$$

where $\hbar$ is a Planck constant, $\alpha = 1/137$ is the fine structure constant, and c is the speed of light in vacuum.

Some important consequences from the theoretical description of Cherenkov radiation are shown in Figure 3.2. One can see, that the number of produced photons per wavelength is different for different wavelengths. It is essential to mentioned, that number of emitted photons in ultraviolet region does not go to infinity. At deep ultra violet region the refraction index gets 1, so the emission stops here. On the other hand, the number of photons per energy bin does not depend from the energy of the particle after overcoming the threshold value.

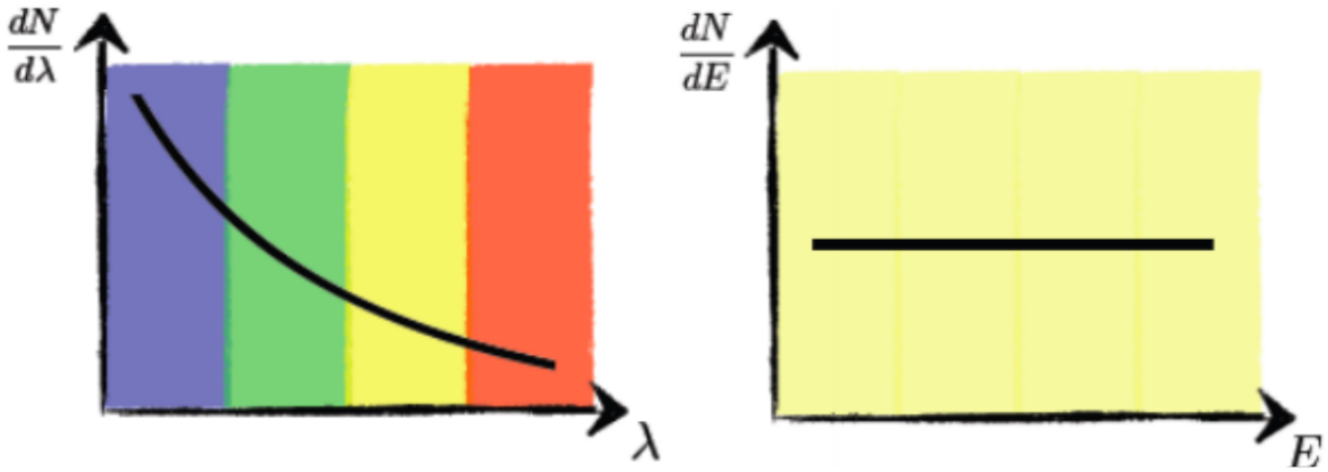

Figure 3.2: Number of Cherenkov photons per wavelength (left) and per energy bin (right)

Scientists can then combine the information about number of emitted photons from a charged particle, emission angle of emitted photons, and refractive index of the medium, in combination with particle momenta in order to calculate its mass and charge, and therefore its identity.

3.2 RICH detector technical design

A detailed description of the CBM-RICH detector can be found in the Technical Design Report [44]. In this chapter only a few important aspects from the TDR are summarized.

The CBM-RICH detector will be positioned behind the dipole magnet at a distance 1.8 m downstream from the target. Complete size of the detector is 2 m × 5.14 m × 3.93 m (length × height × width). It will share its location with the CBM-MUCH detector, both being used alternatively with a typical change period of once a year. The mechanical construction of the RICH must be therefore easy movable as a whole using a crane.

The present position and size of the detector cover maximum possible acceptance of the CBM detector in the range between $2.5° - 25°$ with respect to the nominal target position. The lower and upper values of anticipated acceptance are limited by the size of the beam pipe and by the

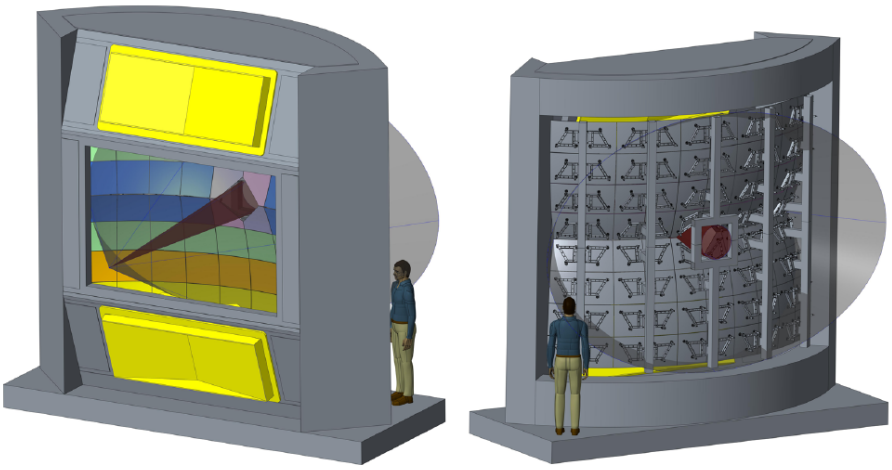

Figure 3.3: Two schematic views (left picture is the view from the back; right picture is the view from the front) of the CBM-RICH detector layout [53]. The human body illustrates the detector size.

aperture of the magnet yoke correspondingly. A schematic view of the detector layout is shown in Figure 3.3. The geometrical acceptance of the detector is indicated by the transparent gray cone.

The CBM-RICH detector is the main detector to identify and separate electrons and pions in collisions from lowest momenta up to $8 - 10$ GeV/c with a desirable pion suppression of at least a factor of 100. The detector will use a gaseous radiator, namely CO_2 gas is foreseen, which has refractive index of $n = 1.00045$, and a Cherenkov threshold for pions of $p = 4.65$ GeV/c. With CO_2 as radiator gas electrons and pions can be separated up to approximately $p = 10$ GeV/c assuming that pions can be separated from electrons up to 90 % of the maximum Cherenkov opening angle θ_c.

All photons produced along the 1.7 m long radiator will be reflected by a spherical-shaped mirror. The mirror plane is split horizontally into two arrays of spherical glass mirrors of 6 mm thickness, made of a reflective Al-coated glass substrate with a protective MgF_2 coating. Glass mirrors are chosen to provide excellent optics combined with a high mechanical stability. Each mirror half is part of a sphere with radius 3 m and consists of 36 segments (shown using different colors in left picture of Figure 3.3). This splitting of the mirror into segments allows for reasonable size of the glass mirror tiles and provides acceptable gaps between the mirrors (about $3 - 4$ mm). Both halves of the mirror are rotated outside around the X-axis by 10°.

Due to the focusing mirror system, all photons will be projected onto the photon detector plane forming rings. The photon detector covers a sensitive area of about 2.4 m^2. In the original design of the RICH detector in [44] it is foreseen to split the detection plane into four separated areas with a size of each 0.6 m × 1.0 m (height × width). One of the main outcomes of this thesis was to improve the design towards the spherical detection plane. The corresponding optimization will be presented in Chapter 4 of this thesis.

The detection modules are arranged in two units above and below the beam pipe, with each detection plane surface individually oriented towards the spherical focusing mirror. These detector planes are located behind the CBM dipole magnet and shielded by the magnet clams. Due to the high stray field from the dipole magnet it is planned to enclose the photon camera with iron shielding box to reduce the stray field in the region of the photomultipliers. Currently the design of iron shielding box is under investigation.

The design of the photon detector plane is based on Multi-Anode Photo Multiplier Tubes

(MAPMTs) (H12700 from Hamamatsu) in order to provide high granularity, high geometrical efficiency, high detection efficiency of photons also in the near ultra violet region, and a stable operability.

The read-out of the sensors will be done with the DiRICH electronics, which is currently being developed at GSI together with our group at the University of Wuppertal. The modules of the DiRICH electronics are very compact and combine the discrimination of signals, the time stamp measurement, as also the data handling itself on one single board. Each DiRICH module can handle 32 channels, therefore two modules are needed per MAPMT with 64 channels pad. To reduce the number of necessary cables for data transfer, additional concentrator boards (data combiner modules) are developed, which will combine the data from 12 DiRICH modules to one single fiber output. The whole CBM-RICH photon camera will be divided into several small PCB backplanes (camera modules), each carrying 3×2 MAPMTs. For better operability, each backplane will have one power module, providing power for the electronics and also for the MAPMTs. A schematic drawing, showing one backplane with 12 DiRICH modules, the concentrator board, the power board, and 6 MAPMTs, is shown in Figure 3.4.

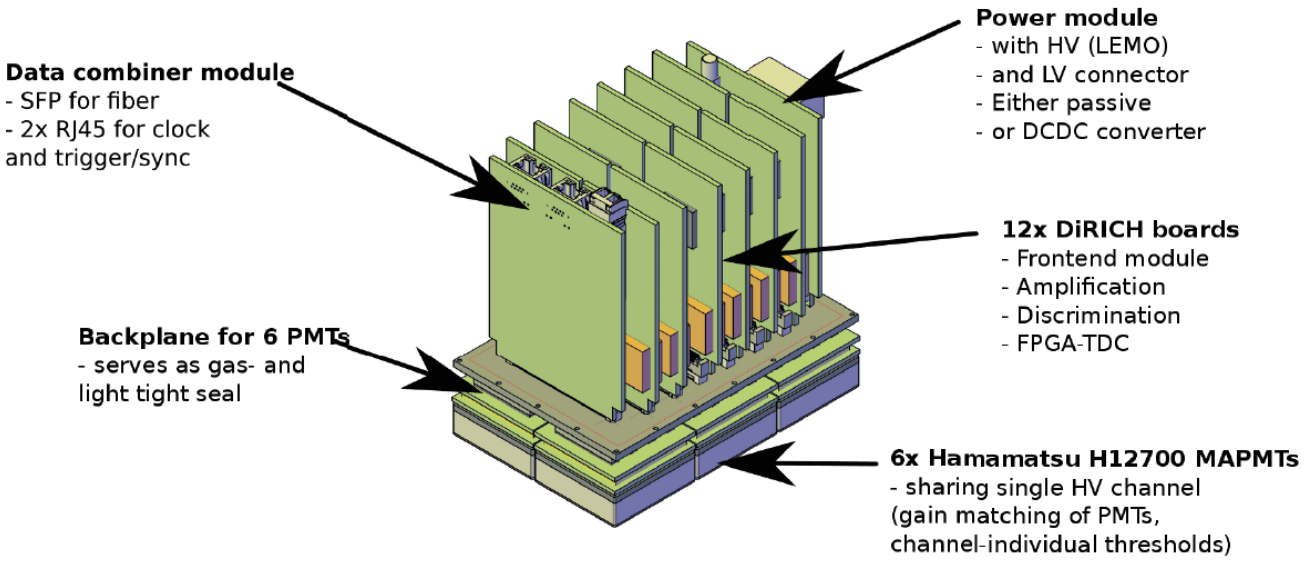

Figure 3.4: Schematic representation of one backplane with 12 DiRICH modules, 1 concentrator board, 1 power board, and 6 MAPMTs, designed for the CBM-RICH photon detection plane [54].

3.3 Environmental setting and requirements

Several important environmental aspects had to be considered in the development of the CBM-RICH detector:

- interaction rates of up to 10 MHz:

  Since the CBM experiment will be operated with Au+Au at interaction rates of up to 10 MHz, this puts up special requirements onto the detector. Such high rates require from the sensors in the detector to be fast and also to have an adequate fast read-out chain, in order to collect all necessary data. The RICH detector readout chain is designed to have a very good timing precision in the order of 1 ns to be able to suppress overlapping background due to noise or beam particles.

- track densities of approximately 1000 charged particles in central Au+Au collisions:

  The huge track multiplicity per event requires from the photon detector high ring reconstruction ability and their precise position determination on the PMT plane in order to match it later with the tracking system. It is also important to have high separation ability between pions and electrons for dielectron measurements.

- a rather high radiation level in the setup:

  The CBM setup has to operate in a harsh environment with respect to radiation doses due to the high interaction rates, high track multiplicities, and running periods per year. For the RICH detector 4 crucial effects due to high radiation dose have been considered: dissociation of the radiator gas (CO_2), radiation damage of the photon camera together with its electronics, radiation damage of the mirrors, radiation damage of wavelength-shifting films applied on the surface of the photomultipliers. Detailed simulations have been performed with FLUKA [55] (general purpose tool for calculations of particle transport and interactions with matter). The detailed simulation results can be found in [44].

- large number of secondary electrons produced in the material in front of the RICH detector:

  The RICH detector will measure about 70 rings in central Au+Au collisions, where the majority of these rings stems from secondary electrons. Therefore, the ring reconstruction algorithm and further matching with the tracking system should provide reliable results in order to reject background electrons, produced in the material in front of the RICH detector.

- magnetic stray field due to the close vicinity of the CBM dipole magnet:

  The magnetic stray field at the place of the RICH photon detector has to be kept below 1 mT. Larger field values will result in efficiency losses of the MAPMTs. A possible solution presently considered against stray field in the RICH detector will be an iron shielding box, which was previously mentioned earlier in this section.

- possibility to exchange RICH and MUCH detectors in order to allow independent measurements of the dilepton signals at low and high masses:

  One of the main tasks in CBM is measurements of both dilepton channels (e^+e^- and $\mu^+\mu^-$). Both these channels will be measured separately in order to provide independent evaluation of the results. It will be achieved with an exchange of the RICH and MUCH detectors. They will operate on a roughly yearly basis.

- low material budget beam pipe and beam pipe access:

  The particles can scatter on beam pipe material, and, as a result, generate secondary particles, which leads to additional background. For the RICH detector it will be important to keep the material budget as low as possible in order to reduce the production of secondary electrons in particular. The best shape of the beam pipe is a trade-off between minimum interference with measurable particles and low probability of ion interactions with the walls. The beam pipe in CBM will be splitted in several sections in order to allow the separate handling of different sub-detectors. The first part of pipe will be closely attached to the STS. To allow the exchanging of the RICH and MUCH detectors both are required to have their own beam pipes. The next beam pipe section would then start with the first TRD station. Every section should be tightly connected one to each other to keep the vacuum inside the beam pipe.

4

CBM-RICH detector geometry optimization

The previous chapter covered the technical characteristics of the CBM-RICH detector, which were also presented in the CBM-RICH technical design report [44]. The high electron identification capabilities of the RICH detector together with the high momentum resolution of the tracking system are essential for the CBM dilepton physics program. One important technical aspect for efficient electron identification is an optimized shape and position of the photon detection plane.

In this chapter several simulation studies for optimization of the photon detection camera are presented. The first section starts with a short description of the present layout of the RICH detector. It describes difficulties to build mechanically the present design of photon detection plane and motivate the choice of another photon detection layout. The second section gives a detailed overview of the basic optimization procedure together with description of technical aspects used in the simulation. In Section 4.3 are presented optimization results basically with respect to three main parameters. Section 4.4 covers the comparison between old geometry and new optimized geometry based on the simulations of rare dilepton probes as well as of pion background contribution. The final parameters for the new design of the photon detection plane are summarized in Section 4.5.

4.1 Status quo and motivation for re-optimization

A first optimization cycle of the geometrical design of the CBM-RICH detector was done for the Technical Design Report [44], filed in 2013. At that time, the optimization focused on the optical properties, but did not yet consider mechanical constraint aspects, like for example additional space requirements for the readout electronics. In this first design, the photon detection system consists of two detection planes: one above and one below the beam pipe (see Figure 4.1). Each of them is horizontally split into two sub planes, forming a wing-shaped structure, therefore also referenced as "wing-shaped" geometry. The pair of wings form an opening angle of 20° with respect to each other. This geometry is reflected in the Geant Monte Carlo simulation as geometry "rich_v16a_1e".

In this first design each individual 1000 mm × 600 mm detector plane is divided into four sub-parts, corresponding to four printed circuit boards (PCB) carrying the photon sensor devices. In Figure 4.2 one can see the photon detector supporting frame as well as a possible installation

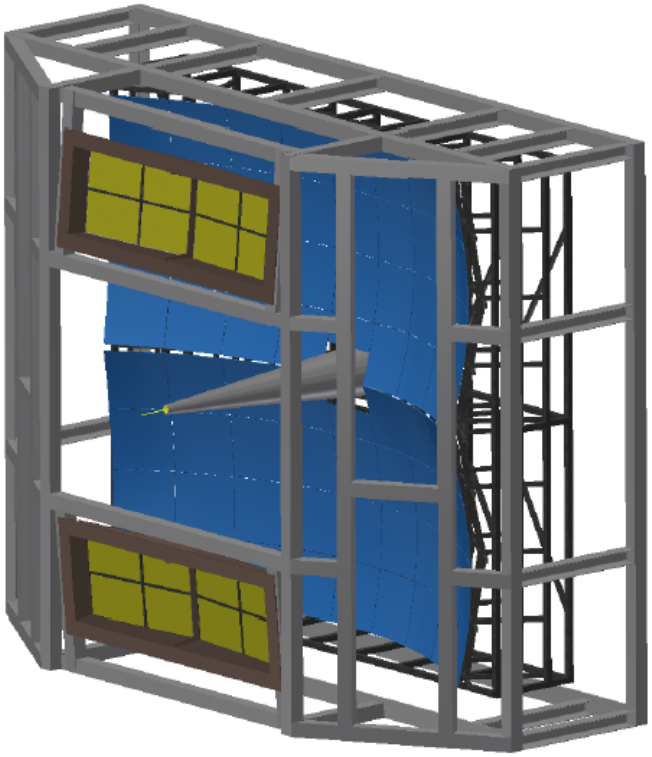

Figure 4.1: Back view of the photon detection planes of the CBM-RICH detector. The geometry presented here is described in the RICH TDR, and implemented in CbmRoot environment as "rich_v16a_1e". It has four sub planes, rotated around Y and X axes by 10° each.

and sealing scheme for the individual PCBs.

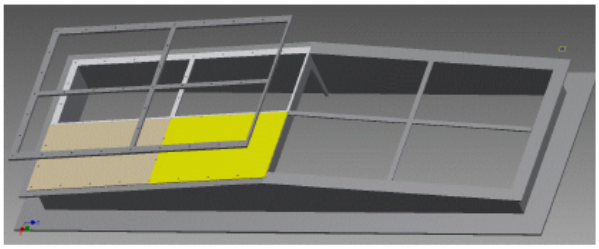

Figure 4.2: Preliminary design of RICH photon detection planes according to the Technical Design Report [44].

More realistic mechanical modeling of the detector design shows that the mechanical design can not be realized in such a way due to overlaps between the electronic readout modules from neighboring PMT boards as shown at left picture in Figure 4.3.

A possible solution of this problem would be to increase the space between two sub planes, but this would result in a non-implemented dead area between two planes of up to 5 cm. It is a significant gap right at the point, where the highest particle occupancy is. One can do some mechanical tricks to minimize the corresponding dead space area, but it would always give problems in this point.

Looking for the better solutions, the idea of a continuously curved detector plane came up, as illustrated at right picture in Figure 4.3. The curved geometry might be mechanically easy to

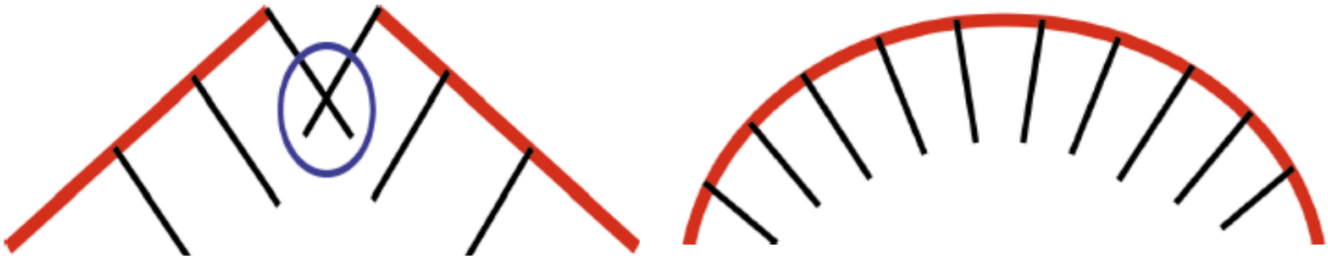

Figure 4.3: Schematic representation of wing geometry with intersection between modules behind the PMT plane, when the electronics is taken into account (left picture) and sketch of the alternatively suggested continuously curved PMT plane (right picture).

implement due to more compact size of the meanwhile developed 3×2 MAPMT readout modules (see Figure 3.4), and would help to overcome the dead space limitation of the wing geometry. In addition, since the focusing mirror system has a spherical shape, the ideal camera plane has a spherical shape as well in order to optimize the ring sharpness. However, such a spherical shaped photon detection plane complicated and expensive to build. Therefore, as alternative approximation, a cylindrical shaped plane instead of spherical will be considered as a possible new geometry for the CBM-RICH detector.

Optimization parameters

The detailed description of a new method with determination of a cylindrical photon detection plane is given in the next section of this chapter. The optimization procedure of the cylindrical geometry is done basically with respect to three parameters:

- R - radius of the cylindrical camera
- θ_x - tilting angle of the camera around X-axis
- Z - position of the camera with respect to collision point

And in another section will be discussed the optimal size of the photon detection plane, which has big impact on costs. On the other hand, the size of the camera has a big influence on efficiency of particles reconstruction and thereby on the performance of the camera.

Optimization criteria

The optimization procedure of the RICH geometry is concentrated on two main aspects of the detector: the best optical properties of rings and maximum possible acceptance coverage. In order to properly find hits, which belong to one ring, and later fit them with a circle or with an ellipse, a dedicated ring finding algorithm is used. In case of CBM, the applied ring finding algorithm is optimized to achieve large ring finding efficiency in a high ring density environment. However, the ring reconstruction efficiency directly depends on the optical quality of the ring image. Therefore, it is the most crucial parameter for the optimization. A maximum possible acceptance coverage is necessary in order to not miss, for example, one of the particles from the $\omega \rightarrow e^+e^-$ decay, and, as a result, fail to reconstruct a rare particle decay of interest.

For the ring finding algorithm in the CBM-RICH detector two parameters are most important: ring resolution parameter (dR) and ellipticity of the ring (B/A). The dR parameter can be expressed with formula:

$$dR = \sqrt{\frac{\sum_n (d_n - d_{fit})^2}{n}},$$

where n is number of all hits corresponding to the ring and $(d_n - d_{fit})$ is the closest distance between individual hit and fitted ring/ellipse. The B/A parameter is defined by:

$$B/A = \frac{B}{A},$$

where B is minor axis and A is major axis from the ellipse fit of the ring image. The optimization is done based on maximizing B/A and minimizing dR.

Since the ring finding algorithm is able to deal also with elliptic ring images, the B/A parameter is less important than dR. Therefore, the further analysis steps first of all are concentrated only on optimization of dR parameter, as criterion for ring sharpness.

4.2 Basic optimization procedure

In order to optimize the optical ring sharpness on the PMT plane, the PMT cathodes have to be arranged close to the focal plane of the focusing mirror. In the case of the CBM-RICH detector, which uses a spherical mirror with a curvature radius of 3 m, its focal plane should be also spherical with a curvature radius of 1.5 m (see Figure 4.4).

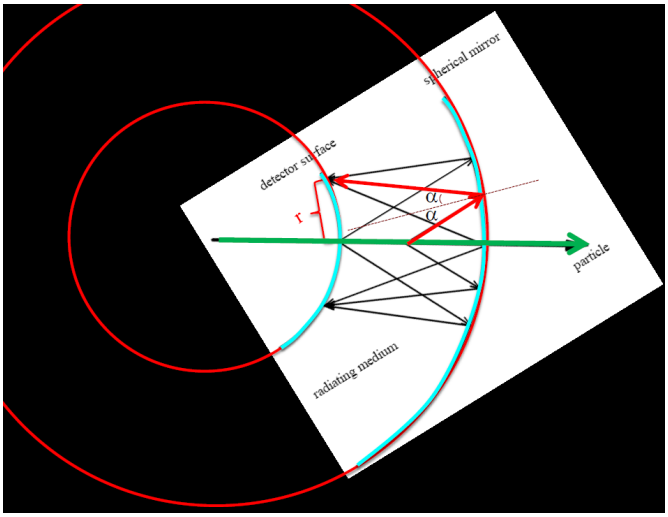

Figure 4.4: The best position for the PMT plane from the geometrical point of view. The big circle corresponds to the position of the spherical mirror, and the smaller circle to its focal plane location.

The geometry optimization can not be based only on the pure geometrical calculation of the curvature radius and position of PMT plane, since it does not take into account several key aspects, which are present for real measurements. The main aspects, what might possibly give uncertainty of the focal plane, are tilting of the mirror and bending of charged tracks leading to an undetermined entrance angle. Consequently, an additional method of investigation for position and size of PMT plane is needed. Such method will be a complementary approach to the pure geometrical calculation.

Simulation tools

The newly developed approach is based on simulations, which include realistic detector geometries as well as position-dependent magnetic field. The simulation is performed within the CbmRoot framework, which propagates particles through the CBM detector with the help of Geant3 [56]. Geant is a simulation software designed to describe the passage of elementary particles through matter, using Monte Carlo methods. The name is an acronym formed from "GEometry ANd Tracking". Geant was originally developed at CERN for high energy physics experiments, but it also has been used in many other fields.

As event generator for the geometry studies either BoxGenerator or Pluto generator are used. For the first part, where the cylindrical geometry is determined and optimized, a homogeneous occupation of the full PMT plane by single tracks from BoxGenerator is used. BoxGenerator is a simple particle gun, which can generate particles with any momentum distribution. Later on, for size optimization as well as for comparison of the new optimized cylindrical geometry with old wing-shaped geometry the Pluto generator [57] is used. Pluto is a simulation framework for heavy ion and hadron physics reactions. It includes physical models for hadronic and electromagnetic decays, resonance spectral functions with mass-dependent widths, and anisotropic angular distributions for selected channels, which are modeling closely measured data from many different experiments. The main advantage of the Pluto generator is, that it can simulate rare decays like $\omega/\rho \rightarrow e^+ + e^-$ with kinematic conditions, which are close to physics expectations.

Description of the method

To obtain the optimal focal position from simulation one can use the present wing shaped design of the RICH detector (rich_v16a_1e version). First of all the tilted wing-shaped PMT planes were rotated back, such that they make a single flat plane without additional rotation around X and Y axes. In such position every single point on the plane with a coordinate (x, y) will have the same third coordinate z, where z is in beam direction. The wing shaped PMT plane before and after rotation can be seen on the left and right sides in Figure 4.5 correspondingly.

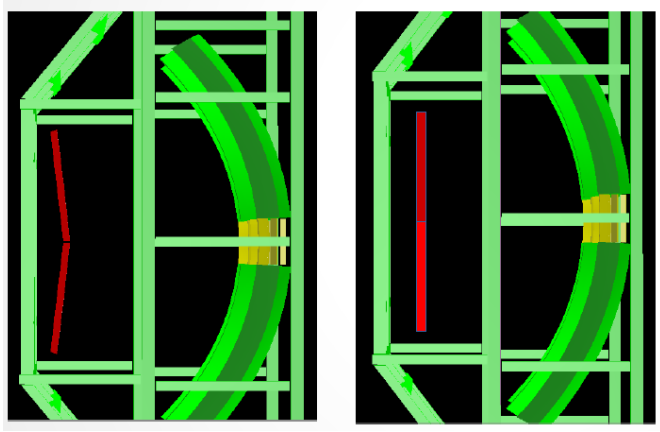

Figure 4.5: Top view of the RICH detector with normal position of wing-shaped PMT plane from the geometry file rich_v16a_1e (left picture) and unfolded wings for the analysis discussed here (right picture).

The main idea behind the method can be summarized in following steps:

1. Take the flat PMT plane and move it along Z axis.

2. In every z position one can find on the PMT plane coordinates (x, y), where the flat PMT plane intersects the optical focal plane of the mirror. In these points the ring sharpness of reconstructed Cherenkov rings will be optimal, hence dR parameter will be the smallest one.

3. For every (x, y) coordinate on the PMT plane plot dR values as a function of z position of the PMT plane and find a coordinate (x, y, z), where dR has minimum value.

4. Build the 3d shape from the found points of optimal dR and fit the corresponding shape with a cylinder.

5. Extract from the fit main parameters of interest: R, θ_x, Z.

As a first step, the full procedure described above is performed without magnetic field in order to investigate the perfect focal plane of the tilted mirror within this approach. As a second step, simulations are repeated with 1 Tm magnetic field in order to see its possible impact on the focal plane determination.

4.3 Result of the optimization procedure

The simulation was done using BoxGenerator, and consists of 100000 electrons and positrons (one particle per event) homogeneously distributed over full acceptance range $(2.5° - 25°)$ of the upper part of the detector. The analysis did not include second half of the detector since both halves are symmetric. Generated particles have the momentum range up to 3 GeV/c. As a first step, the magnetic field is turned off for this simulation, since only the perfect focal plane should be investigated.

The simulation is performed in such a way, that every single point (x, y) on the flat PMT plane at a certain z coordinate is assigned to a reconstructed Cherenkov ring center from the electron. For each event the dR value (based on ellipse fit of the Cherenkov rings) is mapped as a function of (x, y). The same simulation is done for different z positions, where this flat plane is moved upstream and downstream along the beam direction. The ranges for upstream and downstream movement are chosen such, that the optimal focal position is crossed for each (x, y) point.

Comparing dR value for each (x, y) position along z, one can find a minimum dR value for (x, y, z). As an example, one see in Figure 4.6 the dependence of dR value from z position for the randomly chosen (x, y) coordinate. Figure 4.6 shows the dR distribution for the coordinate $x = 42.5$ cm and $y = 172.5$ cm on the PMT plane as a function of distance from interaction point of two nuclei. The red line on the figure shows fit of the data points with a parabolic function, which clearly indicate the position with minimum dR.

Combining such minimum points in one picture, one can plot a 3d shape of the optimal focal plane. Such shape can be further fitted with a cylindrical shape, and the fitted parameters can be extracted. The 3d shape of the optimal focal plane with different colors and its cylindrical fit with a red line are shown in Figure 4.7.

The cylindrical approximation fits quite well to the optimal spherically shaped focal plane, as can be seen from the Figure 4.7. The extracted curvature radius of the cylinder is $R = 160$ cm, and rotation angle is $\theta_x = -17°$. The corresponding result is shown in Table 4.1.

The same analysis has been repeated with magnetic field. Obtained parameters from the simulation with magnetic field have small deviation from the simulation without magnetic field, but they are very close to them. These results suggest that for the simulation described here the magnetic field has no significant influence on the result.

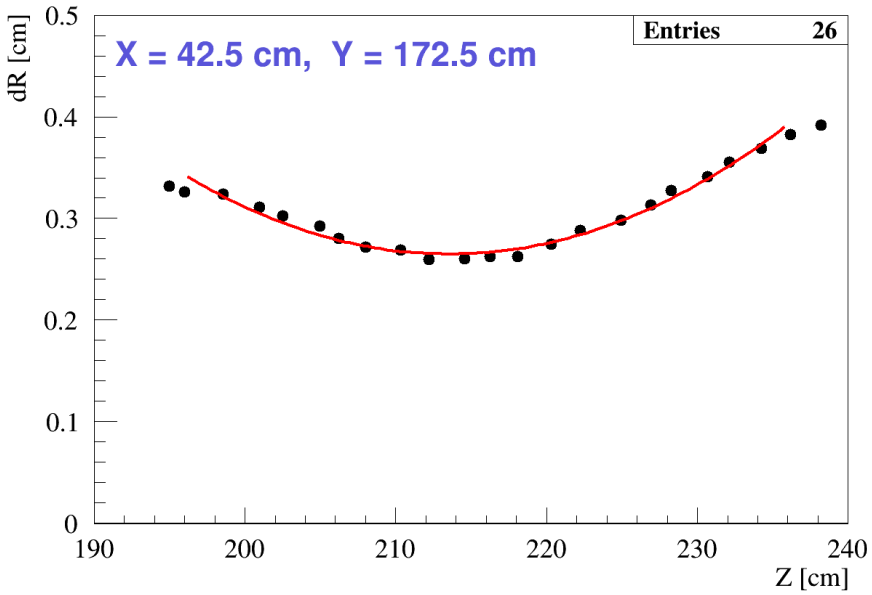

Figure 4.6: Dependence of dR value from z position for ($x = 42.5$ cm, $y = 172.5$ cm) coordinate on the flat PMT plane. The black dots correspond to the dR values for different z coordinates, and the red line shows its fit with a parabolic function. The optimal focal point here is $z = 213$ cm.

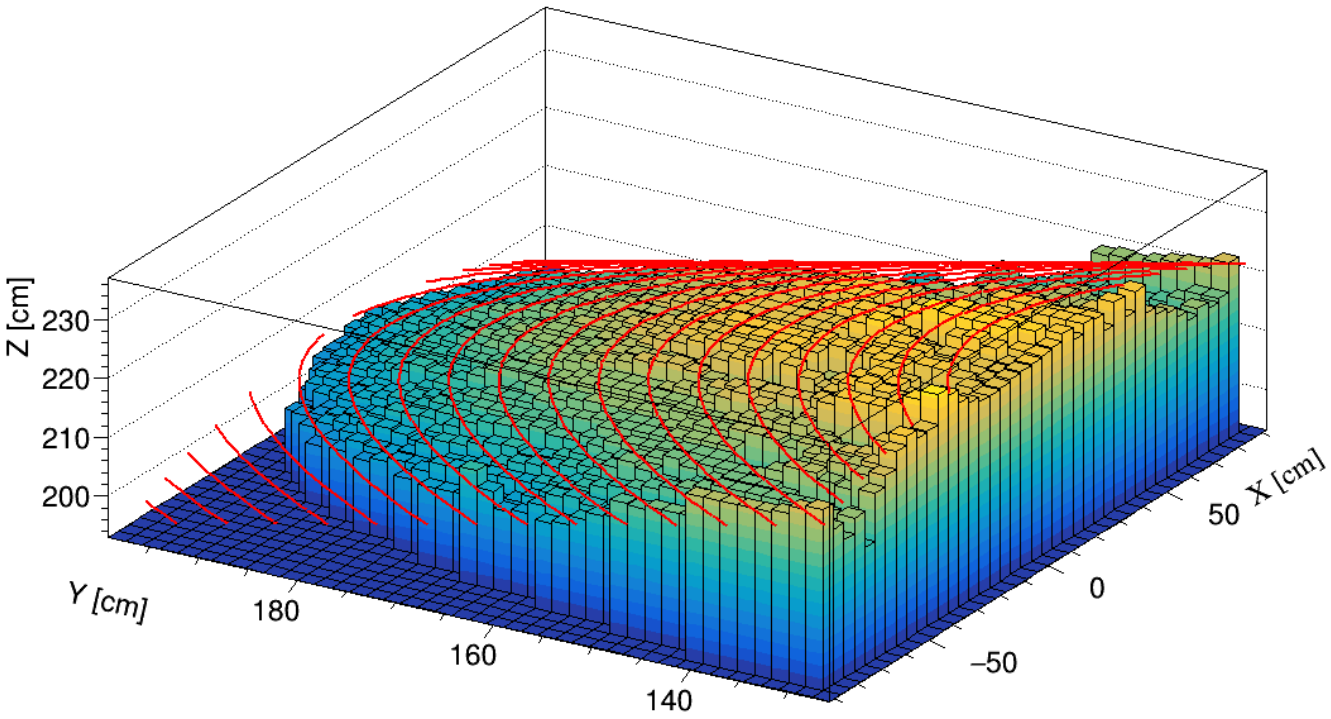

Figure 4.7: 3d representation of z position resulting in minimum dR value for each (x, y) coordinate. Results obtained from simulations with 100000 events containing one electron or positron per event. The fit of the observed shape using a cylinder approximation is shown with the red line.

An interesting fact, which came out from this analysis, is the negative rotation angle of the focal plane. A comparison between previous wing-shaped geometry and new cylindrical geometry, as extracted from the fit, is shown in Figure 4.8. The positive rotation angle of the original wing-shaped PMT plane was chosen not only to have minimal dR value, but also optimal B/A

Parameter	Value
R	160 cm
θ_x	$-17°$

Table 4.1: Focal plane parameters obtained from the numerical method.

and efficiency values. Therefore, after the implementation of cylindrical geometry into CbmRoot environment, it was decided to investigate in a second optimization step the dependence of dR, B/A, and efficiency values from rotation angle θ_x of cylindrical PMT plane and its radius R.

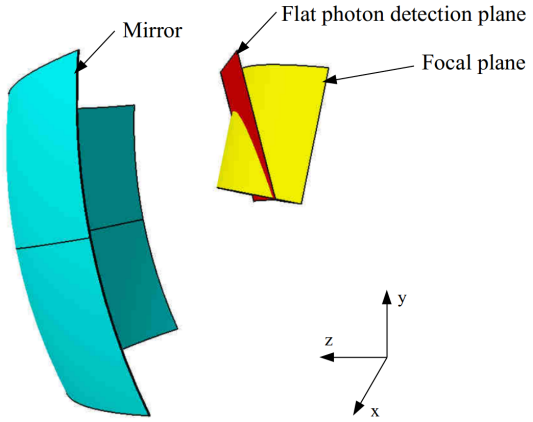

Figure 4.8: Schematic representation of extracted parameters for cylindrical PMT plane (yellow color) and current wing-shape PMT plane (red color) relatively to the spherical mirror position (blue color).

4.3.1 Optimization of radius R and rotation angle θ_x

In order to do so, additional simulations were performed for different θ_x and R combinations, where angle θ_x was changed from $-20°$ to $+30°$ (where $0°$ means that PMT plane is orientated perpendicularly to Z-axis), and the cylinder radius R was changed from 100 cm to 220 cm. Every simulation is based on 10000 events with one electron or positron per event homogeneously distributed over the full acceptance range. During this series of simulations the middle point of the cylindrically shaped PMT plane always had the constant coordinate $(0, 160, 233)$ cm relatively to the target position, hence the rotation is done around this point.

In Figure 4.9 one can see the obtained results: the upper, middle, and bottom graphs show correspondingly the mean dR, mean B/A, and efficiency (ratio between number of registered to number of produced leptons) over the full cylindrical PMT plane for different combination of θ_x and R.

The best configuration for the PMT plane after the optimization process must have the minimum dR, biggest B/A, and biggest efficiency. Unfortunately, as can bee seen in Figure 4.9, the minimum dR can be achieved with the negative rotation angle, but the maximum B/A can be with a positive rotation angle. Concerning the efficiency one can see, that the efficiency is almost constant for all parameters, at a level of 95 %, except the region with high cylinder radius and negative rotation angle. Therefore, the optimization boils down to make a compromise between dR and B/A, when taking into account also the efficiency value.

One can see from the Figure 4.9, that changing the rotation angle of the cylindrical PMT plane θ_x from negative to positive values does not change dramatically dR value (from $\theta_x = -20°$ to

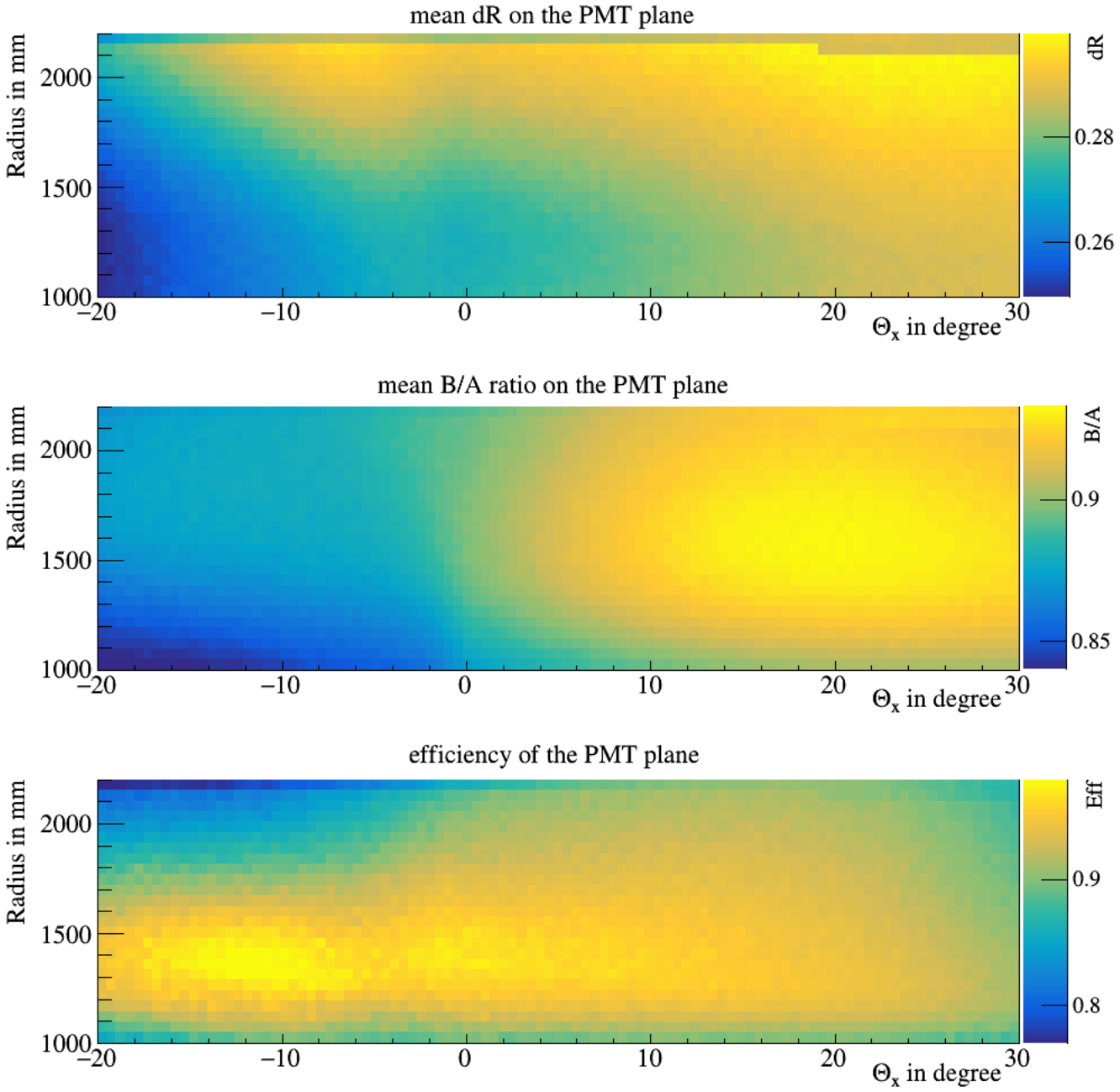

Figure 4.9: Parameter scan results for different rotation angles θ_x and cylinder radii R. The color scale on the upper graph shows mean dR over the full cylindrical PMT plane, on the middle graph - mean B/A over the full cylindrical PMT plane, and bottom graph - efficiency of the cylindrical PMT plane with current configuration.

$\theta_x = +20°$ the difference in dR is less than 0.03 cm, what correspond to relative change of about 10 %), but it increases noticeably the B/A value (from $\theta_x = -20°$ to $\theta_x = +20°$ the difference in B/A is about 0.09 corresponding to relative change of about 10 %), which is quite significant. Taking into account the efficiency, good candidates for cylindrical geometry parameters from the Figure 4.9 are: curvature radius $R = 150$ cm, rotation angle around X-axis $\theta_x = 15°$.

To make the final statement about the best parameter configuration one needs to look not only at mean values of dR and B/A, but also consider their position dependent variation on the photon detection plane. The detector geometry has to be optimized with respect to the reconstruction of particles originating from central Au+Au collisions. In these types of collisions, most of the rings

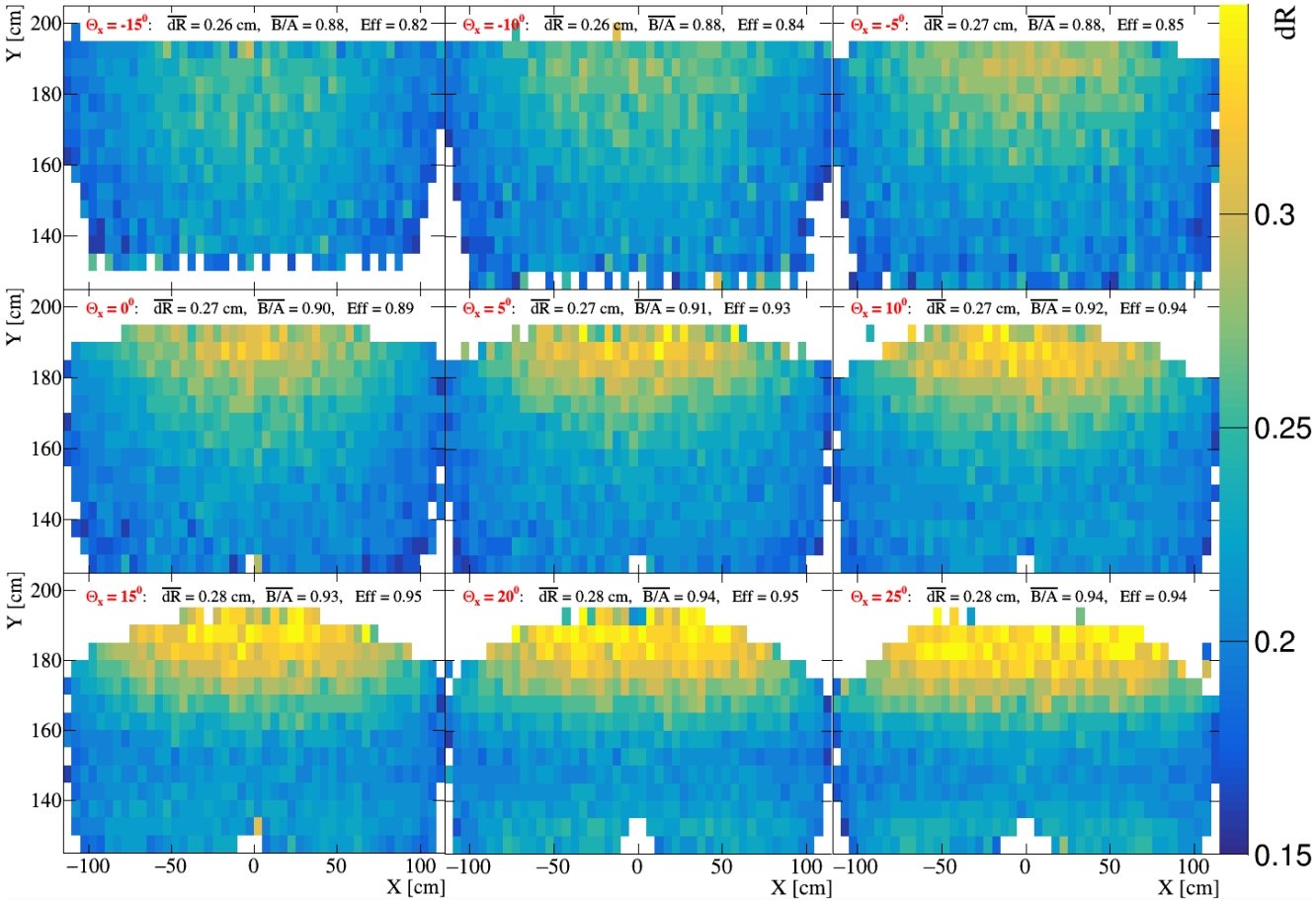

Figure 4.10: dR distributions for several different rotation angles θ_x with fixed cylinder radius $R = 150$ cm and center position of the detection plane $(0, 160, 233)$ cm. With black letters on every graph the mean values of dR, B/A, and efficiency are shown for each configuration. Different rotation angles θ_x are shown with red letters

will be located in the middle part of the photon detection plane, and only a small fraction of rings will be located close to the borders of the detection plane. Therefore, it is necessary to have the best ring parameters especially in the middle region of the detection plane. In Figure 4.10 and in Figure 4.11 one can see dR and B/A distributions correspondingly on the photon detection plane for several different rotation angles at radius $R = 150$ cm. As one can see in Figure 4.10 and in Figure 4.11, cylindrical parameters $R = 150$ cm and $\theta_x = 15°$ give not only good mean values of dR and B/A, but also have the region with best ring quality in the middle of the detection plane, as it is needed for heavy ion collisions measured within the CBM experiment. The corresponding result is shown in Table 4.2.

Parameter	Value
R	150 cm
θ_x	15°

Table 4.2: Best cylindrical parameters from the optimization of R and θ_x of the photon detection camera. Results are obtained with fixed center position of the camera at $(0, 160, 233)$ cm.

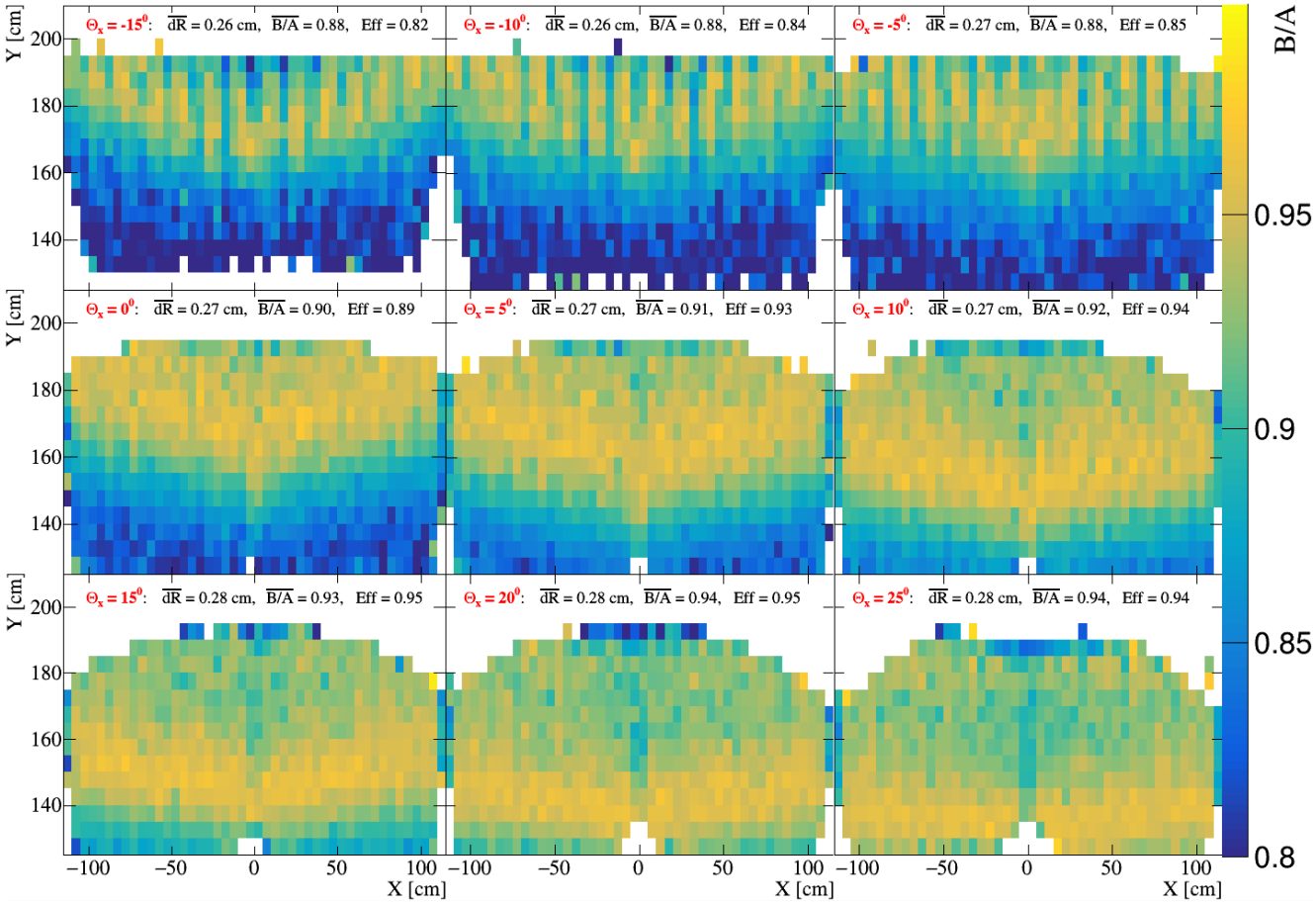

Figure 4.11: B/A distributions for several different rotation angles θ_x with fixed cylinder radius $R = 150$ cm and center position of the detection plane $(0, 160, 233)$ cm. With black letters on every graph the mean values of dR, B/A, and efficiency are shown for each configuration. Different rotation angles θ_x are shown with red letters.

4.3.2 Optimization of camera Z position

In addition to the optimization of photon detection plane radius and tilt angle, also the Z-position of the whole camera module has to be optimized again, taking into account additional space constraints with respect to the additional readout electronic modules to be mounted on the back (i.e. upstream) side of the detector plane. The simulations for such dependence are performed in the same way as previously for cylinder radius $R = 150$ cm and three rotation angles $\theta_x = \{-15°, 0°, 15°\}$, changing the center position of PMT plane for $\Delta Z = -5$ cm back and for $\Delta Z = +5$ cm forward, where the reference start parameter $\Delta Z = 0$ cm corresponds to the value of $Z = 233$ cm from the target, as it was used as a standard value in previous simulations. The results can be seen in Figure 4.12 and in Figure 4.13, where dR and B/A distributions correspondingly are shown on the photon detection plane for different rotation angles and different Z positions.

As can be seen in Figure 4.12 and in Figure 4.13, advantages of the positive rotation angle of the photon detection plane $\theta_x = 15°$ are the high efficiency and high B/A values. One can also see, that there is no dramatical change of key values during the shifting of PMT camera along beam axis for ± 5 cm. The disadvantage of the positive rotation angles of the photon detection plane is slightly increased dR value, but mostly in the top region of the PMT, where low amount of rings is expected. The best result can be obtained via shifting the PMT plane for -5 cm (closer

to the magnet) from start value. Relevant dR and B/A distribution for such shift are shown on the right-top picture in Figure 4.12 and Figure 4.13 correspondingly.

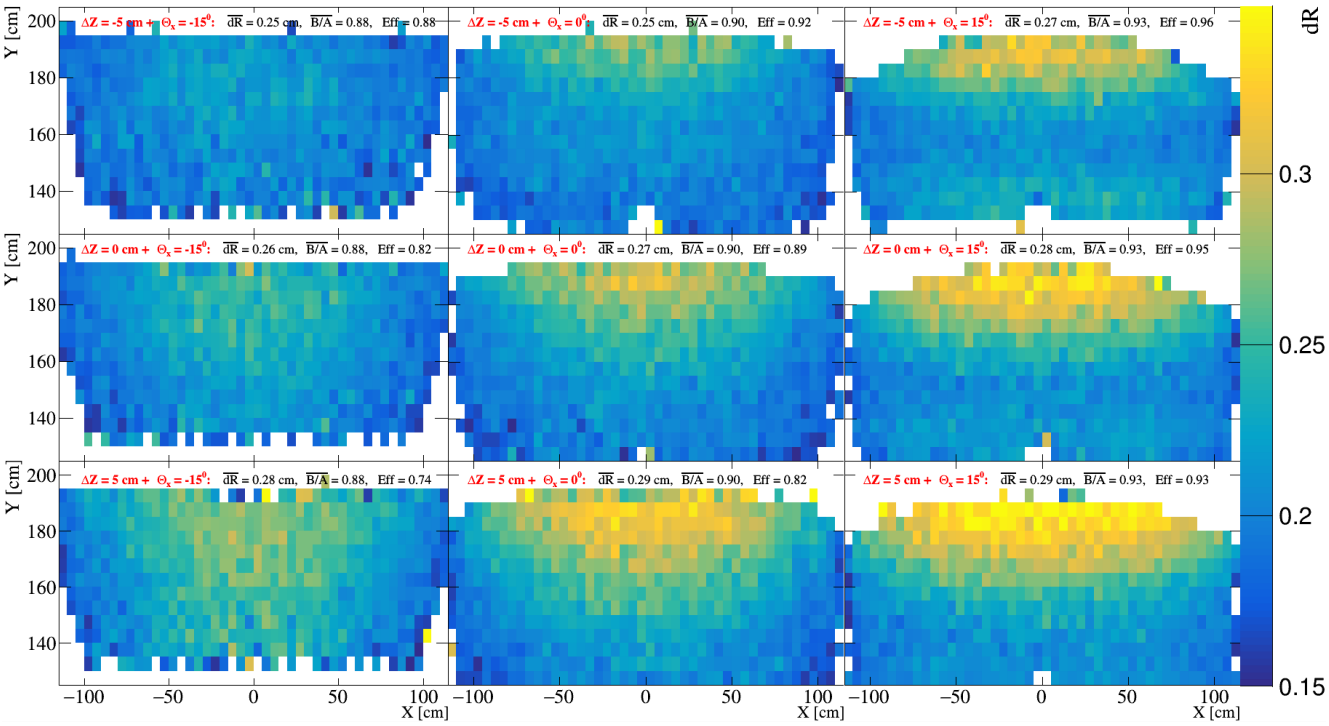

Figure 4.12: dR distributions for several different rotation angles θ_x and different ΔZ positions with fixed cylinder radius $R = 150$ cm. With black letters on every graph the mean values of dR, B/A, and efficiency are shown for each configuration. Different rotation angles θ_x and ΔZ positions are shown with red letters.

Taking into account all information mentioned above, one can make conclusion, that there is no dramatic difference in Cherenkov ring images during slight changes of R, θ_x, and Z parameters of the cylindrical geometry. The best parameters configuration obtained from the optimization process are: curvature radius of the cylindrical geometry $R = 150$ cm, the center position of the cylindrical PMT plane has coordinate $(0, 160, 228)$ cm relatively to the target, and the rotation angle around such middle point is $\theta_x = 15°$. The corresponding optimal parameters can be seen in Table 4.3.

Parameters applied in the final design slightly differ from the upper mentioned ideal parameters, due to the requirement to have additional space behind the PMT plane for readout electronic, for the cooling system and for a magnetic shielding box. The final parameters of the new cylindrical geometry for the CBM-RICH detector (also implemented in CbmRoot framework as "rich_v_17a" version) are: radius $R = 165$ cm, rotation angle $\theta_x = 18°$, center position of the PMT plane $(0, 160, 231)$ cm. As has been showed before in this chapter, such slight changes give very minor effect on the Cherenkov ring images, therefore no big difference is expected. The corresponding implemented parameters can be seen in Table 4.3.

	R	θ_x	center of the PMT camera
Optimal	150 cm	15°	$(0, 160, 228)$ cm
Implemented	165 cm	18°	$(0, 160, 231)$ cm

Table 4.3: Optimized parameters of the cylindrical photon detection camera.

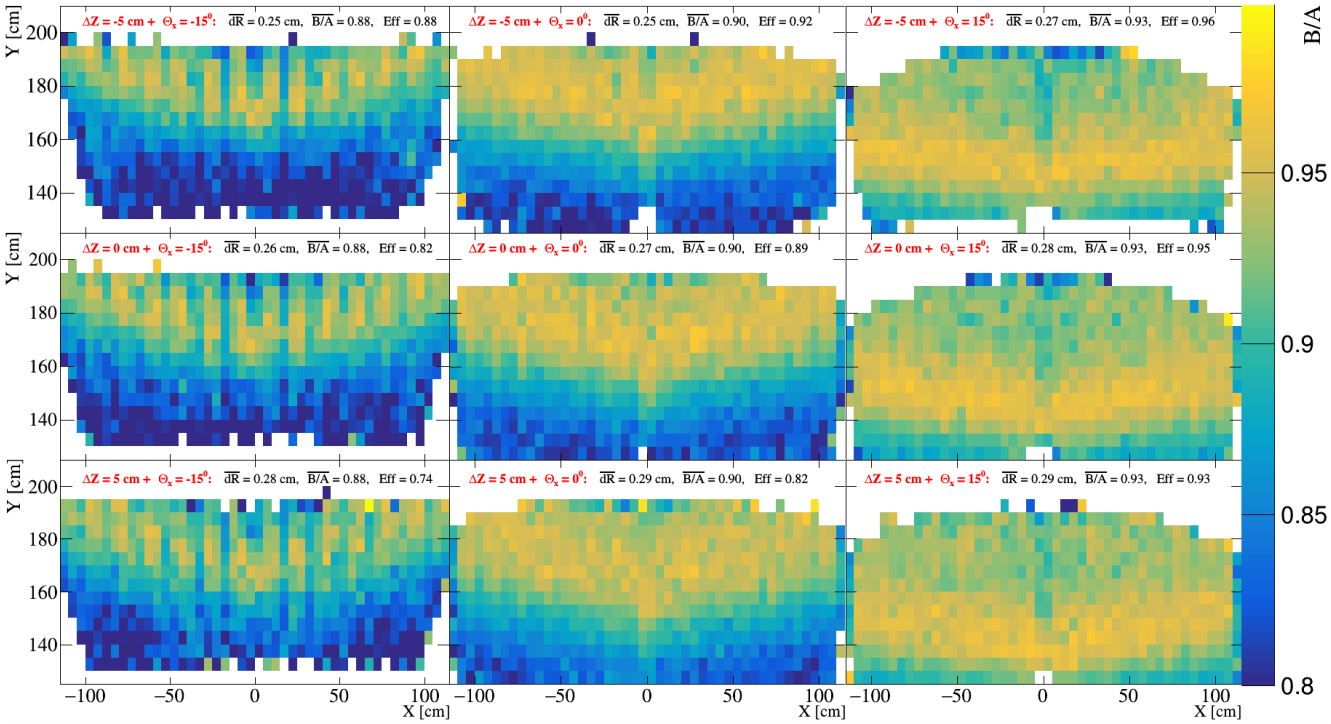

Figure 4.13: B/A distributions for several different rotation angles θ_x and different ΔZ positions with fixed cylinder radius $R = 150$ cm. With black letters on every graph the mean values of dR, B/A, and efficiency are shown for each configuration. Different rotation angles θ_x and ΔZ positions are shown with red letters.

4.3.3 Optimization of camera size

An additional question, which arose during the optimization process, is "which size of the cylindrical PMT plane should be used?". To answer such question a detailed physics simulation is required, since the size directly depends from the physics goals. The size optimization also takes into account another main aspect of the detector namely maximum possible acceptance coverage.

The cylindrical photon camera will be composed from small PCB backplanes (camera modules), each carrying 3×2 MAPMTs (see Figure 3.4). Such PCBs will be combined in vertical stripes of $5 - 7$ rows, and both halves of photon camera above and below the beam pipe will be composed from $14 - 16$ such stripes. This limitation comes from available amount of MAPMTs. Considering 16 stripes with 7 PCBs each, one will end up with 1344 MAPMTs, but maximum available amount of PMTs is only 1100. Therefore, some compromise is necessary.

Since the dilepton measurement is one of the important task at the CBM-RICH detector, the size optimization is done exactly for this particular measurement. In order to simulate only pure signal without any additional background, the Pluto generator was used as an event generator. The magnetic field in the simulation has a value of 0.7 Tm.

Figure 4.14 shows the simulation with implemented cylindrical geometry (with $R = 165$ cm and $\Theta = 18°$), consisting of 16 stripes with 7 PCBs each, for $\omega \to e^-e^+$ decay on the left side and $\rho \to e^-e^+$ decay on the right side. As can be seen from the pictures for dilepton decay channels of ω and ρ, 14 stripes per camera is fully enough, because most of the electrons from this decay channel are located in the middle part of the camera. On the other hand, it is obvious, that one can remove some MAPMTs in the middle-bottom region and in top corners of the camera, since they are barely covered with an interesting signal.

Doing dilepton analysis the proper description of background is another important task. The

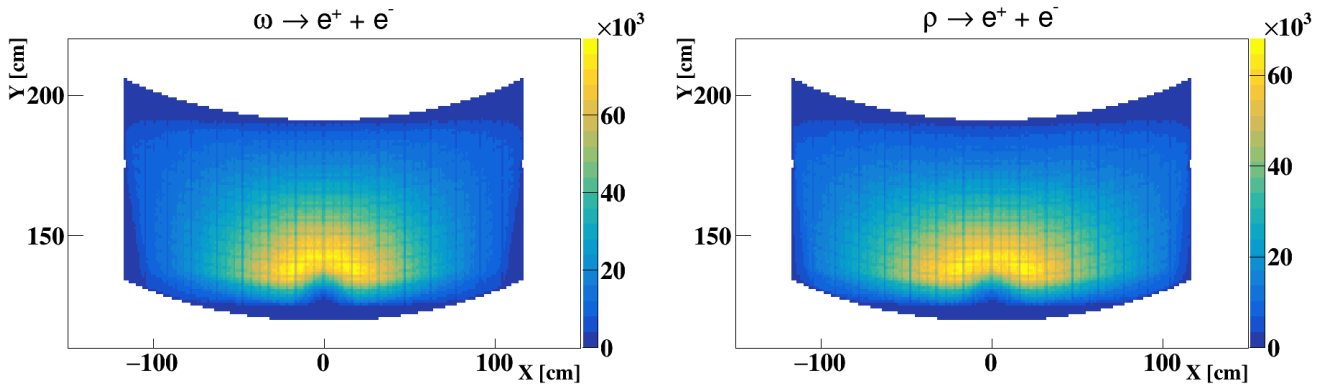

Figure 4.14: Pluto simulation for cylindrical geometry with 16 stripes with 7 PCBs each. Pictures show are hits from $\omega \to e^- + e^+$ decay (left) and from $\rho \to e^- + e^+$ decay (right) from 2.5 million simulated events at beam energy 8 AGeV.

small production cross section of vector mesons, together with their small branching ratio into e^+e^- make their reconstruction quite challenging because of the large physical background. The most of background for dileptons is coming from π^0 Dalitz decays ($\pi^0 \to \gamma + e^+ + e^-$) and from γ conversions ($\gamma \to e^+ + e^-$), which stem mainly from $\pi^0 \to \gamma + \gamma$ decay. Therefore, in Figure 4.15 is shown Cherenkov light on the extended PMT plane with 16 stripes coming from π^0 double photon decay on the left side, and from π^0 Dalitz decays on the right side.

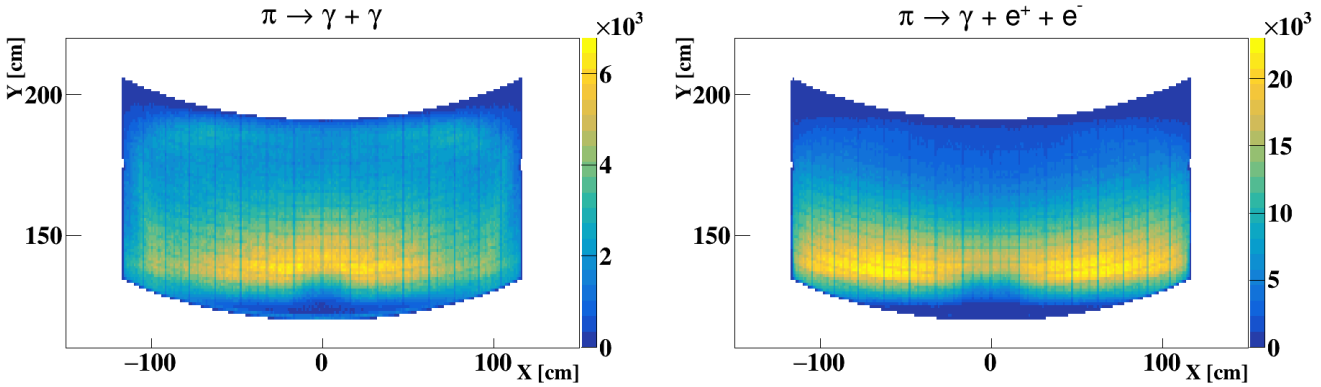

Figure 4.15: Pluto simulation for cylindrical geometry with 16 stripes with 7 PCBs each. Pictures show hits from $\pi^0 \to \gamma + \gamma$ decay (left) and from $\pi^0 \to \gamma + e^- + e^+$ decay (right) from 2.5 million simulated events at beam energy 8 AGeV.

As clearly seen in Figure 4.15, the outer upper corners of the plane as well as the middle bottom region are not relevant for any signal, therefore one can remove some MAPMTs there, but overall 7 PCBs per vertical strip is the optimal amount.

The amount of vertical stripes cannot be judged so easy as number of PCBs per vertical strip. The 14 stripes per one camera is fully enough for the dilepton detection. Adding two additional strips on the sides gives only ~ 3 % improvement for dilepton signal identification. On another hand, two additional stripes on the sides result in recording 10 % of additional electrons originating from π^0 decays (including photon conversions from them). This is particularly important, when one uses the RICH detector to reconstruct the direct photon signal, where it is essential to understand the background precisely from π^0 decays and to have it under control. To be able to detect as many of these electrons as possible it would be nice to have the enlarged PMT plane by adding one additional strip on each outer side, but due to the limited number of available

MAPMTs (1100) this enlargement is impossible to perform. In addition, it is planned not to use all available MAPMTs, but to have some part of them as spare, therefore, 14 stripes geometry with 7 modules along the Y-axis (excluding several purely populated outer MAPMTs) is the reasonable cylindrical geometry in order to perform reliable dilepton measurements.

4.4 Comparison of the performance between new cylindrical geometry and old wing-shaped geometry

In order to quantify the overall detector performance improvement due to the geometry optimization discussed above, a final comparison of the new optimized geometry (rich_v17a_1e) with old wing shaped geometry (rich_v16a_1e) is discussed here. To make such comparison, physics simulations for signal and background contributions are required. Here the comparison between old wing shaped geometry rich_v16a_1e and new cylindrically shaped geometry rich_v17a_1e (which has 14 strips with 7 PCBs each) is done. As was observed in the previous section, there is no visible difference between ρ and ω dilepton channels, therefore, here only $\omega \rightarrow e^+ + e^-$ will be considered as signal decay. As shown in previous section already, no big difference is observed for two main background channels $\pi^0 \rightarrow \gamma + e^+ + e^-$ and $\pi^0 \rightarrow \gamma + \gamma$. Hence, only π^0 Dalitz decay will be used as a background for the comparison between two different geometries.

The simulations are based on 2.5 million events, generated with the help of Pluto generator, and the magnetic field has value of 0.7 Tm. Main parameters for the comparison are dR, B/A, and efficiency. The relevant dR and B/A distributions using two geometries for $\omega \rightarrow e^+ + e^-$ and $\pi^0 \rightarrow \gamma + e^+ + e^-$ decays can be seen in Figure 4.16. The left column of plots in Figure 4.16 corresponds to simulations with wing-shaped geometry and the right column of plots correspond to simulations with cylindrical geometry. With blue letters on each graph the mean values of dR, B/A, and efficiency over full PMT plane are shown. Both geometries are located almost in the same position, have similar rotation angle, and have comparable size, but the main difference between two geometries is their shape, hence plots in Figure 4.16 show similar distributions behavior.

There is a tiny difference between two geometries in mean dR, $\overline{B/A}$, and efficiency, where the cylindrical geometry is slightly better (for example, for wing-shaped $\overline{B/A} = 0.91$ and for cylindrical $\overline{B/A} = 0.94$), but overall both geometries give comparatively good performance. Taking into account that such wing-shaped geometry can not be built because of additional dead space in the middle, one can make conclusion, that the cylindrical geometry is much suitable for the data taking, and, therefore, is chosen as new default geometry for the CBM-RICH detector.

4.5 Summary and conclusions from the geometry optimization

Result of the optimization, which has been discussed in this chapter, is a basis for the new standard geometry rich_v17a_1e with parameters based on the optimization studies shown in this thesis. As a result of studies, the standard geometry has been changed from the idealized wing geometry towards the mechanically more realistic cylindrical geometry.

Cylindrical parameters R, Z, and θ_x implemented in rich_v17a_1e geometry slightly deviate from the optimal one due to geometry constrains. The studies in this chapter give an idea how sensitive two main optical quality parameters (dR and B/A) of Cherenkov rings are. It was found, that the dependence of optical parameters from slight changes of R, Z, and θ_x is quite weak.

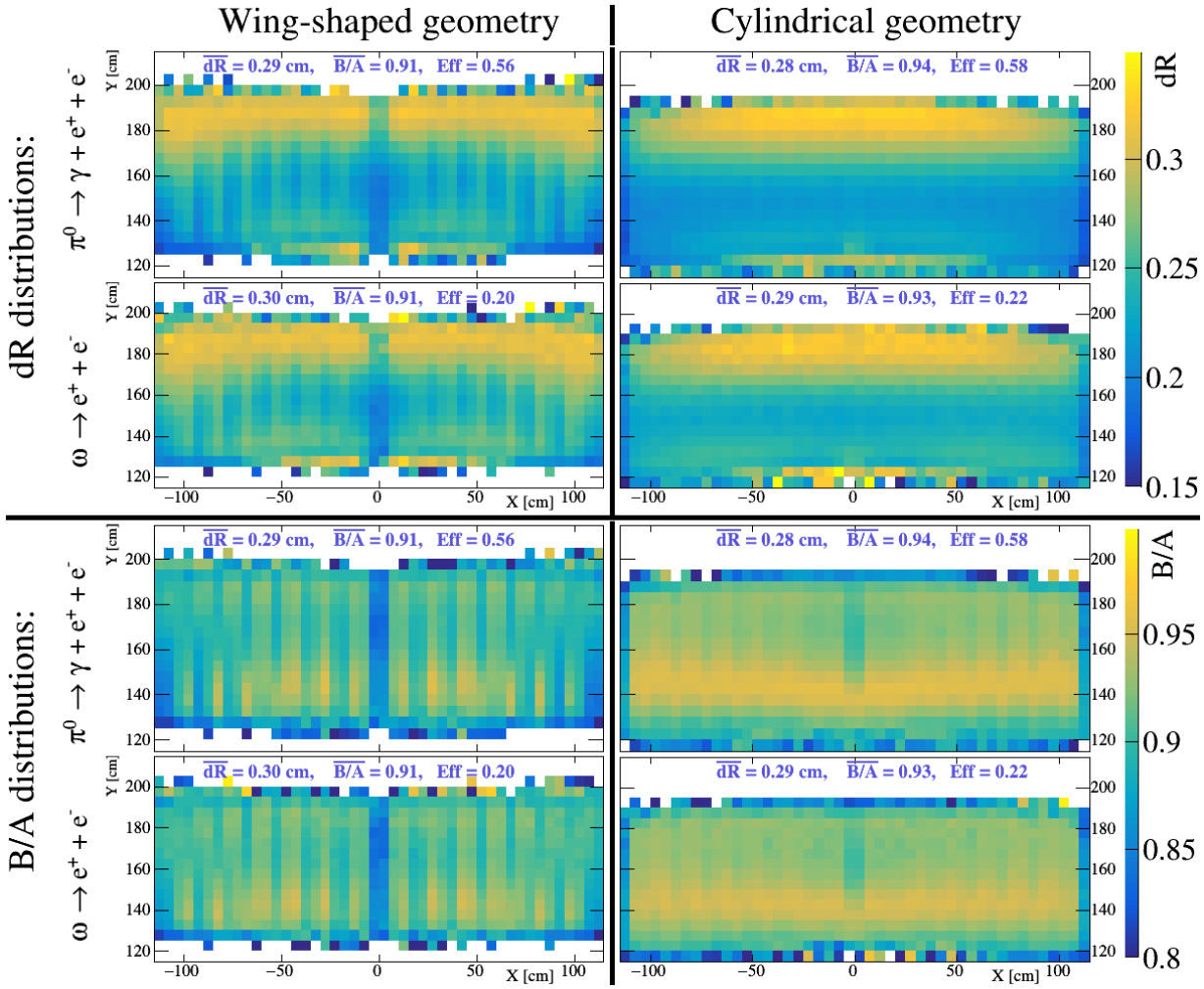

Figure 4.16: The relevant dR and B/A distributions using two geometries for $\omega \rightarrow e^+ + e^-$ and $\pi^0 \rightarrow \gamma + e^+ + e^-$ decays. With blue letters on each graph the mean values of dR, B/A, and efficiency over full PMT plane are shown.

The mechanical design of the cylindrical geometry can be realized for the CBM-RICH detector, since it takes into account the requirement of the additional space behind photon detection plane for readout electronics. The new standard geometry rich_v17a_1e is now used in all further simulations. The final numbers, which are implemented in the cylindrical geometry, are summarized in Table 4.4.

Parameter	Camera radius	Camera angle	X position	Y position	Z position
Value	$R = 165$ cm	$\Theta_x = 18°$	0 cm	160 cm	231 cm

Table 4.4: Final result from geometry optimization of the CBM-RICH photon detection camera. The following parameters are implemented in the new standard geometry rich_v17a_1e.

5 Reconstruction of neutral mesons using double conversion

One of the main goals of the CBM physics program is dilepton measurements. The measured invariant mass spectrum of dileptons contains the actual signal and a significant part of background coming from hadron decays. In order to perform an analysis of the dilepton invariant mass spectrum, one needs to estimate and subtract the background contribution first. The purity of the final dilepton spectrum directly depends on the accuracy of the background estimation. Therefore, a quantitative modeling of background is an essential task for proper understanding of the invariant mass spectrum of dileptons.

The data analysis from these heavy ion collision experiments shows that a significant part of background comes from π^0 and η decays. In order to model the background contribution originating from decays of these mesons one needs not only to reconstruct, but also to count them quantitatively. There are two possibilities in the CBM experiment to reconstruct these mesons: via direct measurement of their decay photons with the ECAL detector or via indirect reconstruction of these photons after conversion into e^+e^-. Here, only the conversion method is considered.

In this chapter several important aspects on the meson reconstruction are discussed. Since the analysis in this thesis is based on simulation data, the important aspects of used frameworks for simulations are described. Later on, central aspects and selection criteria of the simulation are discussed, including the estimation of cut values to be applied on reconstructed tracks to have highest efficiency in signal reconstruction with optimally suppressed background. In the last section is shown the connection to previous works with conversion analysis studies for the CBM experiment.

5.1 The CbmRoot simulation Framework

The simulation studies presented in this work are performed using the CbmRoot software, which is part of the FairRoot software package [58]. The FairRoot framework is fully based on the ROOT system [59] developed at CERN and commonly used for high-energy physics analysis. The CbmRoot simulation framework has been developed for the analysis of data within CBM experiment, as well as for feasibility studies and optimization of the detector layout. With the

help of CbmRoot framework, users can create realistic simulated data and perform reconstruction analysis.

Particles are propagated through CBM sub-detectors, which have been introduced in the previous sections, using Geant3 or Geant4 transport engines. The user code which creates simulated data does not depend on a particular Monte Carlo engine. As event generator UrQMD (Ultra-relativistic Quantum Molecular Dynamics), PLUTO, or HSD (Hadron-String Dynamics) can be used. As a standard generator for the CBM experiment is used the UrQMD [60] model, although this code does not include rare probes interesting for CBM physics. Those rare decay channels can be additionally embedded using the PLUTO generator [57] with correct decay kinematics of hadronic and electromagnetic decays.

The UrQMD model is used to simulate (ultra)relativistic heavy-ion collisions from the most important accelerators. The model shows a fair overall agreement with experimental data over a wide range of energies.

The detector responses in the framework are implemented as realistically as possible, e.g. obtained from measurements with prototypes in test beams. The mechanical design of detectors is still implemented very roughly since the detailed structures and the supporting materials are still under investigation.

During simulation and reconstruction procedure many classes from the underlying framework are used and corresponding data structures are filled, which can than be used for further analyses. The most important of these data structures are MCTrack and GlobalTrack arrays.

- **MCTrack** :

  The MCTrack array is dedicated to store track information for all tracks generated during the simulation of particles, which hit any detector at least one time. All information stored in this array is called MCtrue information, and contains momentum of the particle, starting vertex position, energy loss, particle type, its mother particle ID (i.e. all available information from Geant). Using the MCtrue information one can check, for example, whether a particle was reconstructed correctly or not.

- **GlobalTrack** :

  The GlobalTrack array contains only reconstructed tracks. Global track reconstruction is based on STS track reconstruction, therefore, in this array one can find only tracks, which were reconstructed in STS. All tracks have at least 3 hits in the STS detector, since this is a minimum requirement for STS track reconstruction. This array contains pointers to other classes from where one can extract reconstructed information about hit positions, particle ID, energy loss, and momentum from all participating detectors.

Detector	Target	Magnet	Mag. field	pipe	MVD	STS	RICH
Geometry version	250 μm, gold	v15a	v12b	v16b_1e	v17a_tr	v16g	v17a_1e

Table 5.1: CBM detector configuration used for simulations described in this thesis.

The results shown in this chapter are based on 15×10^6 simulated UrQMD events of central Au+Au collisions at beam energy of 8 AGeV. The CBM detector configuration used in simulations is shown in Table 5.1. Other detectors, as TRD, TOF, ECAL, PSD, were not included in the simulation. The RICH geometry v17a_1e corresponds to the new cylindrical geometry, optimization of which was discussed in the previous chapter.

5.2 Conversion method

The conversion method for reconstruction of photons has been already successfully applied in the analysis of data from heavy ion collider experiments like PHENIX and ALICE, and as well in experiments with a fixed target, like the HADES experiment. Usually, the conversion method is used as a complementary approach to the direct measurement of photons using an electromagnetic calorimeter.

The main idea of the conversion method is to measure photons indirectly by detecting e^+e^- pairs from conversion of $\gamma \rightarrow e^+e^-$ in the target or in the material of the detectors. There are several sources of photons in heavy ion collisions, but only three of them are interesting for this thesis: π^0 and η decays, and direct photons, stemming from primary interactions within the fireball. The biggest amount of all photons originates from π^0 decays. At heavy ion collisions in the typical energy regime of CBM, about 200 π^0 are created during one central Au+Au collision. The two other interesting sources of photons are not so abundant: a few *direct* photons and η mesons per event are produced in one central Au+Au collision.

The π^0 and η mesons have two common decay channels, relevant for conversion analysis:

- a double photon decay channel: $\pi^0/\eta \rightarrow \gamma + \gamma$,
- a so-called Dalitz decay channel: $\pi^0/\eta \rightarrow \gamma + e^+ + e^-$.

The detailed analysis of these sources is given later in this thesis.

The good position and time precision of the tracking system together with the very good electron identification properties of the RICH detector allow to reconstruct γ using the conversion method very precisely.

Such reconstructed photons can be further combined in pairs to form π^0 and η mesons from their $\pi^0/\eta \rightarrow \gamma + \gamma$ decays. Taking into account the fact, that the Dalitz decay channel of neutral mesons is proceeding through intermediate state with imaginary photon ($\pi^0/\eta \rightarrow \gamma + \gamma^* \rightarrow \gamma + e^+ + e^-$), it can be also reconstructed with help of the conversion method. The difference between real and imaginary photon is in the invariant mass. However, due to limited precision in the reconstruction of lepton energy and momentum, the resulting invariant mass resolution is not sufficient to distinguish the Dalitz decay channel $\pi^0/\eta \rightarrow \gamma + e^+ + e^-$ from a real 2 photon decay $\pi^0/\eta \rightarrow \gamma + \gamma$ on an event-by-event basis.

The direct and indirect measurements of photons are complementary and will be both employed in the CBM experiment. Both methods have their own advantages and disadvantages.

The big advantage of the ECAL detector is its high efficiency of photon registration. However, due its position in the CBM experiment behind all other detectors, also due to limited size, only small part of CBM acceptance is covered. Hence, a lot of photons will not be detected. In addition, because of the position of the calorimeter, the background due to conversions in the material budget in front of the ECAL is enhanced.

The big advantage of the conversion method is the better invariant mass resolution of reconstructed π^0 and η, since the momentum resolution of combined electrons and positrons is defined by STS momentum resolution, which is much better than the photon energy resolution of any calorimeter. The main disadvantage is the relatively small (about 5 %) conversion probability of photons, since photons must be converted either in the target, or in the material of the MVD or first 5 STS stations (at least 3 hits in STS for track reconstruction are required). The conversion probability is small, because the MVD and the STS have been developed with low material budget in order to reduce the conversion rate.

5.3 Conversion points

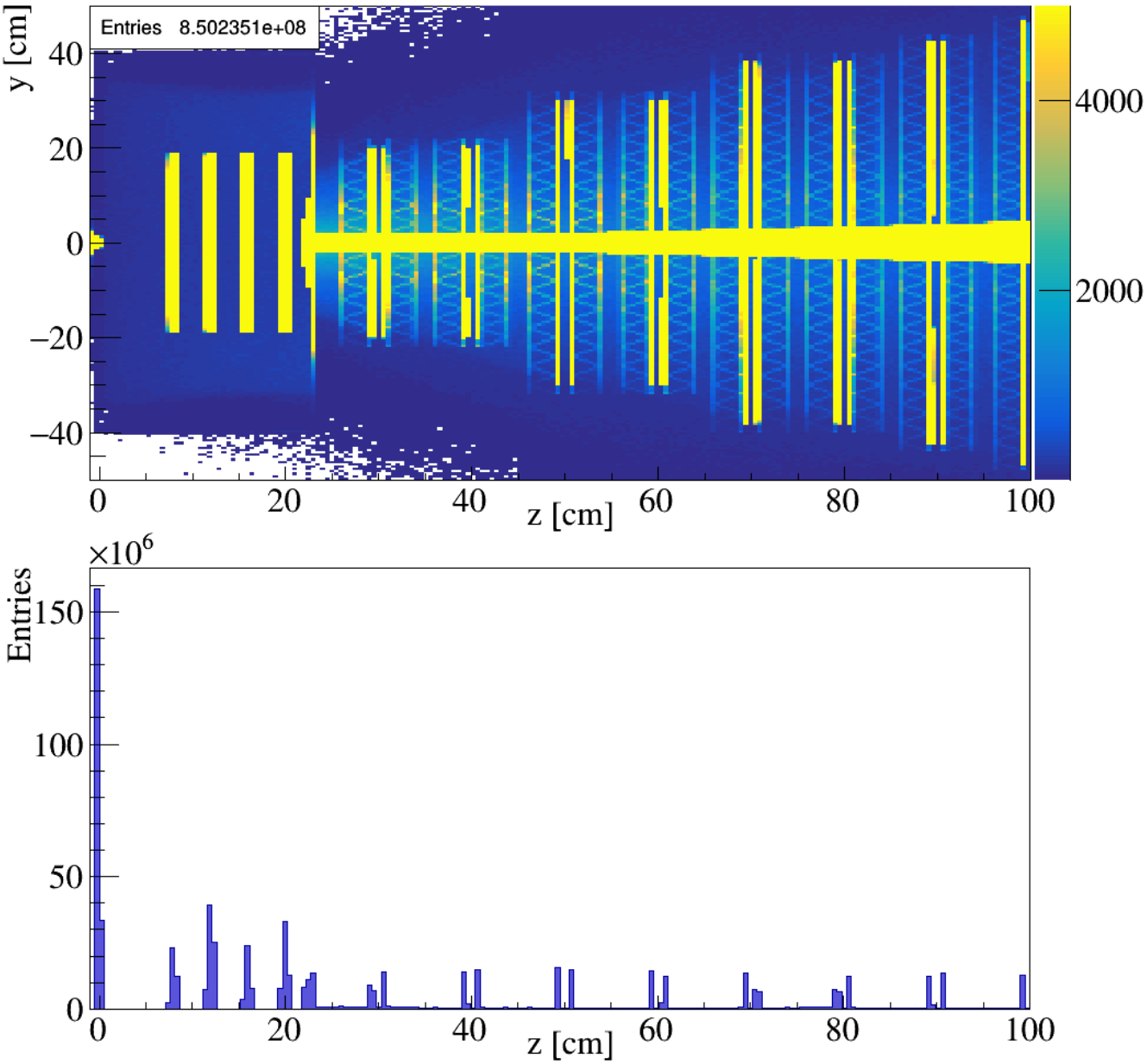

Figure 5.1: Start vertices of leptons coming from conversion of photons (taken from MCTracks array). Vertical yellow lines on top picture and blue lines on bottom picture display target position ($0-1$ cm), four MVD stations ($z = 8-20$ cm), and eight STS stations ($z = 30-100$ cm). Several additional sources of conversion are also recognizable on pictures: beam pipe inside the STS detector, carbon ladder holding structures of the STS detector, and exit window from the vacuum box of the MVD detector (~ 23 cm).

In order to perform a photon conversion analysis, the position-dependent conversion probability should be studied first. Photons can convert into e^+e^- pair only within detector material in order to preserve 4-momentum conservation. There are three main conversion sources before the RICH detector: the target, the MVD, and the STS. The first two will be placed in the vacuum, and the last one in a box with dry and cold CO_2 gas at normal pressure, hence one can expect conversions mainly in detector material or in the target.

One way to study the position-dependent conversion probability is to use simulations. As basis only the MCtrue information from the simulation is used. The MCTrack data is used instead of GlobalTrack, because the real conversion probability is needed. Usage of MCtrue information allows to reconstruct the conversion vertex density independently from the reconstruction capabilities of detectors.

Geant is used for the simulation of all physics processes during the passage of particles through the detector, in particular including possible conversion process of photons. During the simulation process, the originating vertices of all particles are stored in a data structure, and can be later analyzed without depending on the detector reconstruction capabilities. Among all types of particles only electrons and positrons were selected, which stem from the conversion of a photon, and their start vertices are recorded as conversion coordinates (see top picture in Figure 5.1). In order to see the conversion probability more clearly, the top picture from Figure 5.1 is projected onto the z-axis. The result is shown on bottom picture in Figure 5.1. As can be seen in Figure 5.1 the main sources of conversions are detector materials and the target.

One can see from Figure 5.1, that ~ 28 % of conversions happens in the target ($z = 0 - 1$ cm), another $\sim$ 29 % in MVD + vacuum box material, and the rest of 43 % belongs to STS + pipe material. Interesting fact can be remarked, that amount of converted photons in MVD ($z = 5 - 25$ cm) and in STS ($z = 30 - 100$ cm) differs only by 14 %, although the area of MVD detector is in several times smaller than the STS detector.

5.4 KFParticle secondary vertex finder

During the standard track reconstruction of STS tracks, each particle is expected to originate from the primary vertex and is fitted accordingly. Since almost 3/4 of conversions happen in the detector material, electrons and positrons from such conversion after standard track reconstruction will have wrongly reconstructed momenta, which leads to misidentification and other problems. Therefore, some additional tool is needed for this particular purpose.

A dedicated software package "KFParticle" [61] can be used for reconstruction of secondary vertices outside the target. This software has been originally developed for complete reconstruction of short-lived particles, but it also provides many standalone features for users. The package is based on the Kalman filter method [62]. The Kalman filter method is a recursive method for analysis of linear discrete dynamic systems described by a vector of parameters. The method allows to find an optimal estimation of the particle track parameters and to achieve high accuracy [63].

The important feature from KFParticle package used here is a search of the point of closest approach between two particles. In our particular case it will be used to find out the possible intersection point between negative and positive tracks in order to reconstruct converted γ particles.

The difficulty of finding the point of closest approach of two tracks is coming from non-homogeneous magnetic field in the CBM experiment. This can be solved only by numerical approximation method. Considering the case when two particles fly in a constant one-component

magnetic field B_z, the equation of motion of each particle is described by the following formulas:

$$
\begin{aligned}
x &= \left(x_0 + \frac{p_{y0}}{qB_z}\right) + \frac{p_{x0}}{qB_z}\sin(qB_z s) - \frac{p_{y0}}{qB_z}\cos(qB_z s),\\
y &= \left(y_0 + \frac{p_{x0}}{qB_z}\right) + \frac{p_{x0}}{qB_z}\sin(qB_z s) + \frac{p_{y0}}{qB_z}\cos(qB_z s),\\
z &= z_0 + s p_{z0},\\
p_x &= \frac{p_{x0}}{qB_z} - \frac{p_{x0}}{qB_z}\cos(qB_z s) + \frac{p_{y0}}{qB_z}\sin(qB_z s),\\
p_y &= \frac{p_{x0}}{qB_z} - \frac{p_{x0}}{qB_z}\sin(qB_z s) - \frac{p_{y0}}{qB_z}\cos(qB_z s),\\
p_z &= p_{z0},
\end{aligned}
$$

where $s = l/p$, l is a distance of propagation, p is a total momentum of the particle, q is the charge of the particle, $\{x_0, y_0, z_0\}$ is an initial position of the particle, $\{p_{x0}, p_{y0}, p_{z0}\}$ are initial components of its momentum. Such assumptions are valid in case of the smooth behavior of the magnetic field and small extrapolation distances.

The point of the closest approach for two particles can now be found by minimizing the distance between their trajectories R as:

$$
\begin{aligned}
R &= \sqrt{(x_1(s_1) - x_2(s_2))^2 + (y_1(s_1) - y_2(s_2))^2 + (z_1(s_1) - z_2(s_2))^2},\\
\frac{dR}{ds_1} &= 0,\\
\frac{dR}{ds_2} &= 0,
\end{aligned}
$$

Solving the system of equations on parameters s_1 and s_2 for first and second particle correspondingly, it is possible to find an exact solution in the transverse XY plane and then add a small correction on the z coordinate.

Solving such equation system, two points in XY plane can be found, what makes ambiguity in the vertex. Based on errors of those points the following two cases can arise (see Figure 5.2):

1. If the points are well separated with a significance beyond 5σ, then the point where two particles are closer taking into account the z coordinate is selected (see left picture in Figure 5.2).

2. If the points are not separated significantly, then the middle point is selected as intersection point (see right picture in Figure 5.2).

The selected intersection point is shown in Figure 5.2 with light-blue color. In a second step, the obtained point is corrected on z-coordinate. The corrected point is shown with red dot in Figure 5.2.

The use of this feature from the user's point of view is relatively simple: the user has to provide two tracks into KFParticle package together with an assumption on their particle ID in order to find a possible intersection point between them. The software will search the point of closest approach between these two tracks using above mentioned method. When the point is found, the two tracks are fitted to this common vertex point and corresponding momenta are assigned to these tracks. The user can afterwards simply extract all information of interest: the three component coordinate of the point of closest approach, corresponding three-momenta for each track, and their errors.

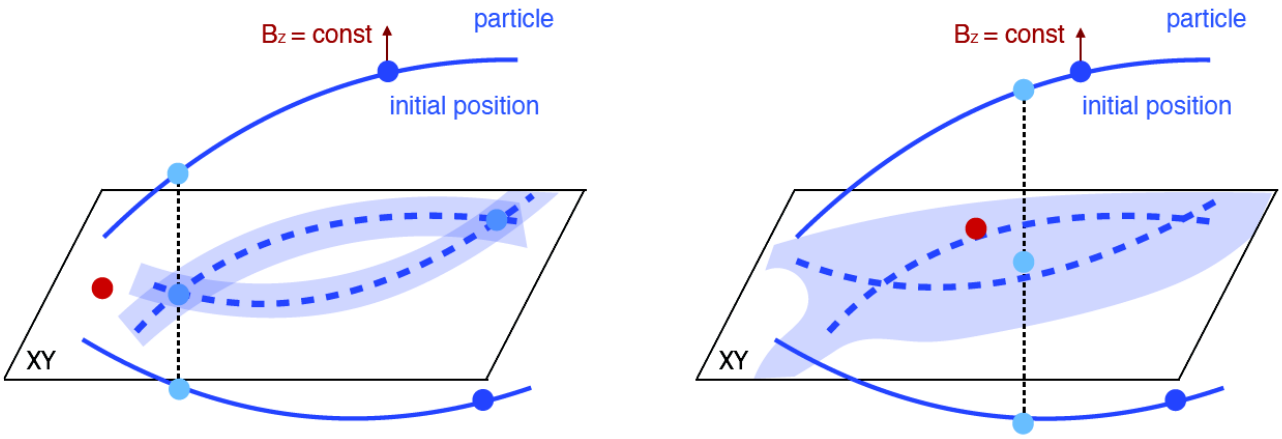

Figure 5.2: Two possible solutions of the equation system [61]. The left picture shows the case when two found points in XY plane are well separated within 5σ errors. The right picture shows the case when two found points in XY plane are not separated within 5σ errors. Dashed lines represent projection of tracks into XY plane. Shaded area show uncertainty of each track.

5.5 Details of reconstruction

The CBM experiment is dedicated to measure a dilepton invariant mass spectrum with high accuracy at high interaction rates. In order to do so, a proper description of the background is needed. Since the most of the background is coming from π^0 and η, the proper analysis of these mesons is required.

As a starting point, the number of generated π^0 and η mesons per event should be investigated. In central Au+Au collisions at CBM energies it is expected, that around 200 π^0 and 10 η per event will be produced. These particles themselves do not affect the dilepton spectrum, but their decay products do. The relevant decay channels for conversion analysis of π^0 and η are:

- $\pi^0/\eta \rightarrow \gamma + \gamma$
- $\pi^0/\eta \rightarrow \gamma + e^+ + e^-$

The first decay channel into two gammas is the dominant decay channel of neutral mesons. It has a branching ratio (BR) of 98.8 % for π^0 and 38.8 % for η. The second one has the BR of around 1.17 % for π^0 and around 0.5 % for η. All other possible decay channels of π^0 will not be considered at all, due to their very low branching ratios. A possibility to reconstruct other η decay channels via conversion method will be discussed in Chapter 7.

From the physical point of view, only Dalitz decays should cause background contribution in the dilepton spectrum, but in reality it is different: additional dilepton pairs can appear from conversion of photons within some material. After such interaction a photon will be converted into a e^+e^- pair following energy and momentum conservation. The photon conversion probability is relatively small, but since the amount of photons per event is around 400 it nevertheless causes significant contribution into the dilepton spectrum.

In order to reconstruct π^0 and η via conversion method from the experimental data, one needs to reconstruct γ particles first. This can be achieved with help of the RICH detector, by combining identified e^+e^- into pairs to form converted photons.

Separation on tracks with primary and secondary vertices

In a first step, all tracks are divided in two groups: primary tracks and secondary tracks. Primary tracks are tracks pointing to the primary vertex. They are caused by particles created directly in the collision process of beam and target. Tracks of particles from resonances and from photon conversions in the target are also considered as primary tracks, since they are produced directly at the point of the primary vertex and can not be distinguished from tracks produced directly in the collision.

Other particles produced in heavy ion collisions have sufficient lifetime to move away from the primary vertex and decay later (for example, strange mesons or multi-strange hyperons). When such particles are decaying, they can produce additional charged particles, which can be also registered in the tracking system, but which do not point to the primary vertex. Tracks of such charged particles are called secondary tracks. Tracks of electrons and positrons from conversions at the detector material are considered as secondary tracks.

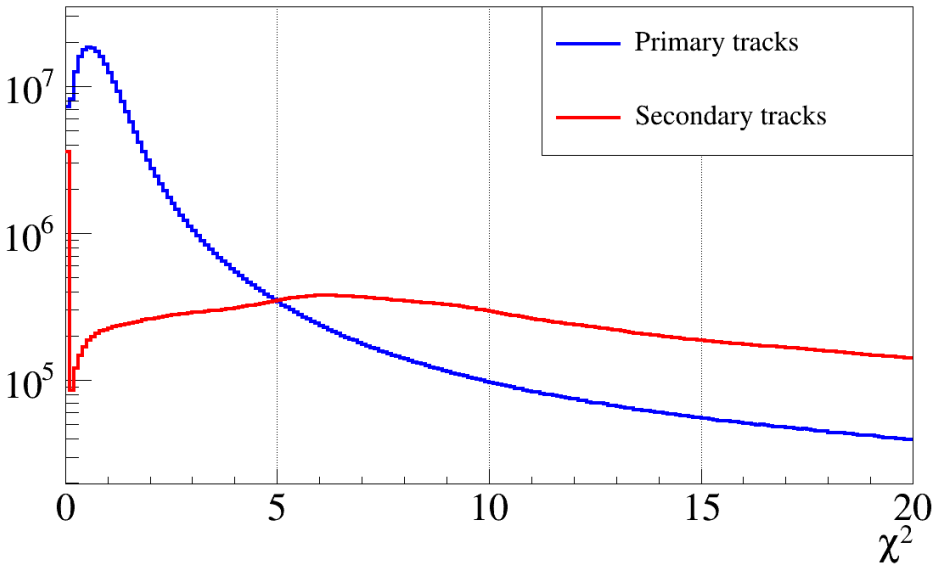

Figure 5.3: Distributions of normalized χ^2 from the standard fitter, fitting all tracks to the primary vertex.

The separation between primary and secondary tracks can be done based on χ^2 criteria. All tracks from the GlobalTrack array initially are fitted with a standard fitter to the primary vertex, getting a normalized χ^2 value as a quality criteria for the fit. The χ^2 from a standard fitter for primary and secondary tracks can be seen in Figure 5.3 with blue and red colors correspondingly. If $\chi^2_{fit} < 5$, than the track is considered as a primary track, otherwise as a secondary track. In addition, all tracks are divided into positive and negative subgroups depending on their charges. Thus, four groups are formed:

- primary positive tracks,
- primary negative tracks,
- secondary positive tracks,
- secondary negative tracks.

When analyzing reconstructed data, it is necessary to apply certain cuts to filter out background and to consider only relevant candidates for further analysis. The essential cuts for photon reconstruction via conversion as well as subsequent cuts on photon pairs are presented below.

Use of the RICH for pion suppression

A large fraction of tracks saved in the previous step are charged pions, which are of no interest for the analysis presented here. Therefore, one needs to reduce their amount as much as possible. In order to do so the RICH detector can be used. Due to the technical design of RICH all electrons and positrons, which reach the detector, produce Cherenkov rings. This feature can be used for pion suppression: all tracks, which reach the RICH detector and do not produce Cherenkov rings can be excluded from the analysis, assuming they are pions. This will not remove all pions from the saved groups, because pions with momenta higher than $p = 5$ GeV/c also produce rings in the CBM-RICH detector, but it will significantly reduce them. Some low energetic pions will also prevail due to misidentification of low energetic pions as electrons in the RICH detector.

Photon conversion in the target and outside the target

When all tracks are sorted and pions are suppressed, converted photons can be reconstructed.

In a first step, photons with a point of conversion inside the target are reconstructed. For this, primary positive and primary negative tracks are fitted to the primary vertex using a standard fitter, and corresponding momenta are assigned. By sorting all possible combinations with one primary positive and one primary negative track one forms the candidates of converted photons. Later on, additional cuts will be applied on these candidates in order to reduce the amount of false pairs.

In a second step, photons with conversion vertices outside the target are reconstructed. Since we are interested only in reconstruction of converted photons, each pair of combined tracks has to have a common starting vertex (assumed conversion point). To find out such common vertex, one can use KFParticle secondary vertex finder. For every possible combination of one secondary positive track and one secondary negative track the KFParticle utility is called, using the assumption on the particle ID of being positron and electron. The software will try to find the point of closest approach between these two tracks, and fit both tracks to the common vertex. If the found vertex does not lie between the target and the 5^{th} station of STS detector in beam direction (i.e. not between $z = 0 - 70$ cm) the candidate pair is considered as a false pair, otherwise - as a candidate for a converted photon. On all accepted pairs additional cuts will be applied later in order to reduce the amount of false pairs even further.

Cuts for identification in the RICH

The identification of electrons and positrons in the CBM-RICH detector is one of the important steps for the reconstruction of converted photons. Due to the choice of CO_2 at normal pressure as radiator gas, pions with momenta $p > 4.7$ GeV/c as well as electrons and positrons with any momenta entering the RICH detector will produce Cherenkov light. The typical radius of Cherenkov ring produced by electrons and positrons is ~ 5 cm. For pions, their radius increases with increasing momenta, starting at a threshold momentum of $p_{th} = 4.7$ GeV/c.

Considering our reconstruction goals, at beam energies up to 11 AGeV, almost all electrons from photon conversion have momenta $p < 4.7$ GeV/c. Therefore, for the ring identification in the RICH detector it is reasonable to use cuts on the ring parameters in combination with corresponding momenta cuts. In the analysis instead of assuming a perfect ring image, we fit an ellipse to the projected ring image with minor axis (B) and major axis (A) as parameters. The mean value for A and B parameters for electrons and positrons in the present cylindrical RICH geometry are ~ 5.1 cm and ~ 4.8 cm correspondingly. The A and B distributions from the ellipse fit can be seen in Figure 5.4 on the left and right side correspondingly. The optimum compromise

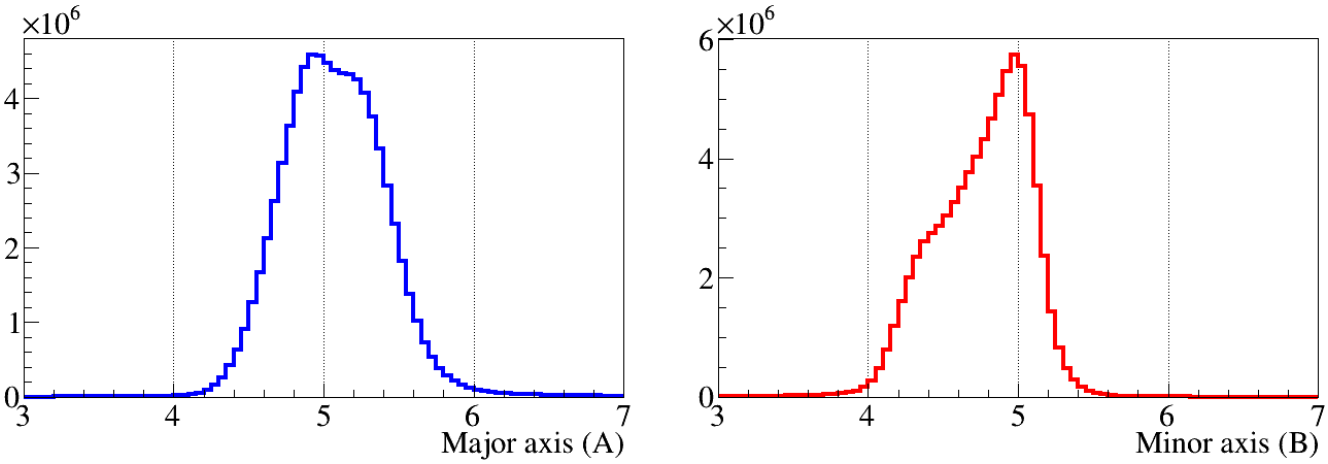

Figure 5.4: Major axis (A) and minor axis (B) distributions from the ellipse fit of projected ring images coming from electrons and positrons.

between good electron identification and a decent amount of background can be achieved with the following cuts:

- 4 cm $< A <$ 6 cm,
- 4 cm $< B <$ 6 cm,
- 0.2 GeV/c $< p <$ 4.7 GeV/c.

The minimum value for A, B = 4 cm is chosen in order to exclude cases, when an electron is wrongly assigned to a ring produced by a pion. The maximum value for A, B = 6 cm helps to avoid wrongly found rings, for example, when two rings are so close to each other, that the ring finder takes half of hits from first ring, and second half - from second ring. All tracks with momenta $p >$ 4.7 GeV/c are excluded from further analysis due to the high pion contamination in this momentum range. A lower limit of momenta is needed in order to avoid wrong matches between rings and very low momenta electrons, which will not reach the RICH detector due to magnetic field.

Opening angle cut

One of the important cuts for conversion analysis is opening angle $\Theta_{e^+e^-}$ of the electron-positron pair from the converted photon. Due to the vanishing mass of photons this opening angle should be equal 0. Due to reconstruction uncertainties it will not be exactly zero, but very small. On the other hand, most of false combinations will have big opening angle up to 180 degree. Therefore, the opening angle is considered as a good selection criteria for photon reconstruction.

To derive the optimal value for the opening angle cut, the reconstructed data together with MCtrue information is used. All reconstructed tracks are combined into pairs consisting of positive and negative tracks. With help of MCtrue data, these pairs are sorted into two groups: pairs which indeed stem from the same photon conversion process, and all other falsely reconstructed pairs. Opening angle distributions for both cases were analyzed individually, the result can be seen in Figure 5.5.

Comparing the two graphs with correct and false pairs, two alternative cuts on opening angle are suggested for further analysis process:

- $\Theta_{e^+e^-} < 1°$

- $\Theta_{e^+e^-} < 2°$

Using the first value, $\Theta_{e^+e^-} < 1°$, about ~ 58 % of all correct pairs will be reconstructed, and signal to background ratio will be ~ 60 %. Using the second value, $\Theta_{e^+e^-} < 2°$, about ~ 76 % of all correct pairs will be reconstructed, and signal to background ratio will be ~ 37 %. Both values of the cut will exclude a huge amount of unnecessary background.

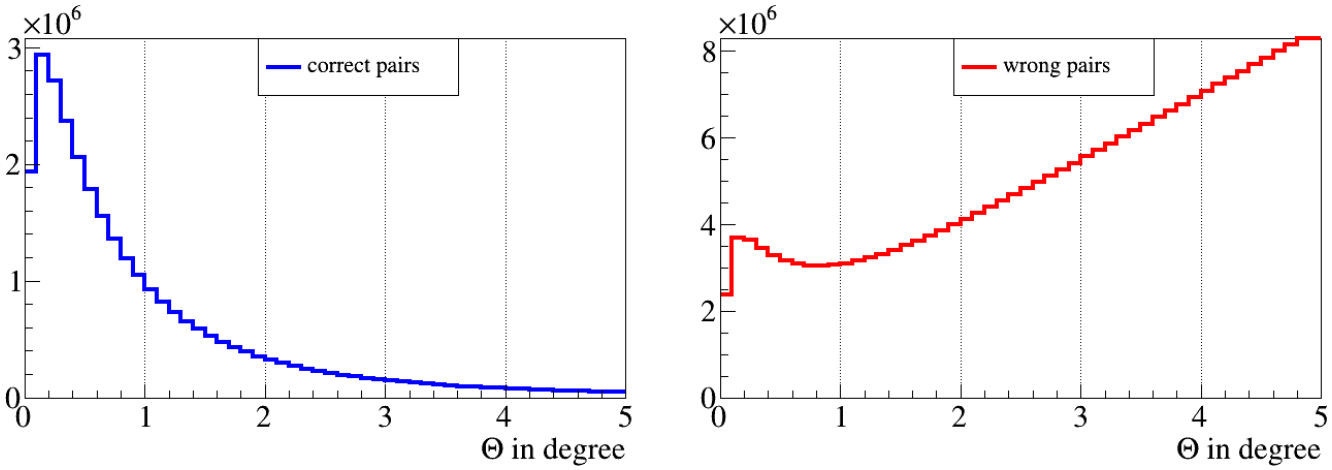

Figure 5.5: Opening angle distributions between two combined particles for correctly combined (left, blue) and wrongly combined (right, red) pairs of tracks.

Invariant mass cut

Another important cut in conversion analysis is based on the invariant mass m_{inv} of the electron-positron pair from the converted photon. This cut is closely related to opening angle cut and it will give almost the same improvement for the selection of true e^+e^- pairs, as the opening angle cut. Since a photon conversion happens in the vicinity of material budget, a fraction of the momentum is transfered to the surrounding atoms in the conversion process. Therefore, invariant mass of reconstructed e^+e^- pair will never be exactly zero, but close to.

To derive the optimal value for invariant mass of the lepton pairs, the same method as for the opening angle was applied (using the reconstructed data together with MCtrue information). The corresponding histograms can be seen for correct and for false pairs in Figure 5.6.

Comparing the two graphs with correct and false pairs, two alternative cuts on the invariant mass are suggested for further analysis process:

- $m_{inv}(e^+e^-) < 10$ MeV/c^2
- $m_{inv}(e^+e^-) < 20$ MeV/c^2

Using the first value, $m_{inv}(e^+e^-) < 10$ MeV/c^2, about ~ 69 % of all correct pairs will be reconstructed, and signal to background ratio will be ~ 45 %. Using the second value, $m_{inv}(e^+e^-) < 20$ MeV/c^2, about ~ 83 % of all correct pairs will be reconstructed, and signal to background ratio will be ~ 23 %. Both values of the cut will exclude a huge amount of unnecessary background.

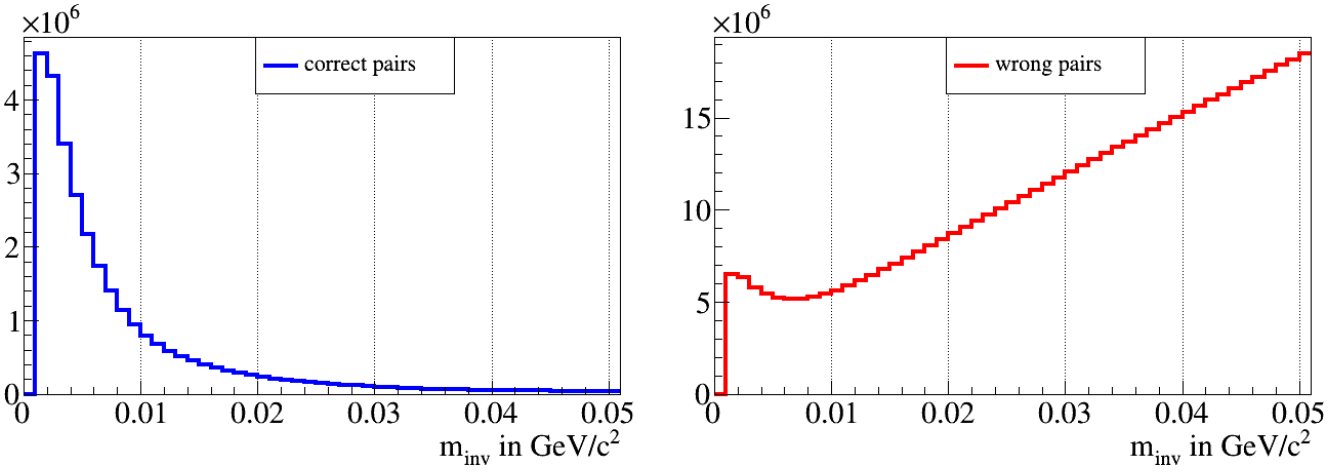

Figure 5.6: Invariant mass distributions of two combined particles for correctly combined (left, blue) and wrongly combined (right, red) pairs of tracks.

Photon reconstruction with Artificial Neural Network

Artificial Neural Networks (ANN) [64] can be used as an alternative approach for photon reconstruction. ANN are layered networks of artificial neurons (AN) which are models of the biological neurons. Artificial Neural Networks are highly effective where traditional analysis would be difficult or impossible to perform. Here, ANN is used to select correctly reconstructed photons from all possible photon candidates.

There are many different ANN configurations which use different techniques. The ring finder algorithm implemented in CbmRoot framework, for example, uses the "Multilayer perceptron" method [65] of ANN in order to judge the quality of found rings. The algorithm has shown good performance results working with reconstructed rings, therefore the same method is used for the analysis presented here.

The structure of Multilayer perceptron consists of one input layer, one hidden layer, and one output layer of ANs connected consistently. The first layer takes input information from dataset and transforms it using a learned non-linear transformation. It passes an input value through to the hidden layer. Hidden layers allow to solve complicated problems adding additional connections between neurons. The final layer provides as an output a numerical probability, that a given event is caused by signal or background. Usual outcome of output is a value between -1 and $+1$. Here, -1 represents a large probability to have a false pair and $+1$ corresponds to the large probability to have a correctly reconstructed converted photon.

In order to make a selection, the following parameters are chosen as input values to the ANN :

- e^+e^- opening angle for the reconstructed photon (Θ),
- e^+e^- invariant mass of the reconstructed photon (m_{inv}),
- three momentum component of combined charged particles ((p_{x1}, p_{y1}, p_{z1}) and (p_{x2}, p_{y2}, p_{z2})),
- reconstructed z-coordinate of conversion point (in beam direction).

The analysis presented here is based on the training sample of 3000 correctly and 3000 falsely reconstructed pairs of tracks with 300 epochs. Applying the received weight parameters onto reconstructed data one can define the necessary cut value using cross check with MCtrue information. The ANN output distributions for false and correct pairs are shown in Figure 5.7.

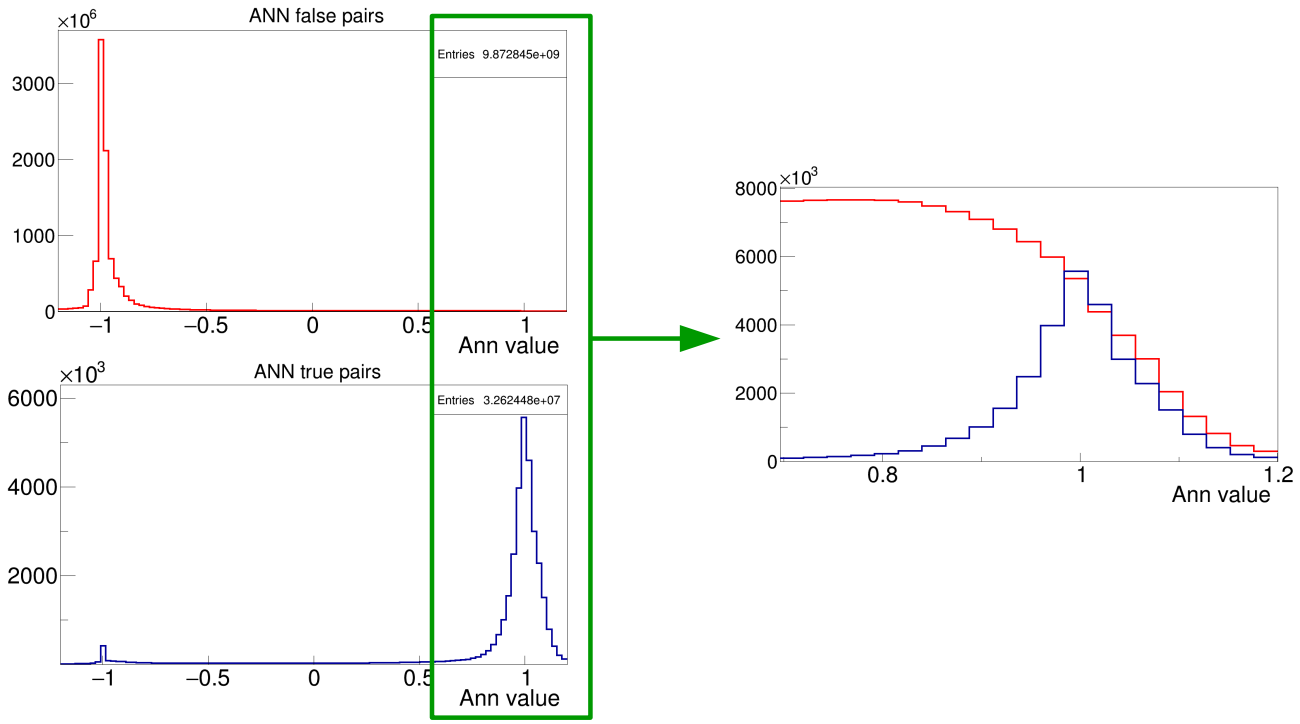

Figure 5.7: ANN output distributions for falsely (red) and correctly (blue) reconstructed pairs. The right picture shows zoomed region between 0.7 and 1.2 of ANN value for both distributions together.

One can see two peaks on graphs: with mean value -1 for false pairs and with mean value $+1$ for correct pairs. For the better representation of results, two ANN distributions are shown together on the right side of Figure 5.7. One can see some amount of background around $+1$ region, which is not visible on the left picture due to the huge peak at -1 region. From these graphs the optimum cut value for the ANN > 0.9 is chosen in order to have as much correct pairs as possible with a minimum amount of background.

Using ANN cut > 0.9, about $\sim$ 83 % of all correct pairs will be reconstructed, and signal to background ratio will be $\sim$ 60 %. In comparison to standard cuts presented above, ANN cut rejects more wrong pairs keeping same amount of correctly reconstructed pairs.

Lepton identification requirements

The standard reconstruction procedure is based on full identification of daughter particles, i.e. all four leptons from double photon conversion have to be identified within the RICH detector. This requirement strongly limits the reconstruction efficiency of π^0/η because it occurs rarely that all four leptons will be reconstructed within the RICH, due to their low momenta. In most of cases at least one out of two leptons from a converted photon is bended out of the RICH acceptance by magnetic field. Weakening the requirements of full identification of both particles in the RICH detector will significantly increase the efficiency reconstruction of neutral mesons. In this analysis, three different cases will be considered (see Table 5.2).

The first case ("two") is reconstruction with full lepton identification within the RICH detector. It consists of those photons, which have electron and positron identified in the RICH detector as leptons, i.e. have been matched to rings. Quantitatively, it is only 10 % of converted photons.

The second case ("onetwo") is reconstruction with partial lepton identification within the

"two"	"onetwo"	"all"
$\pi^0/\eta \rightarrow (e^{\pm} + e^{\mp}) + (e^{\pm} + e^{\mp})$	$\pi^0/\eta \rightarrow (e^{\pm} + e^{\mp}) + (e^{\pm} + e^{\mp})$	$\pi^0/\eta \rightarrow (e^{\pm} + e^{\mp}) + (e^{\pm} + e^{\mp})$
	$\pi^0/\eta \rightarrow (e^{\pm} + e^{\mp}) + (e^{\pm} + ?^{\mp})$	$\pi^0/\eta \rightarrow (e^{\pm} + e^{\mp}) + (e^{\pm} + ?^{\mp})$
	$\pi^0/\eta \rightarrow (e^{\pm} + ?^{\mp}) + (e^{\pm} + ?^{\mp})$	$\pi^0/\eta \rightarrow (e^{\pm} + ?^{\mp}) + (e^{\pm} + ?^{\mp})$
		$\pi^0/\eta \rightarrow (e^{\pm} + e^{\mp}) + (?^{\pm} + ?^{\mp})$
		$\pi^0/\eta \rightarrow (e^{\pm} + ?^{\mp}) + (?^{\pm} + ?^{\mp})$
		$\pi^0/\eta \rightarrow (?^{\pm} + ?^{\mp}) + (?^{\pm} + ?^{\mp})$
(10 %)	(55 %)	(100 %)

Table 5.2: Representation of possible combinations for three approaches using different lepton identification requirements. With green color are shown particles identified within the RICH detector as leptons. With red color are shown particles, which have STS track and fly outside the RICH acceptance. Black brackets indicate pair of particles combined for photon reconstruction.

RICH detector. It consists of those photons, which have at least one electron or positron from the converted pair identified in the RICH detector as a lepton. The second particle can be bended out of the RICH acceptance, but have to be reconstructed within the STS detector. This case also includes photons with full particles reconstruction from the case "two". This type of identification allows to reconstruct around 55 % of converted photons.

The third case ("all") is reconstruction without lepton identification within the RICH detector. This case does not require rings in the RICH detector. The case includes photons, whose products are completely bended out of RICH acceptance, but reconstructed in the STS, in addition to photons from case "onetwo", which are also present here (i.e. reconstruct 100 % of converted photons). This case will have the biggest efficiency reconstruction of π^0 and η, but also will have the biggest background contribution.

Opening angle cut between two reconstructed photons

All photon candidates which satisfy the cuts described above can be combined together in pairs to form π^0/η candidates. A big fraction of such combinations consists of false combinations of photon candidates and only small fraction corresponds to correct pairs stemming from $\pi^0/\eta \rightarrow \gamma + \gamma$ decays. In order to reduce the combinatorial background, an opening angle cut between two reconstructed photons is considered as an additional tool. The different value for opening angle between photons for π^0 and η is expected due to their difference in invariant mass.

In order to derive the optimal value for the opening angle between two photons the reconstructed data together with MCtrue information is used. After combining all reconstructed photons into pairs, all these pairs are sorted into three subgroups: both photons are reconstructed correctly and stem from the same π^0, both photons are reconstructed correctly and stem from the same η, and all other pairs. Opening angle distributions for these three subgroups can be seen in Figure 5.8.

Comparing these three graphs, following cut values are considered as optimal to keep most of signal:

- for π^0 analysis: $\Theta_{\gamma\gamma} < 30°$
- for η analysis: $10° < \Theta_{\gamma\gamma} < 40°$

Follow-up tests have shown, that using the additional cut between photons $\Theta_{\gamma\gamma} < 30°$ for π^0 analysis reduces background around pion peak without significant improvement under the peak region. Therefore, the following cut is not used in further analysis for π^0 reconstruction.

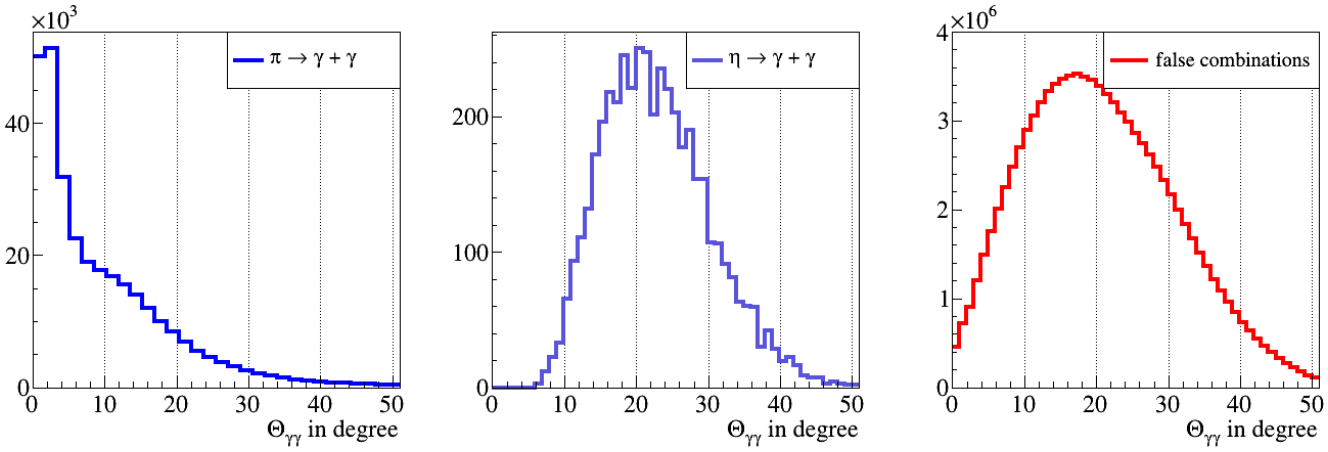

Figure 5.8: Opening angle distributions between reconstructed photons corresponding to combinations of two correctly reconstructed photons stemming from the same π^0 (left), two correctly reconstructed photons stemming from the same η (middle), and two photon candidates which do not stem from same π^0 or η mesons (right).

Similar tests have shown, that the additional cut between photons $10^\circ < \Theta_{\gamma\gamma} < 40^\circ$ for η analysis reduces background in the η peak region for additional $\sim$ 17 %. Therefore, this cut is relevant for η reconstruction via double conversion method and will be applied in analysis.

5.6 Reference to previous works

The conversion analysis studies for the CBM experiment presented in this thesis, are based on forehand studies on π^0 reconstruction with CBM in [66, 67]. However, the analysis concept here is extended significantly going into more details for π^0 reconstruction via conversion method. In particular the presented analysis includes the secondary vertex reconstruction, which helps to reconstruct conversion in the detector material. This extension results in a gain of about factor of 4 for pion reconstruction via double conversion method. Another important new aspect within this study is the extension of lepton identification concepts towards partial identification of the leptons in order to enhance reconstruction statistics.

The two extensions mentioned above are also applied in this thesis in η conversion analysis. The analysis procedure allow to reconstruct η meson via double conversion method, which previously was not feasible. Results for those analyses are presented in next chapters.

6

Results on neutral pion reconstruction

This chapter is dedicated to the estimation of the number of reconstructable π^0 using the conversion method. Cut values estimated with help of MCtrue data in the previous chapter are applied here to achieve optimal π^0 reconstruction. The full reconstruction procedure here is being used in the same way as it would be used in the real experiment. First, the reconstructed charged particles are combined to pairs forming photon candidates, using subtleties described in previous chapter. Later, the π^0 invariant mass spectrum is formed combining two such reconstructed photons in pairs. The reconstructed π^0 invariant mass spectrum also consists of background, shadowing the signal of interest. This background is being simulated using Event Mixing technique and later on is subtracted, leaving only the π^0 signal.

This chapter shows all reconstruction steps leading to the estimation of the π^0 number using the conversion method. Here are shown the limitations of the RICH detector and possible solutions to enlarge the phase-space coverage. Several sets of cuts are being compared in order to find the optimal analysis procedure. All obtained results from π^0 reconstruction analysis are summarized in the last section.

6.1 Reconstruction procedure to get π^0 invariant mass spectrum

The measurement of dielectron and direct photon spectra requires precise knowledge on the contribution from decays (mainly π^0). In order to increase the electron acceptance for low momentum the magnetic field is reduced to 70 % of its nominal value (corresponding to 0.7 Tm). The results shown in this chapter are based on 15×10^6 simulated UrQMD events of central Au+Au collisions at beam energy of 8 AGeV.

By applying the cut values, as described in the previous chapter, it is possible to reconstruct neutral pions from simulated data. The same reconstruction procedures will be later also applied on experimental data in a similar way. The reconstruction chain consists of several steps:

1. Select all particles from GlobalTrack array. At the same time, the RICH detector is used for charged pion suppression: all tracks which reach the detector and do not produce a Cherenkov ring are excluded from further analysis, assuming they are pions.

2. All tracks from the previous step are separated into two subgroups: particles identified as e^-/e^+ in the RICH detector, and particles outside RICH acceptance. All particles with RICH identification must have reconstructed ring properties (A and B parameters from elliptic hit fitter) and reconstructed particle momentum in the range of cuts.

3. All selected tracks are separated into primary and secondary tracks based on their χ^2 of the momentum track fit to the interaction point.

4. All primary tracks are fitted to the interaction point and corresponding momenta are being assigned to tracks. They are further combined into photon candidates using one positive and one negative primary track. Those candidates must satisfy predefined cuts on the opening angle and on the invariant mass of the pair, as well as lepton identification requirements.

5. All secondary tracks are combined into photon candidates using one positive and one negative secondary track. With the help of KFParticle secondary vertex finder the point of closest approach for each such pair is found. After the fit of both tracks to this point the extracted momenta are assigned to corresponding tracks. Those candidates must satisfy predefined cuts on the opening angle and on the invariant mass of the pair, as well as lepton identification requirements.

6. These photon candidates from primary and secondary tracks consist of true and false photons. The true photons are combinations of e^+ and e^- stemming from the same photon. The false photons are combinations of e^+ and e^- stemming from two different photons or combinations of other charged particles. A separation between true and false photons on event-by-event basis is not possible.

7. If at least two photons are reconstructed within one event (regardless of position of conversion), then all possible pair combinations of these photons are formed without any further cuts and the invariant mass of π^0 candidates is calculated.

Figure 6.1 shows the resulting spectra of π^0 candidates (black line) reconstructed using the double conversion method with following steps described above. The reconstruction of π^0 candidates is performed using the three different lepton identification cases. In Figure 6.1 for all identification cases one can clearly see by eye the π^0 peak above the background, but the reconstructed π^0 yield can be determined only after subtraction of the combinatorial background.

Considering all possible photon-photon combinations one gets large combinatorial background in addition to the π^0 signal. This background increases quadratically with the multiplicity of photon candidates N. The number of possible pair combinations is determined by:

$$N_{pair} = \frac{N \times (N-1)}{2} \tag{6.1}$$

The combinatorial background heavily depends on the applied cuts and lepton identification requirements. Therefore, for each π^0 invariant mass spectrum in the analysis its own background description is required based on identical selection criteria.

6.2 Modeling of combinatorial background using Mixed Events

The combinatorial background due to falsely combined photon pairs can be described in several ways. The trivial one is to fit the corresponding background with some polynomial function. This

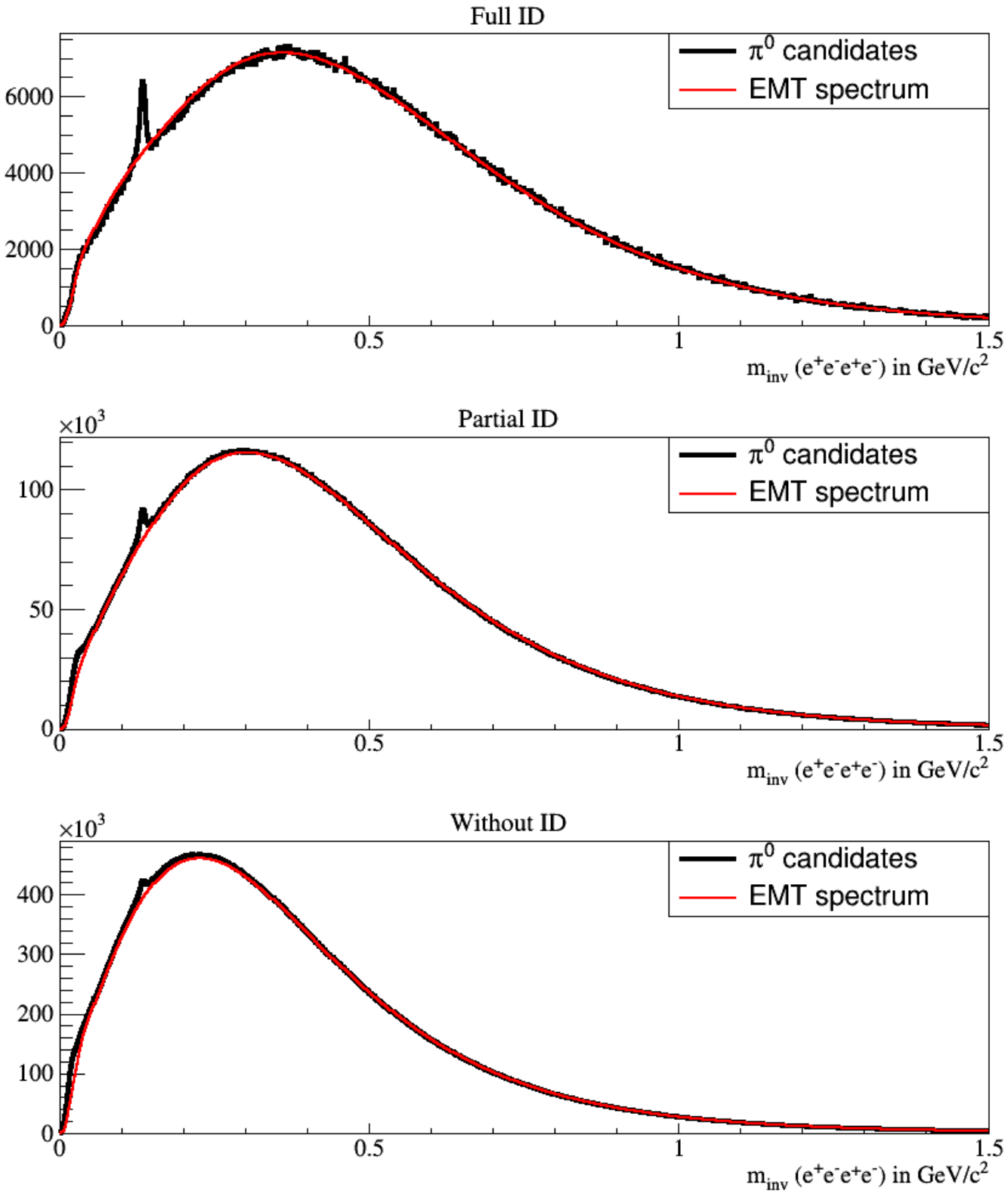

Figure 6.1: Resulting spectra of π^0 candidates reconstructed using double conversion method with cuts on invariant mass of photons $m_{inv}(e^+e^-) < 20$ MeV/c^2 and opening angle of photons $\Theta_{e^+e^-} < 2°$ using different lepton identification approaches: full (upper), partial (middle), without (bottom).

method will describe any kind of background, but on the other hand is usually not a very accurate approach. Therefore, the alternative approach is more preferable and will be used here.

A standard tool for background estimation in particle physics is the simulation of background using Event Mixing Technique (EMT) [68]. Event mixing can be done by combining particles from different events, which are by definition uncorrelated. The mixing technique based on particles from different events is well suited as background simulation tool for events with low (in case of full lepton ID) and also for events with high multiplicity (in case without particle ID) of particles per event. Therefore, the EMT is used here to describe the combinatorial background.

The EMT spectrum in this work is based on combinations of pairs of photons stemming from two different events. Since they are from different events, their invariant mass spectrum will resemble the shape of the combinatorial background without physical signal. In order to keep statistical variation of the simulated background distribution small, a large amount of background must be simulated. In order to match the combinatorial background as close as possible, the exact set of cuts, as were used for the signal reconstruction, have to be used in EMT.

The generation of EMT spectrum is performed in the following way:

- Save all reconstructed photons from the standard reconstruction (which were used to form the invariant mass spectrum of π^0 candidates) together with the corresponding event number in a dedicated array spanning over the last 1000 events.
- Build all possible two photon combinations from saved photons with a restriction that both are stemming from different events. After analyzing first 1000 events, clean the buffer with photons and save another 1000 events.
- The resulting background spectrum is then scaled to the reconstructed spectrum in the range between 0.2 GeV/c^2 and 1.0 GeV/c^2, where no signal peak structure is seen in the distribution.

The scaled background (red line) together with reconstructed spectrum (black line) can be seen in Figure 6.1.

Such scaled EMT invariant mass spectrum can be subtracted from corresponding reconstructed spectrum, leaving only signal entries forming a peak in the region of π^0 mass ($m_{inv}(\pi^0) = 134.97$ MeV/c^2). In addition to the subtracted spectrum, corresponding errors are calculated using normal error propagation:

$$\textit{subtracted} = \textit{(reconstructed) - (normalized EMT)}, \tag{6.2}$$

$$\Delta\textit{subtracted} = \sqrt{(\Delta\textit{reconstructed})^2 + (\Delta\textit{normalized EMT})^2}, \tag{6.3}$$

The remaining peak can be fitted with Gaussian function:

$$f(x) = H \times \exp(-\frac{(x-\mu)^2}{2\sigma^2}) + H_0 \tag{6.4}$$

where H_0 is fit offset, which is needed for situations when the EMT underestimate or overestimate the background under the peak region.

The number of entries (signal) under the peak as well as the signal to background ratio can then be estimated. The amount of reconstructed π^0 within the peak in the background-subtracted spectrum is calculated by adding corresponding bins in the region $m_{inv}(\pi^0)\pm3\sigma$ and by subtracting the offset from the fit. The peak position $m_{inv}(\pi^0)$ and width of the peak σ are taken from the

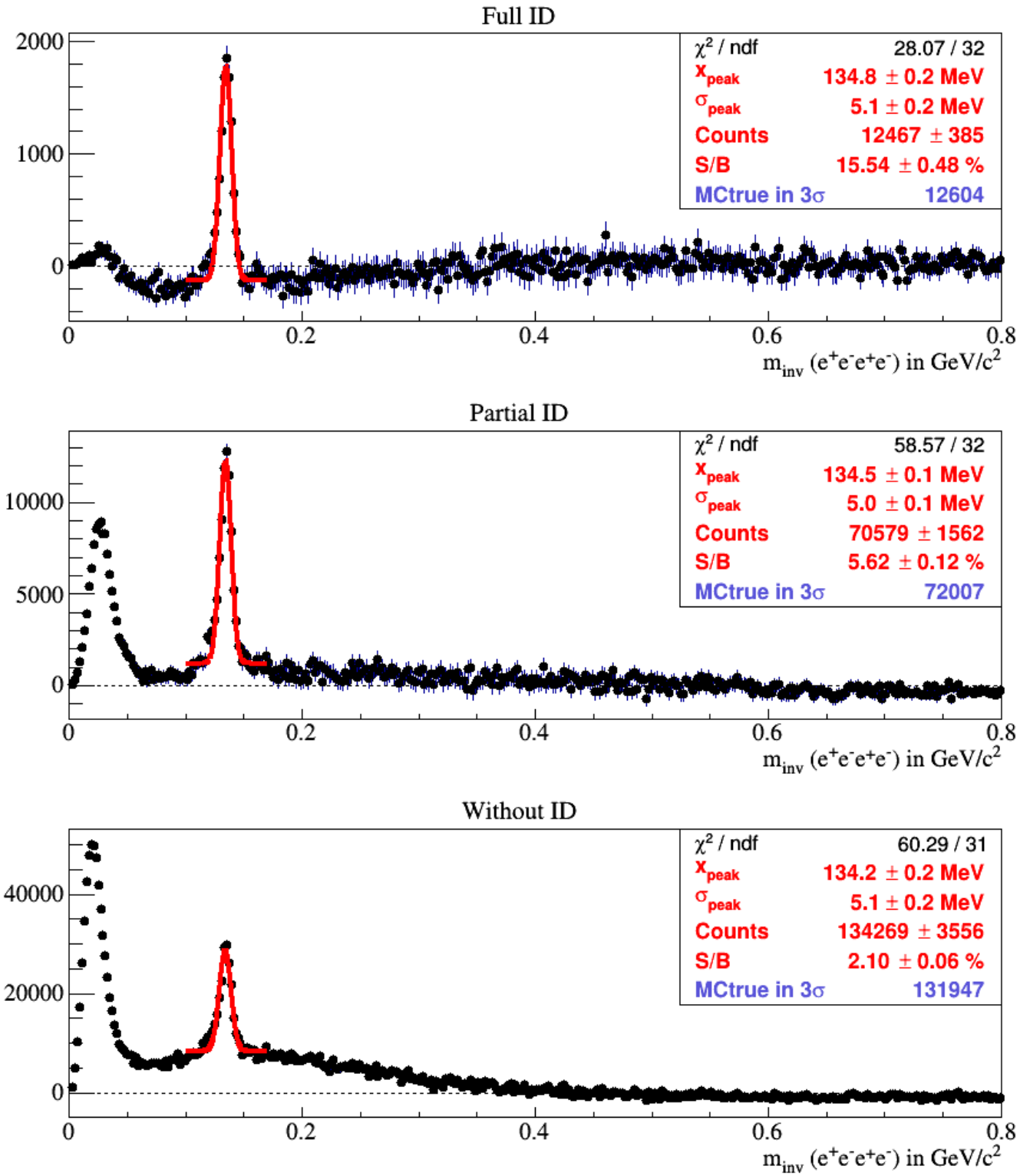

Figure 6.2: Two photon invariant mass spectra after background subtraction from the analysis with cuts $m_{inv}(e^+e^-) < 20$ MeV/c^2 and $\Theta_{e^+e^-} < 2°$ using different lepton identification approaches: full (upper), partial (middle), without (bottom). Black dots show the background-subtracted spectrum and in red is shown the result of Gaussian fit to the peak region.

corresponding fit. For calculation of signal and background amount the same 3σ-region is taken from the reconstructed resulting spectrum of π^0. The signal to background ratio can be calculated by dividing both these received numbers by each other. The corresponding formulas can be found below:

$$signal = \sum_{m_{\pi^0}-3\sigma}^{m_{\pi^0}+3\sigma} (bckg\text{-}subtracted\ spectrum - fit\ offset)$$

$$signal{+}background = \sum_{m_{\pi^0}-3\sigma}^{m_{\pi^0}+3\sigma} (reconstructed\ spectrum)$$

$$\frac{S}{B} = \frac{signal}{signal + background} \times 100\ [\%] \tag{6.5}$$

The extracted π^0 peaks using three particle identification approaches together with their fits can be seen in Figure 6.2. In the legend of Figure 6.2 with red letters are shown reconstructed values: peak position, width of the peak, the number of entries under the peak, and signal to background ratio. With blue letters in the legend of Figure 6.2 is shown the real number of π^0 in reconstructed spectrum, obtained from MCtrue data.

The three types of analysis give almost the same π^0 peak position, which is slightly smaller than the theoretical value. Such small difference (< 1 MeV/c^2) is an attribute of insignificant energy loss of particles due to bremsstrahlung effect. The width of the pion peak is in a good agreement for all three approaches and equals to $\sigma \approx 5$ MeV/c^2, which indicates a very good reconstruction quality.

The main difference between the three approaches is seen in the number of reconstructed pions and in signal to background ratio (see legends in Figure 6.2). There is a significant increase of number of reconstructed pions, when one requests weaker lepton identification requirements in the RICH detector. The gain in π^0 reconstruction efficiency using partial and without identification approaches is correspondingly about a factor of 6 and 10 in comparison to the full identification approach. On the other hand, the loss in signal to background ratio is about factor of 3 and 7 correspondingly also in comparison to the full identification approach.

The reconstruction efficiency for weaker lepton identification requirements increases due to low momentum leptons from conversion, which do not reach the RICH detector, but cause a signal in STS. This weaker requirements at the same time give additional wrong pair combinations. In most of such additional wrong pairs, one particle is a charged pion, which has flight direction outside the RICH acceptance and, therefore is treated as a low momentum lepton.

6.3 Description of correlated background

Looking at background-subtracted spectra in Figure 6.2, one can see a pronounced peak at low invariant mass region (around 30 MeV/c^2) for partial identification approach as well as for the approach without lepton identification. For the case without identification such extra peak is even more pronounced than the reconstructed π^0 peak. The same peak is only barely visible using the analysis with full lepton identification. This peak originates from the fact, that the event mixing technique does not describe all background contributions in the reconstructed spectrum. The event mixing technique per definition describes only combinatorial background stemming from uncorrelated photons. The additional invariant mass peak at ~ 30 MeV/c^2 shows, that additional background of somehow correlated photon candidates is still contained in the event sample after applying all selection criteria.

For the case without identification one can also notice in Figure 6.2 some additional background forming a "hill" under the π^0 peak region. The origin of such surplus must also come from some correlated photon candidates satisfying the selection criteria of this approach.

In oder to understand the nature of these correlated background events, the selected events were divided into different subsamples based on MCtrue data:

1. Correctly reconstructed π^0 from two photon decay channel, or from Dalitz decay channel. Both e^+e^--pairs are correctly matched together to form converted photons, and these photons are further combined forming a correct π^0 signal.

2. Final particle consists of 4 leptons. Both e^+e^- pairs are correctly matched together to form converted photons, but both photons stem from different sources.

3. Final particle consists of 4 leptons. One photon is correctly reconstructed and second one wrongly. Three leptons out of four reconstructed ones have the same grandmother particle.

4. Final particle consists of 4 leptons. One photon is correctly reconstructed and second one wrongly. Only two leptons have the same grandmother particle.

5. Final particle consists of 4 leptons. Both gammas are wrongly combined. Leptons may have any grandmother particles.

6. One particle out of four is not a lepton.

7. Two particles out of four are not leptons.

8. Three particles out of four are not leptons.

9. All four particles are not leptons.

All contributions for each of three lepton identification approaches can be seen in Figure 6.3 with a sequence in the legend corresponding to the sequence above.

For analysis with partial identification one can see in Figure 6.3 some background coming from contributions number 8) and 9), which are not expected in this approach. They occur because of mismatches in the RICH detector, when rings are wrongly assigned to non lepton tracks. These contributions are relatively small in comparison to other subgroups.

As can be seen in the Figure 6.3, in the approach with partial lepton identification the peak at low invariant mass comes mostly from background contributions number 5) and 6). For approach without lepton identification, in addition to 5) and 6), also subgroup number 9) causes some contribution to the peak at low invariant mass region. For both approaches subgroup number 3) produces a correlated background forming the "hill" under the pion peak.

Digging a little bit deeper and separating the contributions number 3), 5), 6) into several additional subgroups, one can determine three main combinations, which contribute to the peak:

- Three leptons out of four particles stem from same π^0. Fourth particle is either a lepton or a pion coming from somewhere else (for example $\gamma_1 \to e_1^+ + e_1^-$ and $\gamma_2 \to e_2^+ + e_3^-/\pi_3^-$).

- Two photons combined from four leptons. Every photon has one lepton from given converted photon and second lepton comes from some other source (for example $\gamma_1 \to e_1^+ + e_3^-$ and $\gamma_2 \to e_4^+ + e_1^-$).

- Both photons reconstructed out of one lepton and one pion. These leptons come from one given converted photon and pions come from fireball (for example $\gamma_1 \to e_1^+ + \pi^-$ and $\gamma_2 \to \pi^+ + e_1^-$).

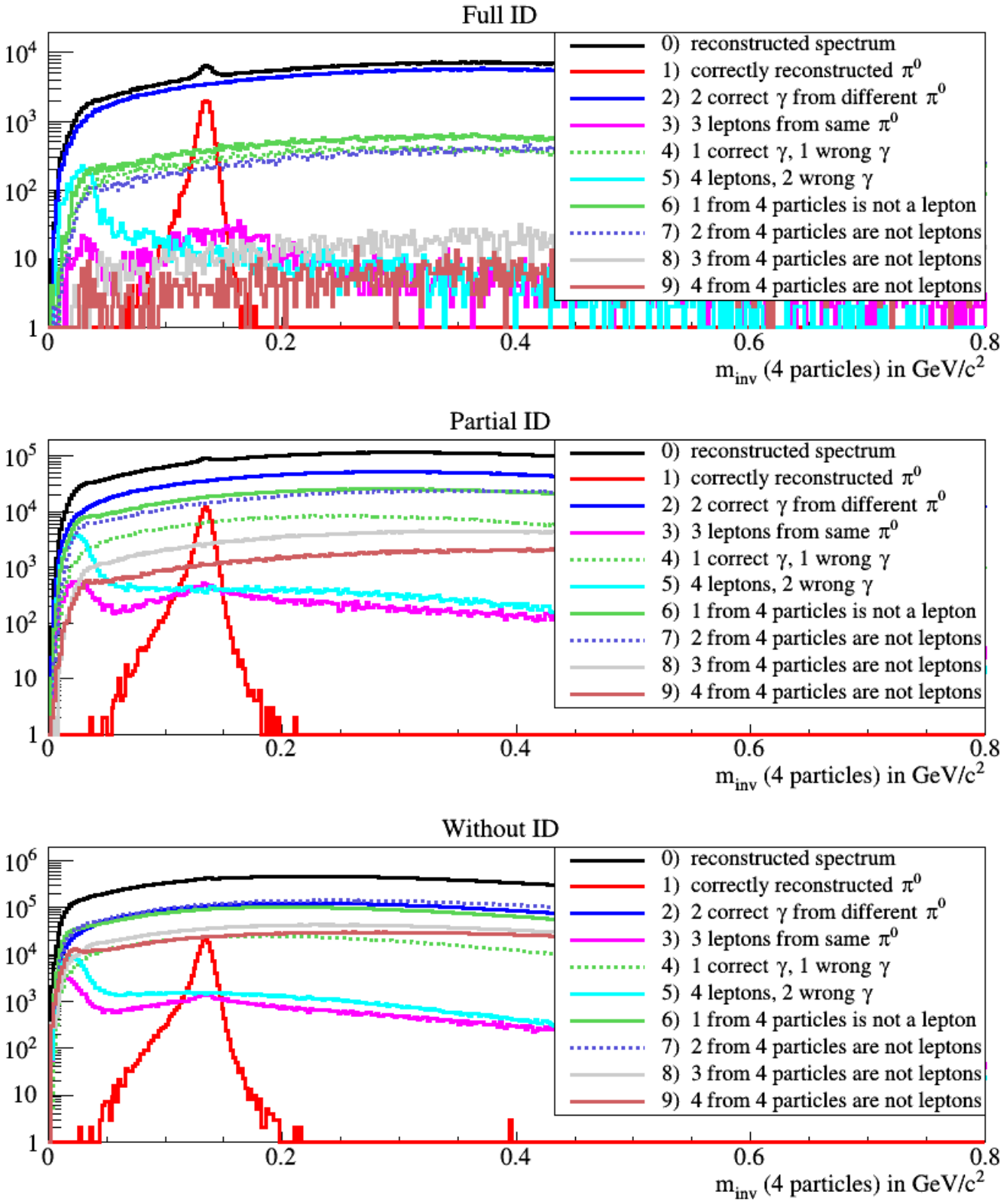

Figure 6.3: Decomposition of various different contributions to the π^0 invariant mass spectrum from the analysis with cuts $m_{inv}(e^+e^-) < 20$ MeV/c^2 and $\Theta_{e^+e^-} < 2°$ using different lepton identification approaches: full (upper), partial (middle), without (bottom).

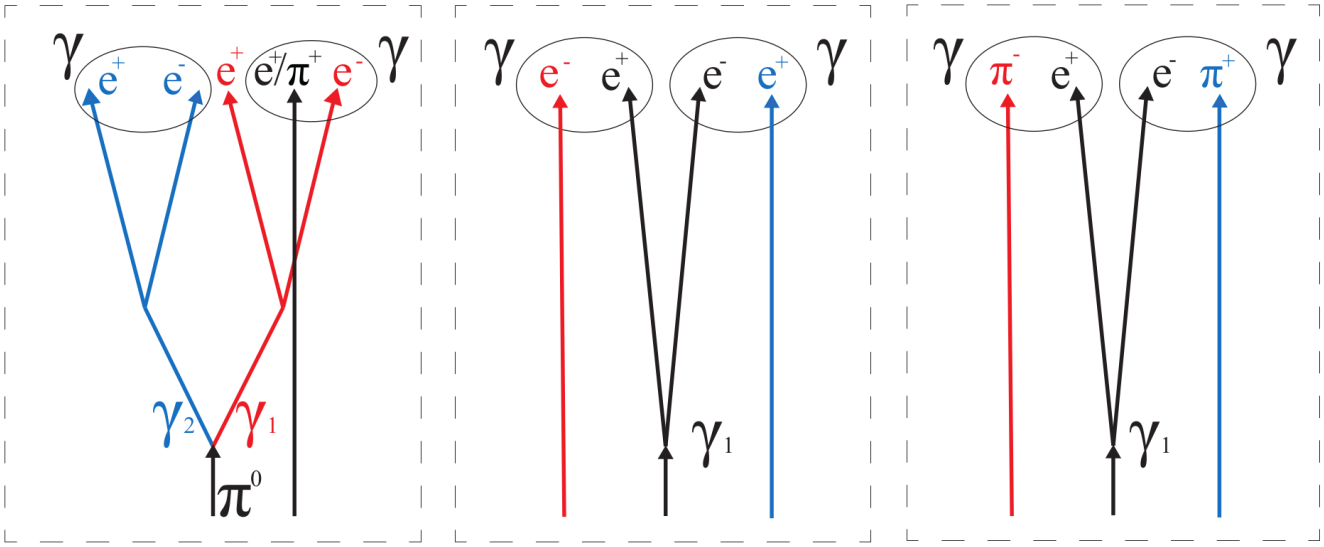

Figure 6.4: Different background contributions into low invariant mass peak for the analysis with partial lepton identification in the RICH detector.

The upper three additional subgroups are illustrated in Figure 6.4. They can not be simulated with event mixing technique since such two reconstructed photons are correlated (leptons from converted real photon), which can not be reproduced by mixing photons from different events. Furthermore, it was identified that such peak occurs only for the reconstruction when both such photons have their presumably conversion points in the target. This is intuitive since from the target point hundreds of charged particles are emitted, and the probability to form such correlated background in this case is much bigger than for particle pairs from outside the target. Several approaches have been tested, but neither of them is able to take away the peak at low invariant mass region. It is also noticeable that this peak is well separated from the signal peak and has no influence on it.

6.4 π^0 acceptance and reconstruction efficiency

The reconstructed number of π^0 in Figure 6.2 for each of the three approaches is around $10^4 - 10^5$ depending on the approach. This number is relatively small in comparison to the number of all produced π^0 in the simulated sample $= 2.2 * 10^9$. The low efficiency in reconstruction of π^0 via double conversion is partially explained by the low conversion probability. The expected conversion probability for photons in the gold target with a thickness of 250 μm is about 2.9 % [69]. The material budget of MVD and first five STS stations adds another 2.7 % to the conversion probability of photons. This sums up to 0.31 % probability that both decay-photons from one π^0 will be converted in the target or in the detector material before the RICH detector. In addition, the finite acceptance of the detector further limits the reconstruction, resulting in a limited phase space coverage of reconstructed particles. A comparison between simulated and reconstructed π^0 can be seen in Figure 6.5.

Figure 6.5 shows the reconstruction efficiency (right plot) as function of transverse momentum p_t and rapidity y for three analysis approaches, obtained by dividing the corresponding number of correctly reconstructed π^0 (middle plot) by all generated π^0 in the simulated sample (left plot) using MCtrue data.

One can clearly see the difference between plots with generated and reconstructed pions. The

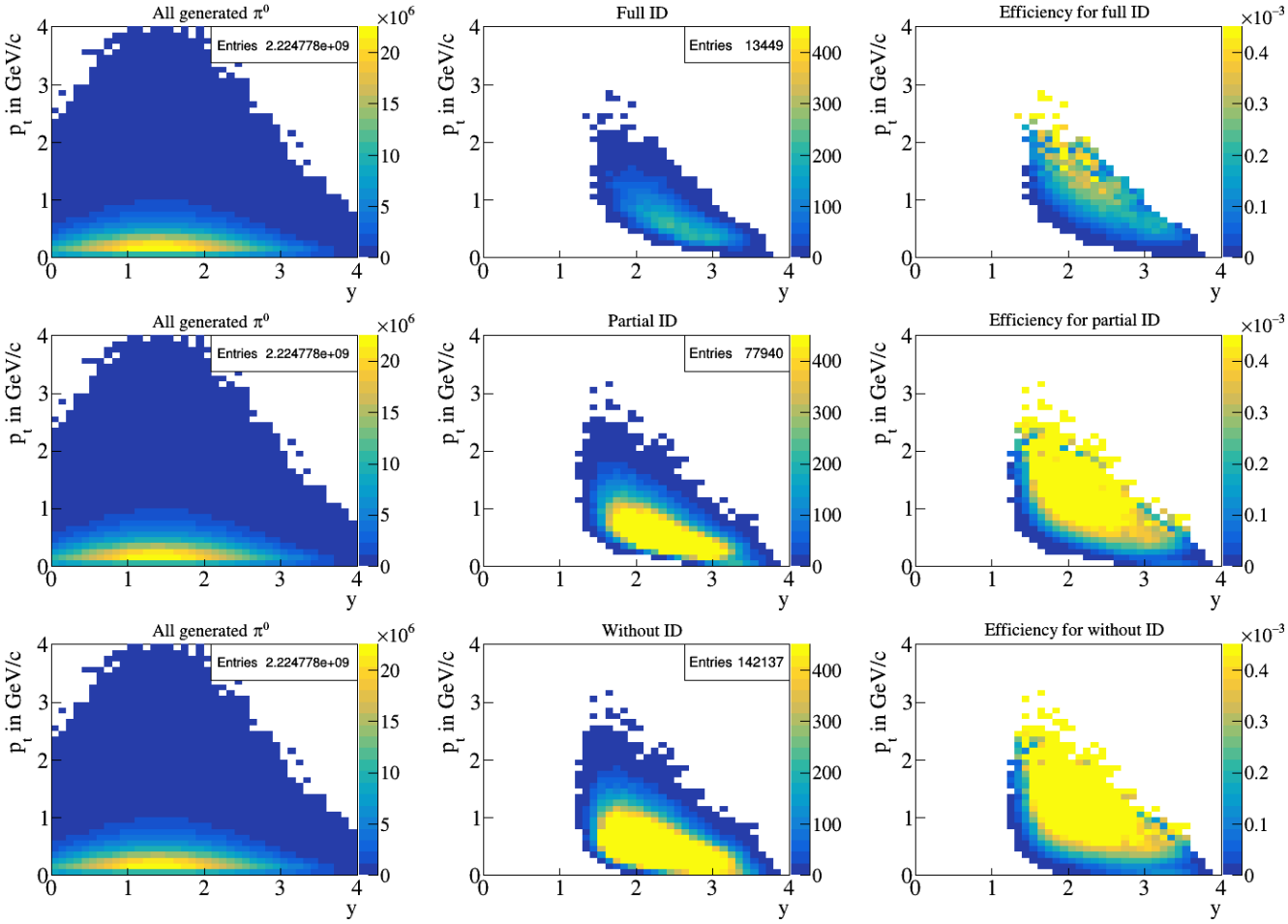

Figure 6.5: Reconstruction efficiency of π^0 as function of transverse momentum p_t and rapidity y for all 3 discussed analysis approaches: full (upper row), partial (middle row), without (bottom row).

Figure 6.5 shows, that the reconstruction procedure has a cut-off towards low rapidities $y < 1.5$. It can be explained by the geometrical acceptance of the CBM detector. Assuming that for low particle masses (including pions) the rapidity y can be approximated by the pseudo-rapidity $\eta = -\ln(\tan\frac{\theta}{2})$, with θ being the emission angle of the particle, the cut-off in rapidity can then be calculated for the maximum geometrical acceptance with $\theta = 25°$ to $y \sim 1.5$, confirming the results from the obtained phase-space coverage. An upper limit in rapidity is expected at $y \sim 3.8$ (with $\theta = 2.5°$) due to the beam pipe, as can be also seen in Figure 6.5. The limitation in rapidity can not be avoided since the geometrical acceptance of the CBM detector is fixed.

Figure 6.5 shows, that there are no reconstructed π^0 in the very low transverse momentum region $p_t < 0.2$ GeV/c for the approach with full lepton identification. The limitation is explained by the magnetic field. Most of low momenta leptons are bended by the magnetic field and, as a result, they can not reach the RICH detector, but only cause a signal in the STS. Such leptons are to some part included in the approach with partial identification and completely included in the approach without lepton identification.

The benefit of approaches with partial and without identification in terms of reconstruction efficiency in comparison to the full identification approach can be seen at the right column in Figure 6.5. The color scale for all pictures in the right column is the same. One can observe that the requirement of partial identification significantly increases the reconstruction efficiency

for π^0 in the region of $p_t > 0.5$ GeV/c as well as slightly extends the phase space coverage of reconstructed π^0 towards the low momentum region, where most of the produced π^0 are situated. On the other hand, the less strict requirement on particle identification leads to a degradation in signal to background ratio.

On the other hand, the difference between approaches with partial identification and without identification is only a slight extension of phase space coverage of reconstructed π^0 towards $p_t = 0$ GeV/c region. Such slight increase of reconstruction efficiency of π^0 decreases signal to background ratio in about three times, which is not critical, but very undesirable.

An alternative way to keep more low momenta leptons for approach with full identification would be to change the strength of the magnetic field. Since the magnetic field bends all charged particles, the acceptance in low transverse momenta heavily depends on the field strength. The stronger the field, the smaller the acceptance is. Based on this rule the magnetic field can be reduced even further to 50 % or even 30 % of its nominal value in order to cover the region with low transverse momenta. The reducing of magnetic field will save more low momenta particles for the analysis with full identification, but on the other hand will decrease the resolution of reconstructed momenta in STS, which at the same time is very undesirable.

6.5 Variation of cut values used in reconstruction

In order to study the influence of cut variations on results obtained from the conversion analysis, other possible cuts were also tested. More strict cuts will decrease slightly statistics, reconstruction efficiency, and the background, as was described in Section 5.5. More loose cuts will change these parameters in opposite direction. The analysis procedure was repeated in exactly the same way as in previous sections.

In Figure 6.6 one can see the obtained results using 3 different lepton identification approaches with cuts on invariant mass of photons $m_{inv}(e^+e^-) < 10$ MeV/c^2 and opening angle of photons $\Theta_{e^+e^-} < 1^\circ$. All reconstructed spectra have similar shape and their signal peaks are clearly visible above the background. The combinatorial background simulated with event mixing technique describes well the corresponding background. The fit results for background-subtracted spectra can be seen in Table 6.1. In order to directly compare two sets of cuts the results from previous sections are also listed in Table 6.1.

case	m_{π^0}, MeV/c^2	σ, MeV/c^2	counts in 3σ	S/B in %	π^0 from MCtrue in 3σ
set 1:	$m_{inv}(e^+e^-) < 10$ MeV/c^2 and $\Theta_{e^+e^-} < 1^\circ$				
"two"	134.3 ± 0.2	4.6 ± 0.2	7737 ± 274	18.71 ± 0.66	7829
"onetwo"	134.0 ± 0.1	4.6 ± 0.1	41917 ± 905	9.74 ± 0.21	42126
"all"	134.1 ± 0.1	4.5 ± 0.1	68428 ± 1631	5.01 ± 0.12	69048
set 2:	$m_{inv}(e^+e^-) < 20$ MeV/c^2 and $\Theta_{e^+e^-} < 2^\circ$				
"two"	134.8 ± 0.2	5.1 ± 0.2	12467 ± 385	15.54 ± 0.48	12604
"onetwo"	134.5 ± 0.1	5.0 ± 0.1	70579 ± 1562	5.62 ± 0.12	72007
"all"	134.2 ± 0.2	5.1 ± 0.2	134269 ± 3556	2.10 ± 0.06	131947

Table 6.1: Fit results for three analysis approaches using two different sets of cuts during the photon reconstruction.

In Figure 6.6 one can see that using more strict cuts the correlated background, which causes a surplus under the pion peak, has disappeared. One can also notice that the additional peak at low invariant mass region has much smaller amplitude comparing to the analysis with cuts

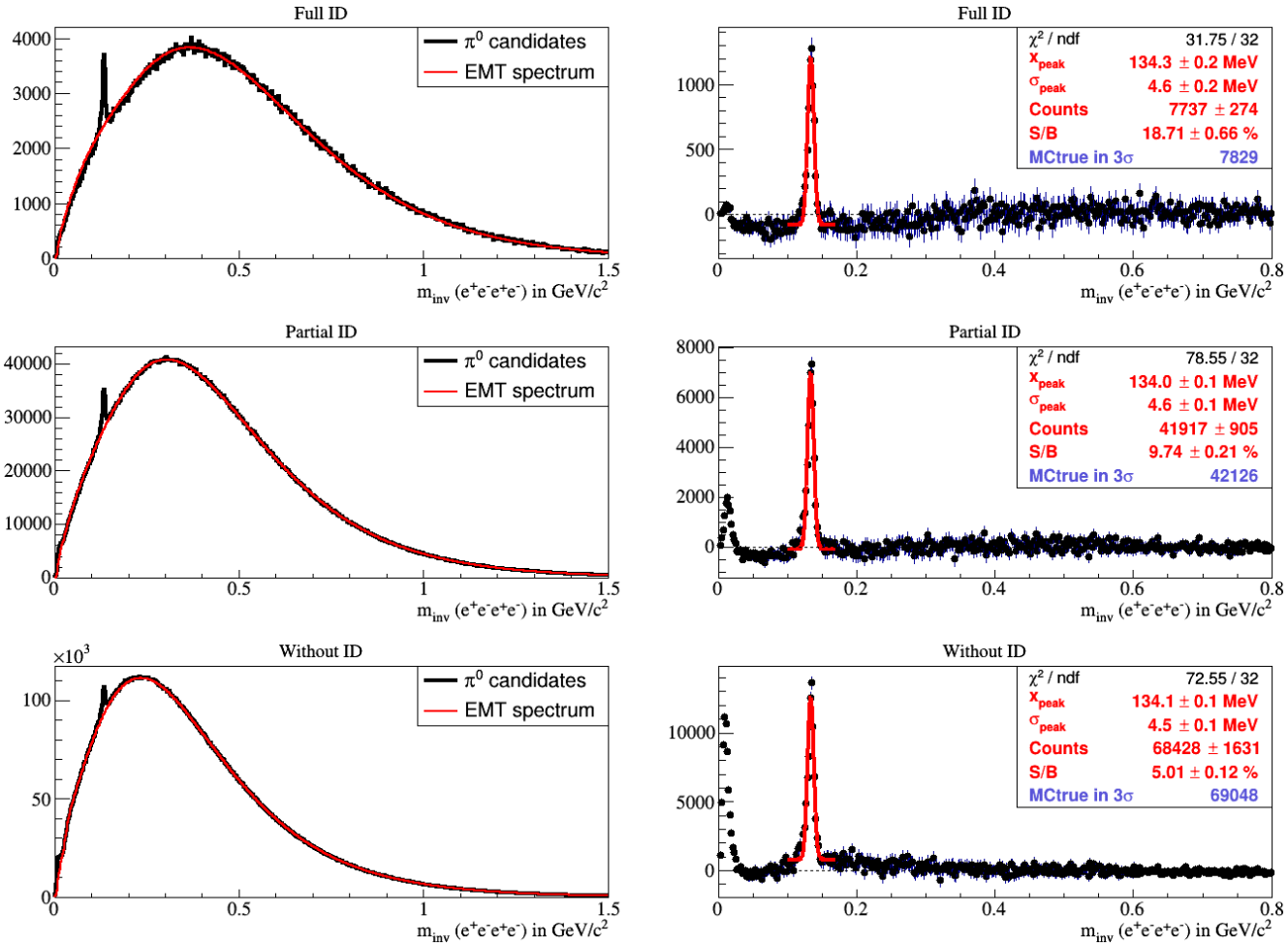

Figure 6.6: Resulting invariant mass spectra of π^0 candidates (left) and background-subtracted spectra (right) reconstructed by applying double conversion method with cuts on invariant mass of photons $m_{inv}(e^+e^-) < 10$ MeV/c^2 and opening angle of photons $\Theta_{e^+e^-} < 1°$ using different identification approaches: full (upper row), partial (middle row), without (bottom row).

$m_{inv}(e^+e^-) < 20$ MeV/c^2 and $\Theta_{e^+e^-} < 2°$ for approaches with partial and without lepton identification. For the analysis with full lepton identification the low invariant mass peak is not visible at all. It means that more strict cuts strongly reduce the probability to combine false pairs, which correlate with each other.

One can see from the Table 6.1 that the pion peak position for both sets of cuts has a reconstructed value slightly smaller than the theoretical one. This is happening mostly due to Bremsstrahlung effect. The more strict cuts give higher pion reconstruction accuracy, which is also reflected in smaller sigma value of the reconstructed peak for all 3 approaches. However, the effect is small and does not change a lot. Applying the more strict set of cuts one decreases the number of reconstructed π^0 by about a factor of 2, but in the same time one increases the signal to background ratio also by about a factor of 2.

The phase space coverage of reconstructed π^0 in terms of transverse momentum p_t and rapidity y with cuts on invariant mass of photons $m_{inv}(e^+e^-) < 10$ MeV/c^2 and opening angle of photons $\Theta_{e^+e^-} < 1°$ looks similar to phase space coverage with second set of cuts, but with less amount of reconstructed π^0, therefore it is not shown here.

Even less strict cuts were also tested, but not presented in details in this thesis. There are two sets of cuts which were considered: 1) $m_{inv}(e^+e^-) < 30$ MeV/c^2 and $\Theta_{e^+e^-} < 3°$; 2) $m_{inv}(e^+e^-) <$

40 MeV/c^2 and $\Theta_{e^+e^-} < 4°$. During these tests some difficulties were observed in the fitting routines because of the huge amount of correlated background, in particular for reconstructed spectra with cuts $m_{inv}(e^+e^-) < 40$ MeV/c^2 and $\Theta_{e^+e^-} < 4°$, leading to a discrepancy between number of reconstructed pions and number of pions in the spectrum. Therefore, cuts $m_{inv}(e^+e^-) <$ 40 MeV/c^2 and $\Theta_{e^+e^-} < 4°$, and even less strict are not recommended to use. A summary of the results of the conversion analysis with different sets of cuts can be found in the last section in Table 6.2.

6.6 Reconstruction using Artificial Neural Network

During the photon reconstruction instead of strict cuts on opening angle and invariant mass of combined pair, one can use alternative approach based on Artificial Neural Network output. The selection criteria on the ANN probability result in this approach is chosen to be > 0.9 in order to keep most of correctly reconstructed photons.

In Figure 6.7 one can see π^0 invariant mass spectra from three types of reconstruction analysis with cut on ANN value for photons > 0.9. All reconstructed spectra are of similar shape and their signal peaks are clearly visible above the background. The background spectra simulated with event mixing technique describe quite well the combinatorial background, but not the correlated background. It results in a "hill" under the pion peak region and in a peak at low invariant mass. Although, the background is not described properly, the pion peak is clearly seen above the rest of background, is well fitted with the Gaussian function, and the extracted number of counts under the peak is close to the MCtrue value.

The results using ANN cut are very similar to the results obtained by using cuts on invariant mass of photons $m_{inv}(e^+e^-) < 20$ MeV/c^2 and opening angle of photons $\Theta_{e^+e^-} < 2°$. Analysis with ANN cut has slightly higher number of reconstructed pions, but at the same time has higher background, which results in smaller signal to background ratio. The phase space coverage of reconstructed π^0 in terms of transverse momentum p_t and rapidity y with cut on ANN value > 0.9 looks exactly the same as with cuts on invariant mass of photons $m_{inv}(e^+e^-) < 20$ MeV/c^2 and opening angle of photons $\Theta_{e^+e^-} < 2°$ and, therefore is not presented in this section.

The results with ANN cut show, that analyses with full identification and partial identification have reconstructed π^0 peak position very close to the theoretical value. At the same time, the peak position from analysis without identification differs by about 1 MeV/c^2 from the theoretical value. Such small deviation of results is not critical.

Overall the ANN based analysis can be used as alternative selection criteria, but strict cuts are more preferable due to the lower amount of correlated background for approaches with partial and without lepton identification. For the approach with full identification ANN selection shows similar good performance as strict cuts.

6.7 Summary

In this chapter different selection cuts for π^0 reconstruction using double conversion analysis were compared, which of course have influence on the reconstruction efficiency and signal to background ratio. However, within the discussed range all of these cuts are justified and it will depend on the later analysis, which of them are more suitable. The final results of the analysis for each of the three approaches using different sets of cuts are summarized in Table 6.2. The graphical representation of this table is shown in Figure 6.8. The correlation between points in Figure 6.8 has roughly exponential dependence (red curvature is a fit of data with an exponential function).

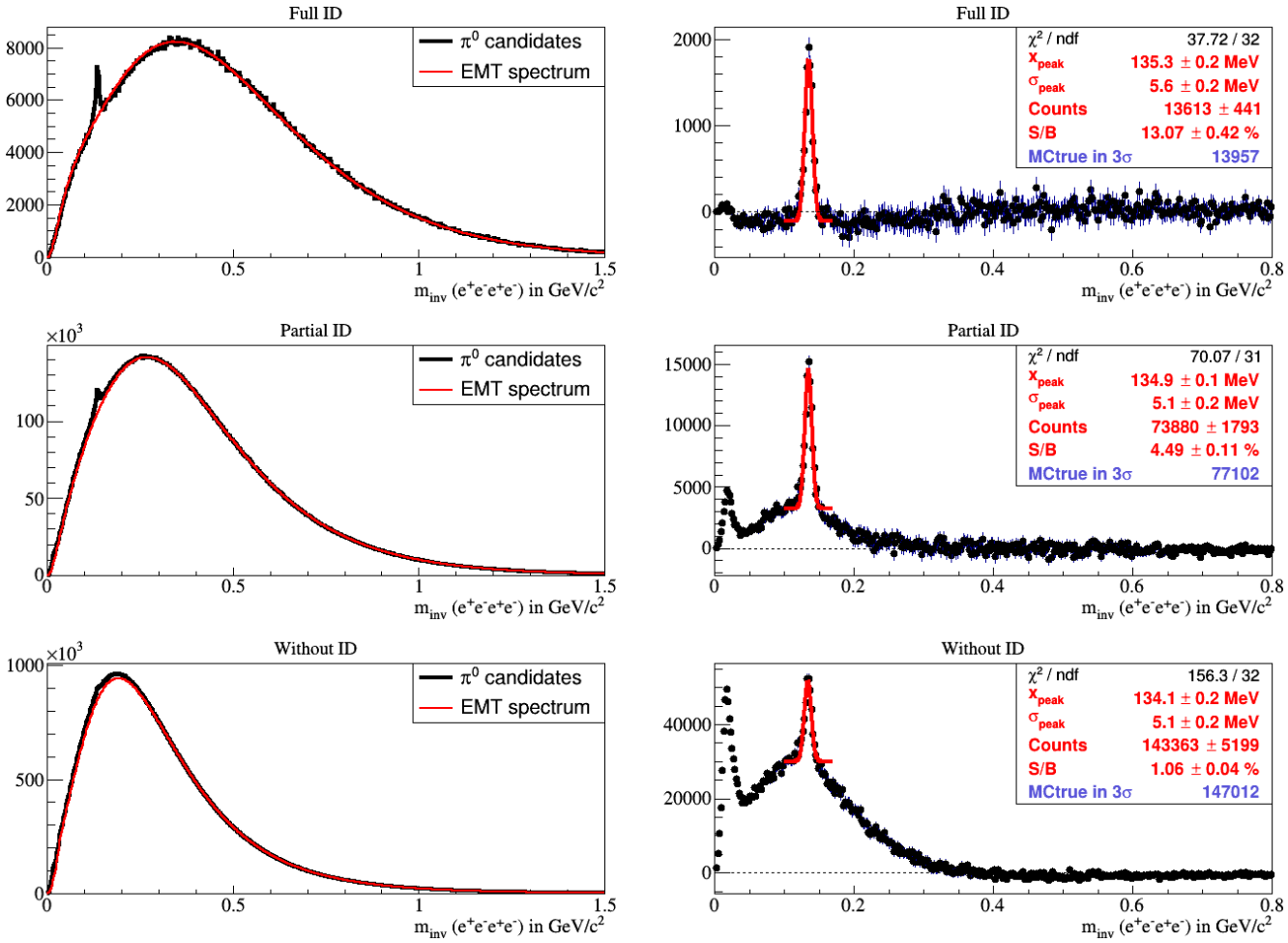

Figure 6.7: Reconstructed invariant mass spectra of π^0 candidates (left) and background-subtracted spectra (right) reconstructed applying double conversion method with cut on ANN value for photons > 0.9 using different identification approaches: full (upper row), partial (middle row), without (bottom row).

The investigation of ANN use was also tested within this work instead of using strict cuts, but, as the analysis shows, there is no clear improvement from the use of the ANN cut. Using the ANN cut one gets many correlated pairs, which can not be described by event mixing technique. The ANN selection shows good performance in the analysis with full lepton identification in the RICH detector. However, the obtained results are similar to the analysis using strict cuts on invariant mass of photons $m_{inv}(e^+e^-) < 20$ MeV/c^2 and opening angle of photons $\Theta_{e^+e^-} < 2°$.

The more loose cuts are used, the more correlated pairs are formed. Therefore, it is not recommended to use very strong cut values on invariant mass and opening angle of photons.

The optimal cut values for photon conversion analysis are: "set 1" and "set 2" (see Table 6.2). There is no clear preference to use first or second set of cuts. Using very strict cut values ("set 1") for photon reconstruction one strongly suppresses correlated background sacrificing reconstruction efficiency. Using more loose cut values ("set 2") one gains in about 2 times more reconstruction efficiency, but in the same time the signal to background decreases in about the same factor of 2. At the end, it is a compromise and depends on what one later needs to do in a physics analysis. Overall, the data sample with 15 million central Au+Au events already allows to count number of reconstructed π^0 with an accuracy of ~ 2 % using these sets of cuts. The use of stronger cut values as "set 3" and "set 4" gives the reconstruction accuracy of $\sim 3-4$ %.

case	m_{π^0}, MeV/c^2	σ, MeV/c^2	counts in 3σ	S/B in %	π^0 from MCtrue in 3σ
set 1:	$m_{inv}(e^+e^-) < 10$ MeV/c^2; $\Theta_{e^+e^-} < 1°$				
"two"	134.3 ± 0.2	4.6 ± 0.2	7737 ± 274	18.71 ± 0.66	7829
"onetwo"	134.0 ± 0.1	4.6 ± 0.1	41917 ± 905	9.74 ± 0.21	42126
"all"	134.1 ± 0.1	4.5 ± 0.1	68428 ± 1631	5.01 ± 0.12	69048
set 2:	$m_{inv}(e^+e^-) < 20$ MeV/c^2; $\Theta_{e^+e^-} < 2°$				
"two"	134.8 ± 0.2	5.1 ± 0.2	12467 ± 385	15.54 ± 0.48	12604
"onetwo"	134.5 ± 0.1	5.0 ± 0.1	70579 ± 1562	5.62 ± 0.12	72007
"all"	134.2 ± 0.2	5.1 ± 0.2	134269 ± 3556	2.10 ± 0.06	131947
set 3:	$m_{inv}(e^+e^-) < 30$ MeV/c^2; $\Theta_{e^+e^-} < 3°$				
"two"	135.0 ± 0.2	5.6 ± 0.2	14794 ± 485	11.83 ± 0.39	14872
"onetwo"	134.7 ± 0.2	5.2 ± 0.2	84289 ± 2240	3.31 ± 0.09	85320
"all"	134.1 ± 0.2	5.4 ± 0.3	167554 ± 5800	0.99 ± 0.03	160943
set 4:	$m_{inv}(e^+e^-) < 40$ MeV/c^2; $\Theta_{e^+e^-} < 4°$				
"two"	134.9 ± 0.2	5.4 ± 0.2	14629 ± 541	9.51 ± 0.35	15560
"onetwo"	134.3 ± 0.2	4.9 ± 0.2	77047 ± 3064	1.63 ± 0.06	91626
"all"	133.5 ± 0.3	5.4 ± 0.4	164056 ± 8651	0.44 ± 0.02	175483
set 5:	ANN value > 0.9				
"two"	135.3 ± 0.2	5.6 ± 0.2	13613 ± 441	13.07 ± 0.42	13957
"onetwo"	134.9 ± 0.1	5.1 ± 0.2	73880 ± 1793	4.49 ± 0.11	77102
"all"	134.1 ± 0.2	5.1 ± 0.2	143363 ± 5199	1.06 ± 0.04	147012

Table 6.2: Summarized results for three different particle identification approaches and five different variations of selection cuts.

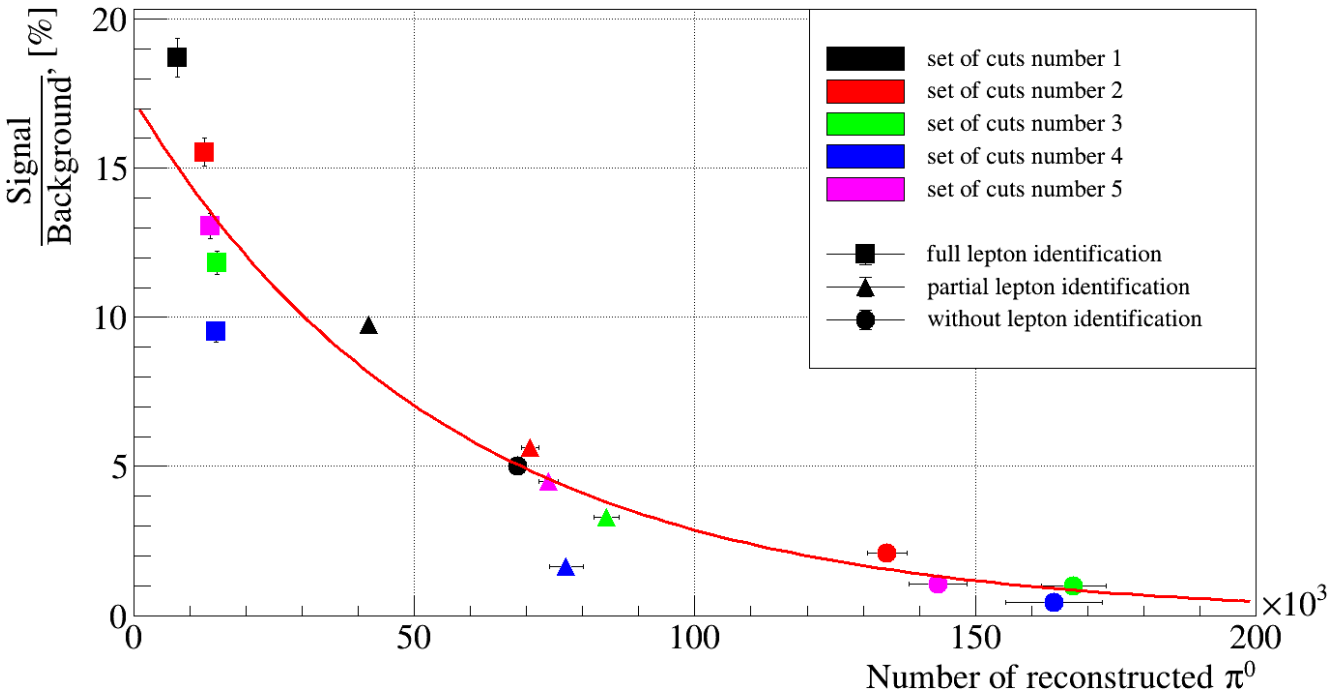

Figure 6.8: Correlation between reconstructed number of π^0 and signal to background ratio. Different colors belong to different sets of cuts. The 3 different approaches on particle ID are shown with squares, triangles, and circles respectively.

In order to have a larger reconstruction efficiency and in particular to increase phase space coverage, one can request instead of full lepton identification only partial lepton identification. This approach increases pion reconstruction efficiency by about factor of 6, but at the same time decreases signal to background ratio by about factor of $2-4$ depending on cut values. If one skips identification completely, the reconstruction efficiency will be improved even further by about factor of 11 in comparison to the full identification approach, but doing this one significantly loses in signal to background ratio.

It is recommended to use either full lepton identification or partial identification approaches, since they give high efficiency reconstruction with rather moderate background. These are then two more realistic options, when the extreme case skipping identification completely has no clear advantages to use it.

7

Reconstruction of the eta meson using conversion method

This chapter is dedicated to estimating the possibility of reconstructing η mesons using the conversion method. The difficulties of η reconstruction via the conversion method come mainly from their low abundance per event and the rich variety of decay channels. Therefore, in first section, different decay channels are studied separately in order to judge their reconstructability using the conversion method.

Of the variety of possible decay channels, only the double photon decay channel is suited for η reconstruction via conversion method. Results from the reconstruction analysis of η mesons are presented in Section 7.2. Based on these results, the corresponding phase space coverage of reconstructed η mesons is shown.

The rather small reconstruction efficiency removes the possibility of reconstructing η mesons with sufficient precision using small simulated data samples. To counter this, in order to see how well one can reconstruct η meson in the CBM experiment, two methods of increasing the statistics of simulated samples are tested and compared to each other. Both methods have advantages and disadvantages, which are described in Sections 7.3 and 7.4. The expectations for the performance of η multidimensional analysis using conversion method are discussed in Section 7.5. Finally, all obtained results from η reconstruction analysis are summarized in the last section.

7.1 Reconstruction of different decay channels of η meson

The reconstruction of the dilepton invariant mass spectrum requires precise understanding of the individual contributions from the different decay channels. Since the Dalitz decays of the η meson give the second biggest contribution to the background in the dilepton spectrum, it is essential to estimate the total particle yield of η mesons. In this section the possibility to reconstruct η using conversion method is considered. The estimation and analysis is made using a simulated sample of 15×10^6 UrQMD events of central Au+Au collisions with a beam energy of 8 AGeV.

The reconstruction of η mesons is even more challenging compared to the neutral pion reconstruction due to both the low abundance of η per event and the large variety of decay channels. One can calculate the theoretical probability to have a reconstructable η using the conversion

method for each channel separately. Summing up the abundance of η per event (~ 7 η per event at this energy), the conversion probability single photon ($\sim$ 5.6 %, see Section 6.4), and the branching ratio of each decay channel (see Section 2.3), one gets the following picture for each decay channel:

(a) $\eta \rightarrow \gamma + \gamma$	$\sim$	135000	reconstructable η from 15 million events,
(b) $\eta \rightarrow \pi^0 + \pi^0 + \pi^0$	$<$	1	reconstructable η from 15 million events,
(c) $\eta \rightarrow \pi^+ + \pi^- + \pi^0$	$\sim$	75000	reconstructable η from 15 million events,
(d) $\eta \rightarrow \pi^+ + \pi^- + \gamma$	$\sim$	255000	reconstructable η from 15 million events,
(e) $\eta \rightarrow \gamma + e^+ + e^-$	$\sim$	45000	reconstructable η from 15 million events.

These numbers are based on the assumption of a full 4π acceptance. In reality, the number of reconstructed η is smaller by a factor of $10 - 100$ depending mainly on the phase space coverage and acceptance.

In this work, the decay channel (b) will not be considered, because such a small signal is impossible to reconstruct with the CBM experiment via the conversion method. However, this channel might be feasible for reconstruction when using electromagnetic calorimeter.

The double photon decay channel (a) and the Dalitz decay channel (e) are treated together as one channel, since the conversion analysis is not able to distinguish the difference between them:

- $\eta \rightarrow \gamma + \gamma/\gamma^*$

the two other decay channels (c) and (d) have one positively and one negatively charged pion as decay products and, therefore are very similar. The difference between these channels is the requirement of double conversion and single conversion for type (c) and (d) correspondingly. Therefore, as a first step only the reconstructability of channel (d) is considered:

- $\eta \rightarrow \pi^+ + \pi^- + \gamma$

In order to check the reconstructability of a channel, one needs to have information about number of reconstructable particles produced while taking into account the phase space coverage of experiment and the corresponding signal to background ratio after reconstruction. If the background is several magnitudes larger than the reconstructed signal, then the analysis can not be done. The statistical and systematic uncertainties will be much higher than the signal itself in such cases.

As a first step, the reconstruction is performed using perfect particle identification (the MCtrue ID). All reconstructed charged tracks are fit and the corresponding momenta are assigned to each. With the knowledge of particle types and charges from the MCtrue ID, one separates all tracks into subclasses as electrons, positrons, and positively or negatively charged pions. All electrons and positrons are then combined into possible pairs using cuts on reconstructed pair mass of photons $m_{inv}(e^+e^-) < 20$ MeV/c^2 and the opening angle of the photons $\Theta_{e^+e^-} < 2^\circ$. All photon candidates in this chapter are selected using only these cut values.

During the reconstruction of η mesons from the decay channel $\eta \rightarrow \gamma + \gamma/\gamma^*$ one needs to apply an additional cut on opening angle between the two photons of $10^\circ < \Theta_{\gamma\gamma} < 40^\circ$ in order to reduce background (see Section 5.5). The result of η reconstruction from this channel using the MCtrue identification is shown in Figure 7.1. This method of analysis gives 12201 reconstructed η mesons and an estimated signal to background ratio of $\sim$ 0.5 %. It is expected that with the

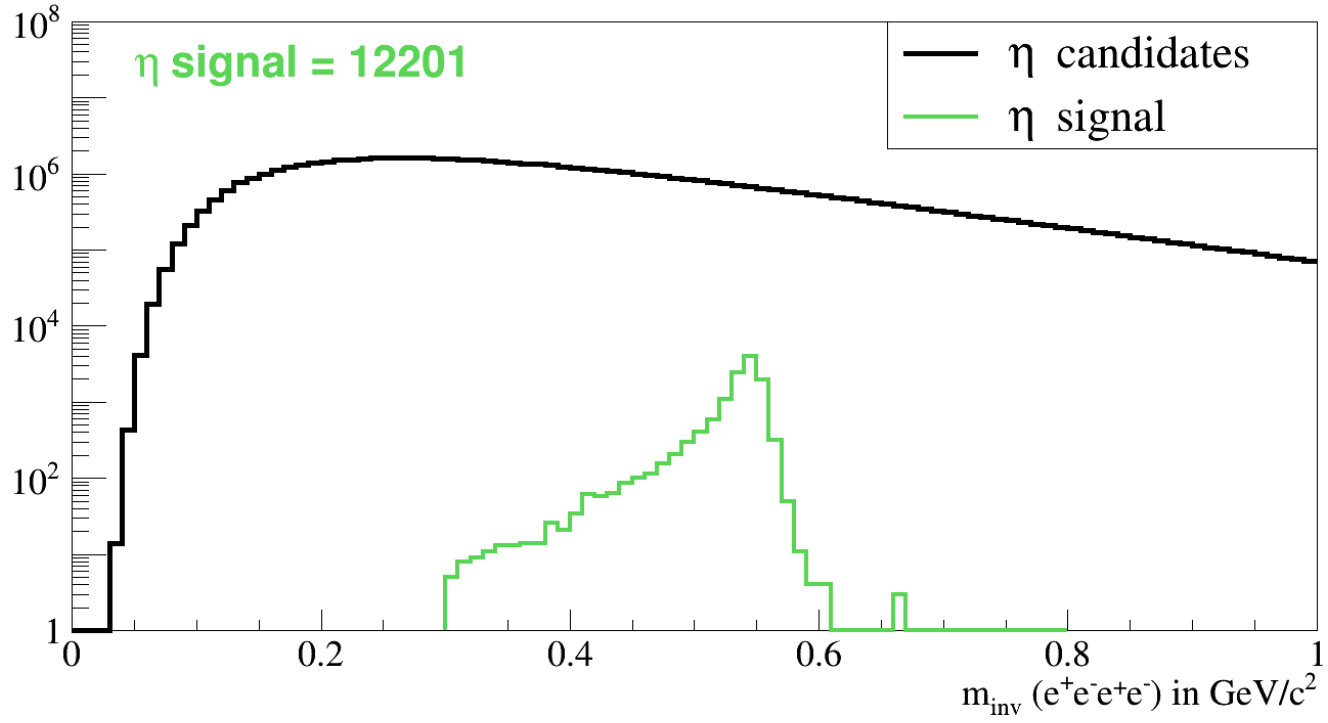

Figure 7.1: Reconstructed η invariant mass spectrum from the $\eta \to \gamma + \gamma/\gamma^*$ decay channel using the MCtrue identification. In the corner the amount of correctly reconstructed η is shown.

full reconstruction procedure (taking into account all detector uncertainties) the S/B will be even smaller, but the signal should be still reconstructable.

For η reconstruction in channel $\eta \to \pi^+ + \pi^- + \gamma$, one needs to form all possible combinations

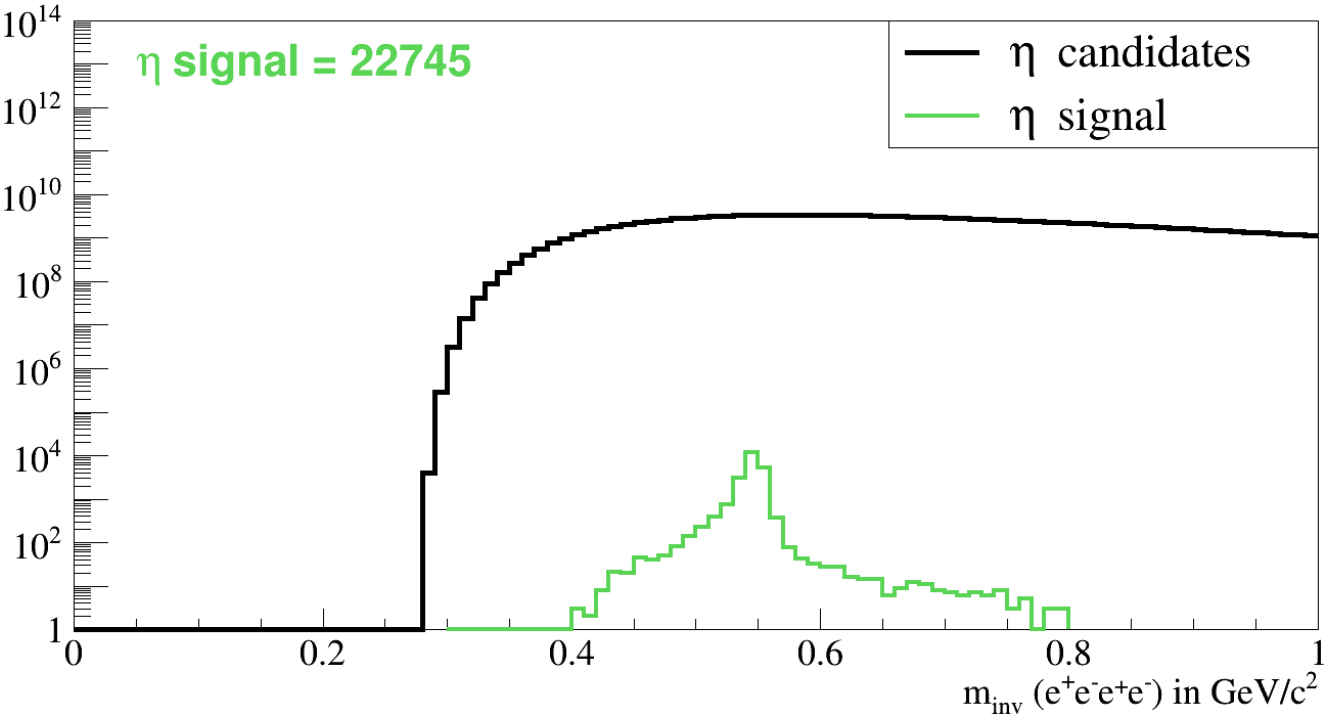

Figure 7.2: Reconstructed η invariant mass spectrum from the $\eta \to \pi^+ + \pi^- + \gamma$ decay channel using the MCtrue identification. In the corner the amount of correctly reconstructed η is shown.

using one reconstructed photon and two charged pions. In this channel, due to the large amount of charged pions coming from the primary ion collision a much higher background is expected. At the same time, however, the signal must be also much higher because only one photon needs to be converted. Unfortunately, there are no additional cuts which can decrease the combinatorial background. The reconstructed η invariant mass in this channel using MCtrue particle identification is shown in Figure 7.2. The number of reconstructed η mesons is 22745 and the signal to background ratio is $\sim 10^{-6}$ %. Taking into account all detector features one can expect a signal to background ratio from the experimental data analysis for this channel of around 10^{-7} %. Unfortunately, this decay channel will be unreconstructable due to the large background.

The results obtained above show that there is no need to check reconstructability of decay channel (c) $\eta \to \pi^+ + \pi^- + \pi^0$, as the expected signal to background ratio from the experimental data will be $\sim 10^{-9}$ %, which is unreconstructable.

Considering these results, only $\eta \to \gamma + \gamma/\gamma^*$ decay channel is suitable for reconstruction of η meson using conversion method.

7.2 Full reconstruction analysis of η mesons from the double photon decay channel

In order to make a realistic η estimation, one needs to perform a full analysis chain for the decay channel $\eta \to \gamma + \gamma/\gamma^*$ including all detector uncertainties and the limitations of the reconstruction procedure. The present analysis for η is very similar to the neutral pion analysis, and therefore, repeats all reconstruction steps applied to the π^0 case in previous chapter. The only difference in the analysis chain is the application of an additional cut on the opening angle between two photons: $10^\circ < \Theta_{\gamma\gamma} < 40^\circ$. The results of this full reconstruction analysis are shown in Figure 7.3, again separating three different variants of particle identification: full, partial, and without lepton identification within the RICH detector. A 7^{th} degree polynomial fit is used to model the background. The fit is performed in the range $0.3 - 0.5$ MeV/c^2 and $0.6 - 1.0$ MeV/c^2 excluding the signal region. The reconstruction results can also be seen in Table 7.1.

case	m_η, MeV/c^2	σ, MeV/c^2	counts in 3σ	S/B in %	η from MCtrue in 3σ
"two"	550.0 ± 28.1	10.0 ± 4.5	449 ± 539	0.31 ± 0.37	538
"onetwo"	548.1 ± 5.9	10.0 ± 4.1	5829 ± 1941	0.31 ± 0.10	2825
"all"	541.5 ± 4.7	6.3 ± 3.9	3753 ± 2508	0.12 ± 0.08	3587

Table 7.1: Reconstruction results from the full reconstruction analysis of the $\eta \to \gamma + \gamma/\gamma^*$ decay channel using different lepton identification approaches.

The analysis approach using full lepton identification has a very low fraction of reconstructed η mesons = 538 (cross checked with MCtrue data). The amount of reconstructed η from the full analysis chain, as obtained by a Gaussian fit of the η signal peak after background subtraction, results in 449 ± 539 reconstructed η. This number is comparable within errors to the true number contained in this spectrum. The large errors occur because the η peak on the graph is barely recognizable among statistical deviations of the background. If one would not know about the presence of some particle there, one would probably consider the region between 0.5 GeV/c^2 and 0.6 GeV/c^2 only as statistical deviations. The small amount of reconstructed particles comes mainly from the η feature of having a relatively large opening angle between the decayed photons. After the conversion of such photons, the probability to have all four leptons identified in the RICH detector is very low. The signal to background ratio from the analysis is equal to $\sim 0.5\%$.

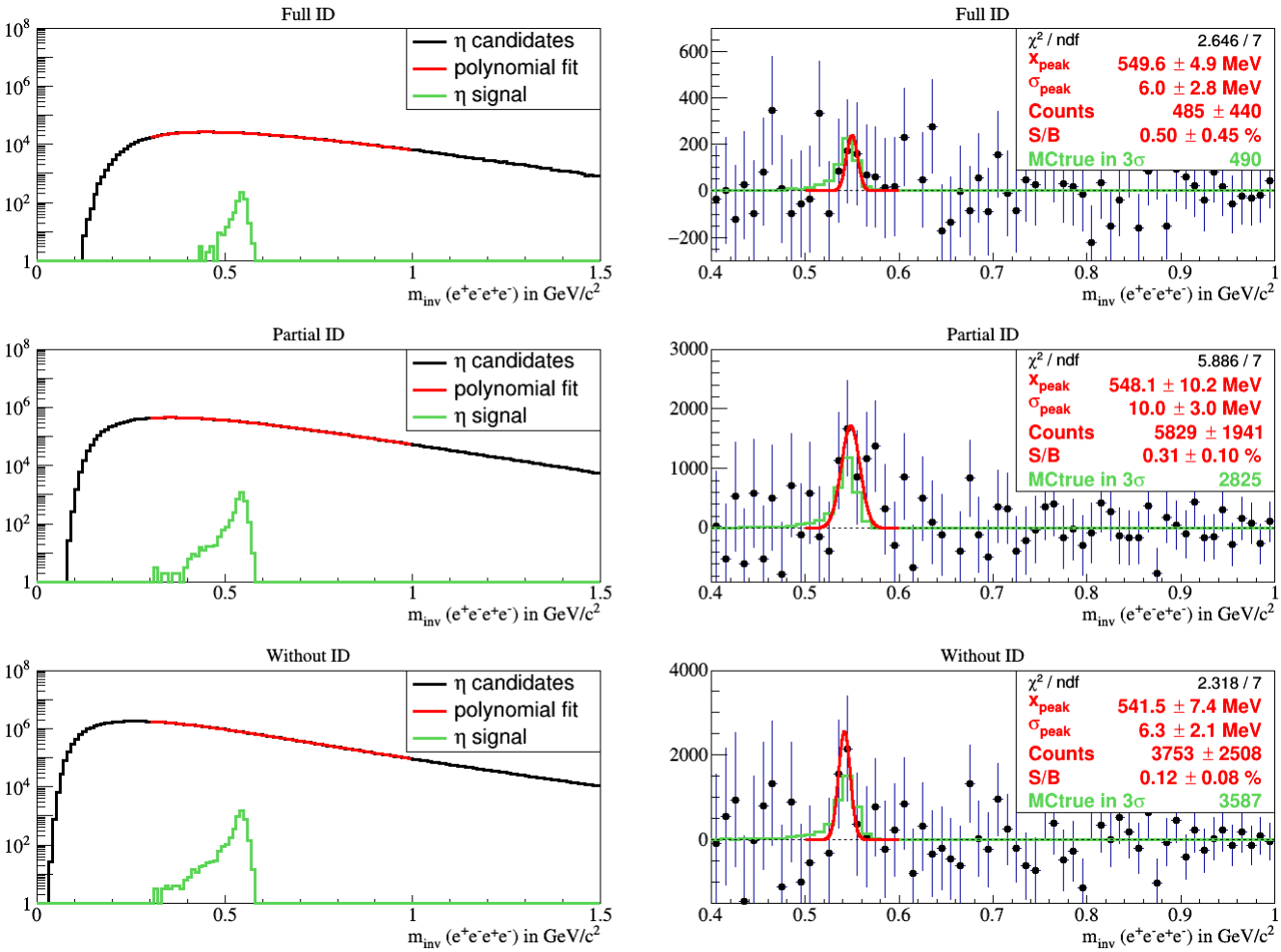

Figure 7.3: Reconstructed (left column) and background-subtracted (right column) invariant mass spectra of η meson from the $\eta \rightarrow \gamma + \gamma/\gamma^*$ decay channel using different lepton identification approaches: full (upper row), partial (middle row), without (bottom row). Green line at all graphs shows correctly reconstructed η signal contained in spectra.

The approach with partial lepton identification shows an increase in signal by a factor of 5, but at the same time the background increases by a factor of 10 in the η peak region as compared to the analysis with full identification. The number of reconstructed η mesons contained in the invariant mass spectrum is equal to 2825 (cross checked with MCtrue data). The complete analysis routine, on the other hand, gives slightly larger number of reconstructed η: 5829 ± 1941. Although the signal peak looks like a proper peak, the obtained results disagree due to the random statistical enhancement directly on the right side of the signal. Because of this difference, the extracted signal to background ratio in this particular situation can not be trusted. Taking into account correct number of reconstructed particles, the signal to background ratio should be $\sim$ 2 times smaller and roughly equal to ~ 0.2 %.

The approach without lepton identification shows an increase in signal by a factor of 7, but also an increase in the background by a factor of 30 when compared to the full identification analysis. The η peak is clearly seen on the background-subtracted spectrum and results in 3753 ± 2508 reconstructed η, which is very close to the true number of η mesons contained in this spectrum 3587 (cross checked with MCtrue data). The signal to background ratio from this approach is the smallest of any method but still at the permill level: ~ 0.1 %.

The phase space coverage of reconstructed η, as well as the reconstruction efficiency in terms

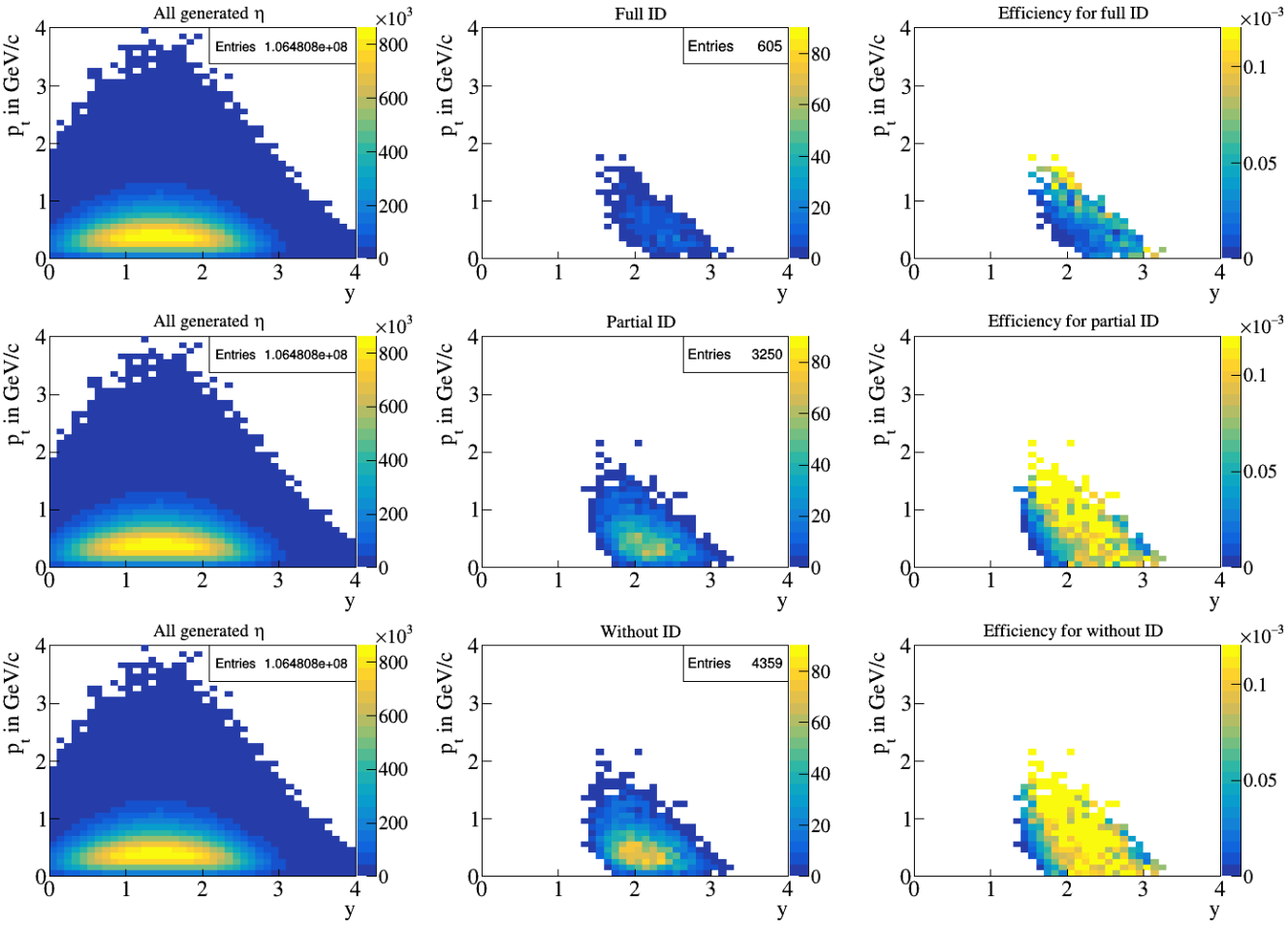

Figure 7.4: Reconstruction efficiency (right column) of η as function of transverse momentum p_t and rapidity y for three analysis approaches: full (upper row), partial (middle row), without (bottom row).

of transverse momentum p_t and rapidity y (based on MCtrue information), are shown in Figure 7.4. The reconstruction efficiency (right plot) is obtained by dividing the corresponding number of correctly reconstructed η (middle plot) by all generated η in the simulated sample (left plot). The color scale for pictures in the right column is always the same. Figure 7.4 shows, that the phase space coverage for the η analyses is similar to the phase space coverage of π^0 analyses (see Figure 6.5) for all identification approaches. The efficiency for η mesons, reconstructed via the $\gamma\gamma$ decay branch, is smaller than for π^0 by a factor of 4. This is mainly due to the larger number of different decay channels for the η meson, and thus, smaller $\gamma\gamma$ branching ratio.

As can be seen from the middle column in Figure 7.4, the reconstructed number of η for different rapidities and transverse momenta differs strongly. Typically during the data analysis, one analyzes not only the integrated spectrum, but also each separate rapidity and transverse momentum region. This multidimensional analysis gives information about possible dependencies of the peak position, peak width, number of reconstructed particles, and signal to background ratio on the $y - p_t$ phase space. Due to the lack of statistics, one can not do such analysis for η in this thesis, but it can be done with experimental high statistics data samples.

7.3 Modeling and full analysis of a high statistics input data sample

The low abundance of reconstructed η from a sample of 15 million simulated events does not allow for the possibility of seeing how accurate one can count η using the double conversion reconstruction method. This simulation sample already needs about 30 TB of disk space for storage, even though the detector setup does not include TRD, TOF, ECAL, and PSD detectors. Unfortunately, this is the maximum disk space currently available local for data storage. Therefore, alternative ways to simulate larger data samples are needed.

In Section 7.1 it was shown that in only roughly 1 event out of 100 can an η meson be reconstructed via decay channel $\eta \rightarrow \gamma + \gamma/\gamma* \rightarrow (e^+ + e^-) + (e^+ + e^-)$. The remaining events contribute only to the background of the η invariant mass spectrum. In storage space equivalent, approximately 29.7 TB of the data is background and only 0.3 TB contains signal.

During the simulation process within the CbmRoot framework, one can select individual events for storage. With help of this feature a 100×10^6 UrQMD events of central Au+Au collisions at a beam energy of 8 AGeV were simulated, but only events, where the η decayed into two photons, which converted into e^+e^- pairs were kept (checked using MCtrue information). Overall, from 100×10^6 simulated events only $\sim 1.4 \times 10^6$ events were stored, henceforth called the "signal-enriched" sample. These $\sim 1.4 \times 10^6$ signal events need only 3 TB storage space. The disadvantage of this "trick" is an unrealistic signal to background ratio.

In Figure 7.5 the invariant mass spectra of η candidates obtained by using the same analysis chain, used in Section 7.2, on the "signal-enriched" sample is shown. Due to background rejection during the simulation, one can clearly see an η peak after reconstruction using all three approaches for particle identification. Some combinatorial background is still present in the final invariant mass spectra as within every event one has a lot of converted photons from π^0, which also used to form possible η candidates. Using MCtrue information, one can extract the correctly reconstructed η contained in the final spectra alone (green line in corresponding graphs).

The obtained invariant mass spectra in Figure 7.5 can not be used for η analysis since they do not contain realistic background. However, one can extract correctly reconstructed signal (green line in Figure 7.5) and later on add the corresponding background on top. To do this the modulated background must correspond to the same amount of events, same collision system, and the same beam energy, as the simulated signal. Assuming, that one has only combinatorial background (without any correlated background) in the final invariant mass spectrum, one can easily modulate the corresponding background with help of event mixing technique using a much lower number of events.

In order to simulate the necessary EMT spectrum, one performs the normal analysis with 15 million simulated events used in Section 7.2. All reconstructed photon candidates during the analysis are stored in a buffer array with all relevant information. By varying the size of the buffer, one can easily adjust the final EMT spectrum to correspond to desired amount of background (as calculated via Formula 6.1 in Section 6.1). For the analysis presented here, a EMT spectrum corresponding to 100 million events with the corresponding statistical errors is used.

Having both the η signal and background spectrum corresponding to 100 million events separately, one can combine them together to form the final spectrum. Later on, the following analysis is performed using this spectrum: combinatorial background is first fit with a 7^{th} degree polynomial, the background is subtracted, the remaining peak is fit with a Gaussian, and all interesting information is extracted from the reconstructed peak. The final results after background subtraction and the fitting routine can be seen in Figure 7.6. Results obtained from the peak reconstruction are shown in Table 7.2.

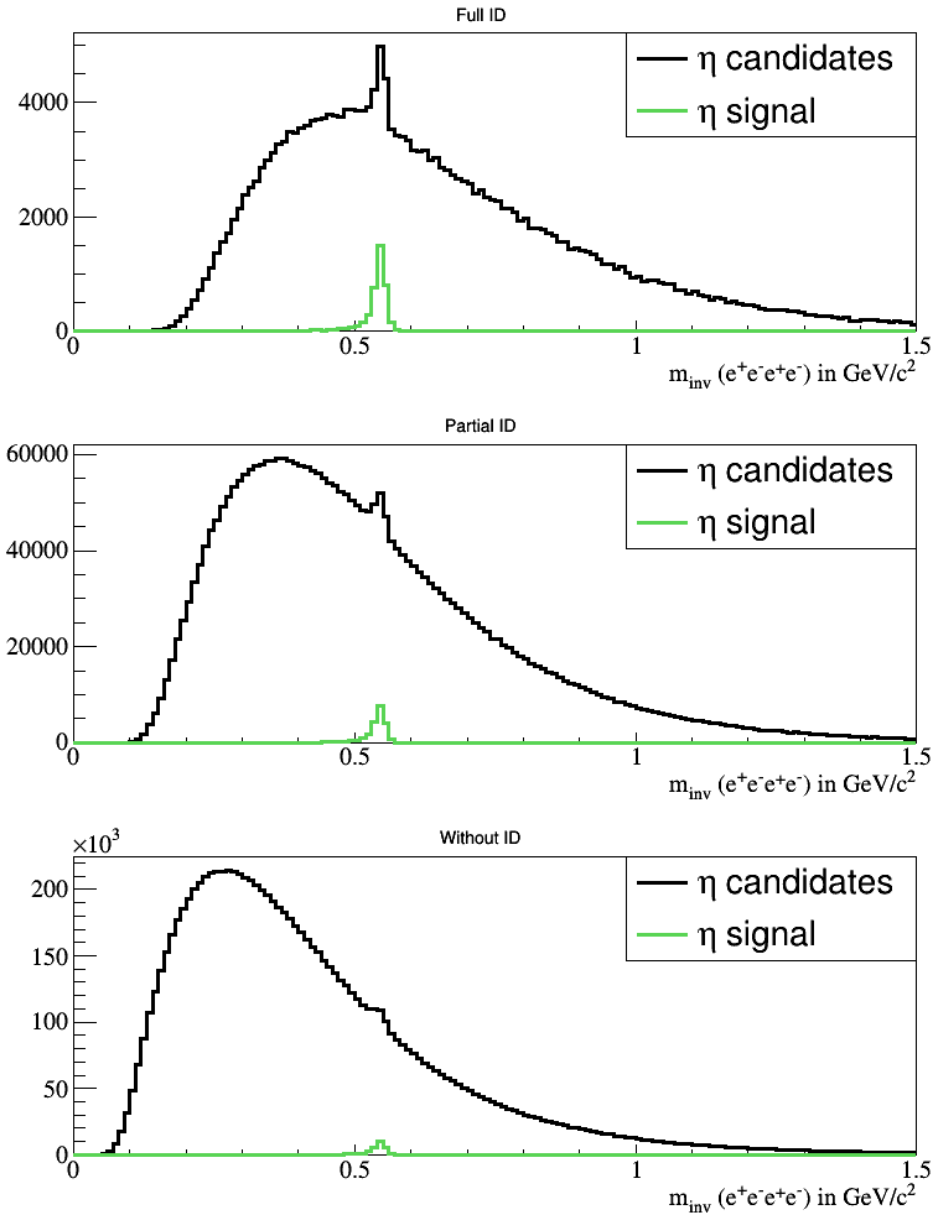

Figure 7.5: Reconstructed invariant mass spectrum of η from "signal-enriched" simulated sample using three analysis approaches: full (upper), partial (middle), without (bottom).

One can see from Table 7.2 that the position of the η peak after reconstruction slightly differs from the theoretical prediction, but is very close. The shape of η peaks is also very close to a Gauss function, which simplifies fitting. The extracted η peak width has a small deviation for every approach, but stays in the range of errors. The mean width is $\sigma = 9.1 \pm 2.6$ MeV/c^2. The number of reconstructed η mesons is in agreement with the true amount of η contained in the invariant mass spectra (cross checked with MCtrue data). The relatively large error values in the number of reconstructed η mesons occurs due to the rather low reconstruction efficiency of the particle. In order to have higher precision, an even bigger data sample is required.

The expected S/B ratio for analysis using the full identification approach is 0.52 %, which is the highest seen and is due to the precise lepton identification. For the partial identification approach, a S/B ratio at the level of 0.15 % is expected. In case without lepton identification the signal to background ratio is the smallest and equals 0.10 %. The use of extreme case without identification is not recommended since only small number of additional η mesons are reconstructed compared

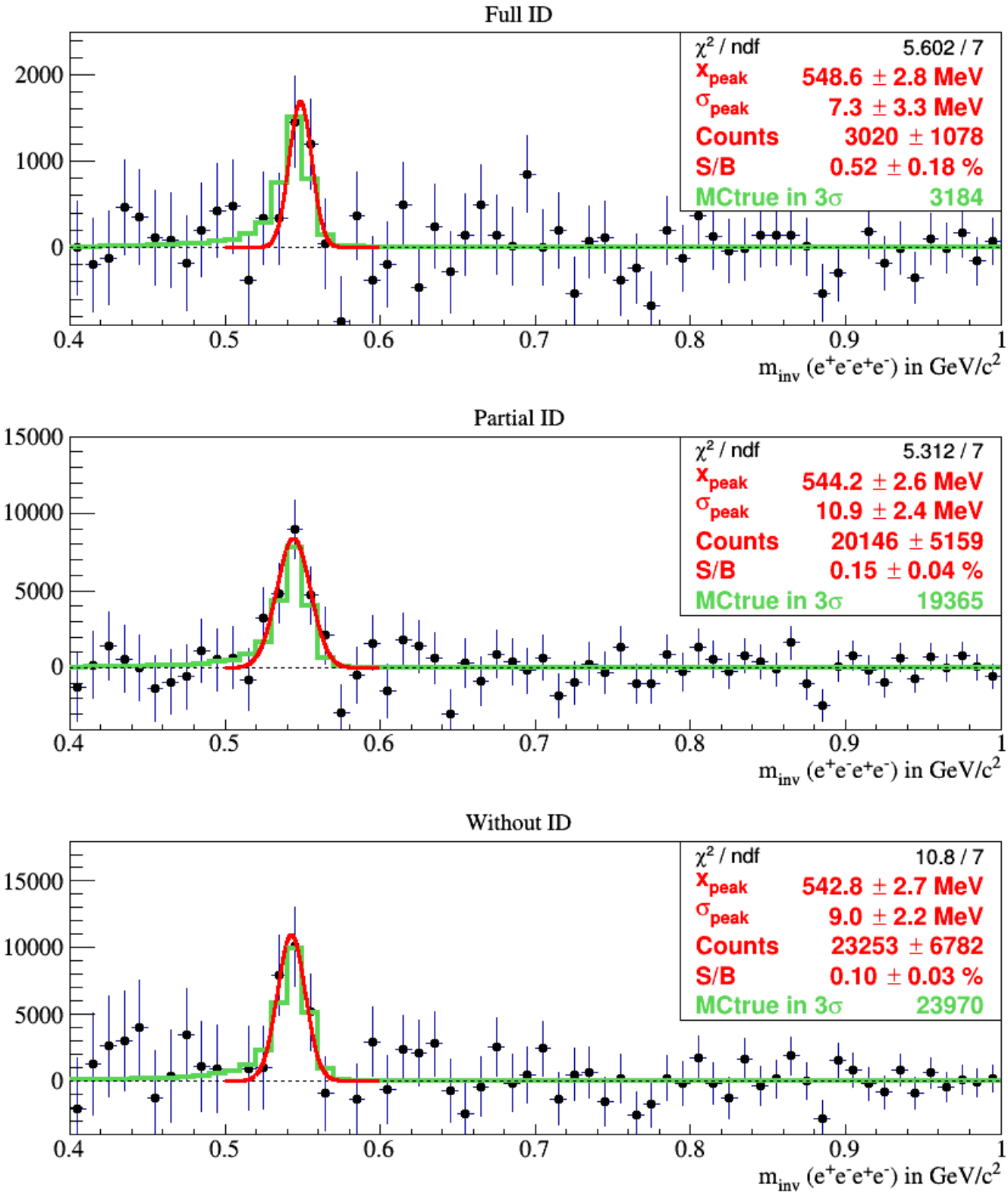

Figure 7.6: Reconstruction results for the $\eta \rightarrow \gamma + \gamma/\gamma*$ decay channel using combined invariant mass spectra corresponding to 100 million central Au+Au events. Three cases of particle identification are listed: full (upper), partial (middle), without (bottom).

case	m_η, MeV/c^2	σ, MeV/c^2	counts in 3σ	S/B in %	η from MCtrue in 3σ
"two"	548.6 ± 2.8	7.3 ± 3.3	3020 ± 1078	0.52 ± 0.18	3184
"onetwo"	544.2 ± 2.6	10.9 ± 2.4	20146 ± 5159	0.15 ± 0.04	19365
"all"	542.8 ± 2.7	9.0 ± 2.2	23253 ± 6782	0.10 ± 0.03	23970

Table 7.2: Reconstructed information from the $\eta \rightarrow \gamma + \gamma/\gamma*$ decay channel from combined invariant mass spectrum corresponding to 100 million central Au+Au events.

to the partial identification approach, and it dramatically increases the amount of background.

7.4 Consistency of combined analysis with full analysis

Since the method described in previous section has been applied for the first time, one can not be sure that it gives proper results. Therefore, the method reliability must be tested by comparison to a full simulation of 100 million events.

Since the storage of samples as big as 100 million events can not be done, one can run a full simulation-analysis chain based on several small simulation samples:

- Simulate a small fraction of events (for example 1 million) in standard way, take final histogram, and delete simulated files.
- Simulate another small fraction of events, take final histogram, add it to the first one, delete events.
- Do until one gets the simulation sample corresponding to 100 million events.

In this approach the use of computing power is still 100 %, but space consumption is reduced by a factor of 100, due to 100 individual simulation steps, each of which is always deleted after each step. Since, at the moment, the main limitation factor is storage space and not computing power, this is the best way to obtain a full simulation of 100 million events.

In this way one can perform reconstruction analysis completely based on full simulated data sample as it would be done from experimental data. This is the only advantage of such approach. The largest disadvantage of this method is that one can not change anything for the analysis without re-simulating everything. This method also requires a huge computing time, and therefore can not be used regularly. As an example, for the simulation of 100 million events on the computing farm using 1000 cores simultaneously one needs to wait two weeks.

case	m_η, MeV/c^2	σ, MeV/c^2	counts in 3σ	S/B in %	η from MCtrue in 3σ
"two"	540.0 ± 2.9	8.2 ± 2.7	3574 ± 1146	0.54 ± 0.17	3268
"onetwo"	546.1 ± 2.7	10.0 ± 2.1	18379 ± 5010	0.15 ± 0.04	18656
"all"	545.9 ± 3.2	10.1 ± 2.4	27921 ± 7760	0.09 ± 0.03	24238

Table 7.3: Reconstructed information from the $\eta \rightarrow \gamma + \gamma/\gamma*$ decay channel from full simulation of 100 million central Au+Au events.

The reconstruction analysis for η meson via double conversion on this sample is performed in the same way as in Section 7.2. The final results after background subtraction and the fitting routine from the full simulation of 100 million events are shown in Figure 7.7. The results can be also seen in Table 7.3.

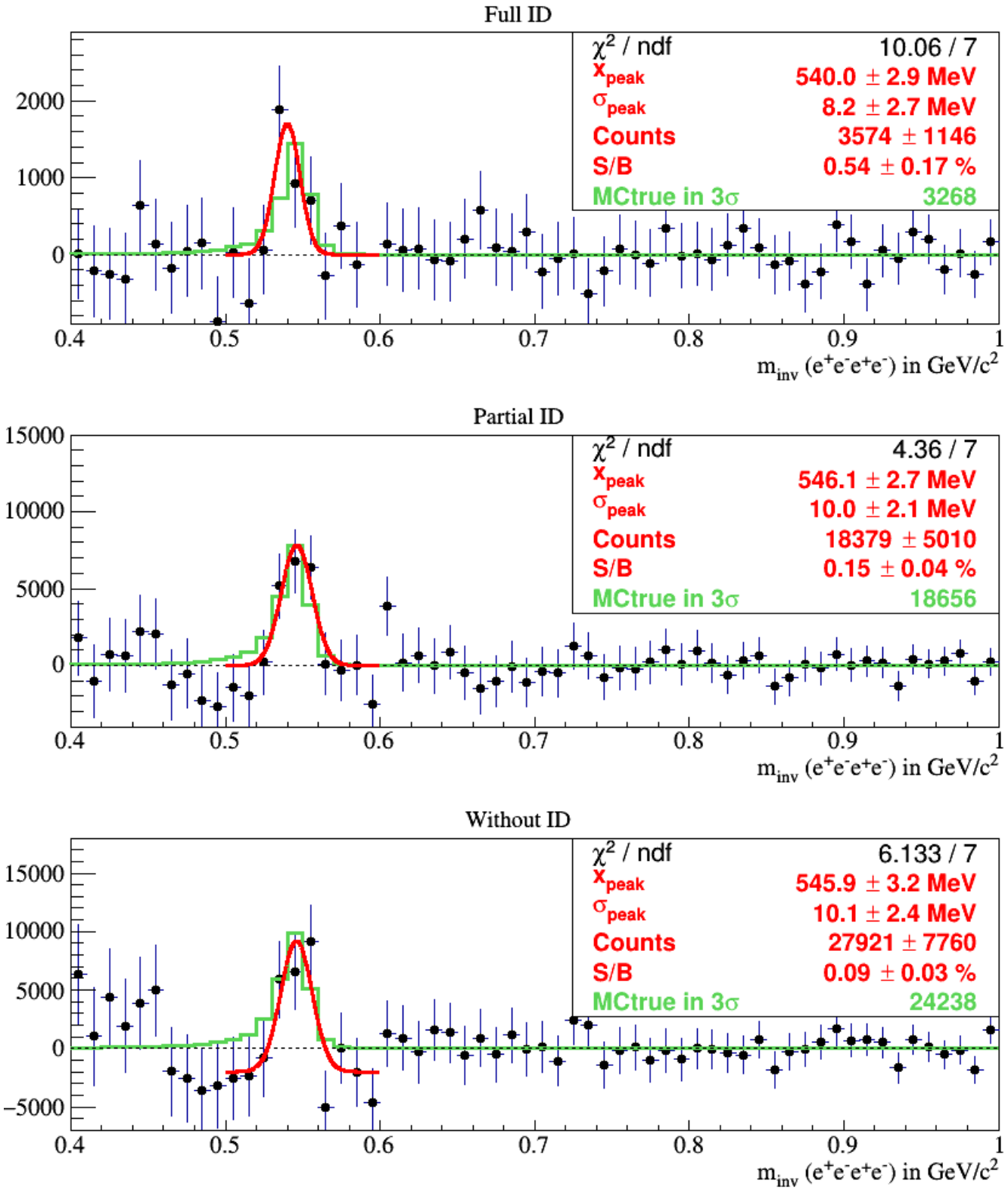

Figure 7.7: Reconstruction results for the $\eta \rightarrow \gamma + \gamma/\gamma*$ decay channel using full simulation of 100 million central Au+Au events. Three cases of particle identification are listed: full (upper), partial (middle), without (bottom).

Having these results in hand, one can compare the two approaches (Figure 7.6 and Figure 7.7). Overall one can see very good agreement between both approaches. Obtained fit results are comparable in the range of errors between the two approaches. There is a small difference in the peak position for the case with full lepton identification, but it appears to be due to insignificant statistic deviations. Such good agreement in results confirms reliability of the method described in Section 7.3.

Comparing the advantages and disadvantages of both approaches, it is better to use the combination of the signal spectrum with the corresponding combinatorial background when one needs to perform a simulation with high statistics. This method is more well suited for cases where the analysis is still under investigation. The second method with deleting simulation files should be used only as a final check of the final analysis.

Overall 100 million central Au+Au events are enough to properly reconstruct η meson with moderate precision. The obtained results corresponding to 100 million central Au+Au events at a beam energy of 8 AGeV can be easily achieved with the CBM experiment. Assuming the interacting rate for the experiment $\sim$ 100 kHz and only 1 % of central events, the necessary 100 million central Au+Au events will be achieved by the CBM experiment in 10^5 seconds of operation time, which equals $\sim$ 28 hours of data taking.

7.5 Multidimensional signal to background ratio for η reconstruction

A similar analysis as was done in previous section, can also be performed separately for different phase space bins. It is expected that during such analysis, different phase space regions will have different amount of reconstructed signal and background. The reconstruction analysis must always be done multidimensionally in order to get better knowledge about particle properties. Unfortunately, our available 100 million central events do not allow for the extraction of multidimensional signal peaks with acceptable precision for fitting, therefore here, the estimation for limited phase spaces is based on the MCtrue number of reconstructed η. The multidimensional estimation is shown here, as an example, for the case with partial lepton identification. The analysis is performed for the rapidity range $1.2 - 3.2$ with a bin step of 0.4, and for the transverse momentum range $0.0 - 1.6$ GeV/c with a bin step of 0.4 GeV/c. During the reconstruction routine in previous section the final η spectrum (η candidates) was separated into corresponding bins depending on their reconstructed rapidity and transverse momentum.

The final results with the number of correctly reconstructed η mesons in the invariant mass spectrum, the amount of background in 3σ region (σ = 10 MeV/c^2), and the expected signal to background ratio can be found in Table 7.4. Bins with very small statistics and empty bins are not listed in the table.

Overall, the signal to background ratio remains on the permill level for all phase spaces: the smallest is 0.1 % and the biggest is 0.41 %. Some bins have quite a large amount of reconstructed η, as an example, $y = 2.0 - 2.4$ at $p_t = 0.4 - 0.8$ GeV/c has 4174 reconstructed η mesons. This bin also has a large combinatorial background, which results in a roughly $\sim$ 0.2 % signal to background ratio. On the other hand, some bins such as $y = 1.2 - 1.6$ at $p_t = 1.2 - 1.6$ GeV/c or $y = 2.8 - 3.2$ at $p_t = 0.4 - 0.8$ GeV/c have only $\sim$ 72 reconstructed η from the 100 million central Au+Au events and, therefore, are extremely hard to reconstruct, although in these cases the signal to background is similar to other bins. Such low statistics bins can be also nicely reconstructed, but they require huge amount of experimental data.

rapidity range	p_t range in GeV/c	η in bin	background in bin	S/B ratio	efficiency
1.2 - 1.6	0.4 - 0.8	161	153567	0.10 %	0.02×10^{-4}
1.2 - 1.6	0.8 - 1.2	182	139557	0.13 %	0.1×10^{-4}
1.2 - 1.6	1.2 - 1.6	74	54409	0.14 %	0.2×10^{-4}
1.6 - 2.0	0.0 - 0.4	1624	1684127	0.10 %	0.3×10^{-4}
1.6 - 2.0	0.4 - 0.8	3136	2333799	0.13 %	0.5×10^{-4}
1.6 - 2.0	0.8 - 1.2	1511	868677	0.17 %	1.0×10^{-4}
1.6 - 2.0	1.2 - 1.6	430	213717	0.20 %	1.6×10^{-4}
2.0 - 2.4	0.0 - 0.4	4103	2652770	0.15 %	0.8×10^{-4}
2.0 - 2.4	0.4 - 0.8	4174	2051904	0.20 %	1.0×10^{-4}
2.0 - 2.4	0.8 - 1.2	1191	501264	0.24 %	1.5×10^{-4}
2.0 - 2.4	1.2 - 1.6	147	59650	0.25 %	1.4×10^{-4}
2.4 - 2.8	0.0 - 0.4	2691	1005438	0.27 %	1.0×10^{-4}
2.4 - 2.8	0.4 - 0.8	1400	525277	0.27 %	1.0×10^{-4}
2.4 - 2.8	0.8 - 1.2	142	58656	0.24 %	0.8×10^{-4}
2.8 - 3.2	0.0 - 0.4	510	125392	0.41 %	0.9×10^{-4}
2.8 - 3.2	0.4 - 0.8	72	30598	0.23 %	0.3×10^{-4}

Table 7.4: Multidimensional expectations from η analysis for different phase spaces in terms of rapidity and transverse momentum. The values are based on MCtrue information using partial lepton identification in the analysis.

7.6 Summary

In this chapter, the possibility of reconstructing η mesons by the conversion method has been investigated. The study has shown, that among all decay channels of η only the $\eta \to \gamma + \gamma/\gamma^*$ channel can be reconstructed using conversion method.

As a first step, the reconstruction of η mesons has been tested using a simulated sample of 15 million UrQMD central Au+Au events. Due to the low abundance of η per event and large diversity of decay channels, it was challenging to estimate the amount of reconstructed η mesons with good precision from this sample. In order to increase the precision, a data sample with larger statistics is required. Unfortunately, because of the limited disk space available, it was impossible to store more events for the analysis. Because of this the following two alternative methods to produce a high statistics data sample were considered.

The first method is based on combination of separate signal and background invariant mass spectra. The signal spectrum is obtained with help of the CbmRoot feature of saving only selected events, where double conversion of photons from η decay occurred. The background spectrum is simulated using an Event Mixing Technique.

The second method is based on several small simulation samples produced in the standard way, each of which are then deleted after every batch.

A comparison of the accuracy of both methods has been done for 100 million central Au+Au events. Obtained results for both methods are comparable in the range of errors. There is a small difference in the fitting parameters, which is mainly due to statistical deviations. Such a good agreement in results confirms reliability of the first method.

Both approaches have some advantages and disadvantages. The first method, where final spectrum is combined from two separate spectra, is preferable, since it is flexible to any changes in the analysis. The disadvantage is that it does not include the correlated physical background. The second method can be used only as a check of the final analysis, as it requires significant

case	m_η, MeV/c^2	σ, MeV/c^2	counts in 3σ	S/B in %	η from MCtrue in 3σ
set 1:	$m_{inv}(e^+e^-) < 10$ MeV/c^2; $\Theta_{e^+e^-} < 1°$; $10° < \Theta_{\gamma\gamma} < 40°$				
"two"	548.4 ± 2.7	6.5 ± 3.6	1830 ± 854	0.50 ± 0.23	2059
"onetwo"	544.9 ± 2.4	9.3 ± 3.4	13012 ± 2777	0.34 ± 0.07	11538
"all"	542.7 ± 3.0	10.9 ± 3.9	14547 ± 4402	0.15 ± 0.05	15446
set 2:	$m_{inv}(e^+e^-) < 20$ MeV/c^2; $\Theta_{e^+e^-} < 2°$; $10° < \Theta_{\gamma\gamma} < 40°$				
"two"	548.6 ± 2.8	7.3 ± 3.3	3020 ± 1078	0.52 ± 0.18	3184
"onetwo"	544.2 ± 2.6	10.9 ± 2.4	20146 ± 5159	0.15 ± 0.04	19365
"all"	542.8 ± 2.7	9.0 ± 2.2	23253 ± 6782	0.10 ± 0.03	23970
set 3:	$m_{inv}(e^+e^-) < 30$ MeV/c^2; $\Theta_{e^+e^-} < 3°$; $10° < \Theta_{\gamma\gamma} < 40°$				
"two"	549.5 ± 2.7	7.9 ± 2.5	3433 ± 1346	0.38 ± 0.15	3613
"onetwo"	545.9 ± 3.0	10.4 ± 2.4	24114 ± 7872	0.08 ± 0.03	22194
"all"	544.2 ± 4.2	7.2 ± 2.3	26298 ± 9593	0.03 ± 0.01	27570
set 4:	$m_{inv}(e^+e^-) < 40$ MeV/c^2; $\Theta_{e^+e^-} < 4°$; $10° < \Theta_{\gamma\gamma} < 40°$				
"two"	548.0 ± 4.4	8.3 ± 3.0	3593 ± 1737	0.24 ± 0.12	4054
"onetwo"	549.5 ± 3.0	9.4 ± 3.0	23741 ± 10108	0.05 ± 0.02	22290
"all"	-	-	-	-	-
set 5:	ANN value > 0.9; $10° < \Theta_{\gamma\gamma} < 40°$				
"two"	550.0 ± 4.5	7.1 ± 3.2	3128 ± 1154	0.47 ± 0.17	3552
"onetwo"	546.8 ± 2.4	10.2 ± 3.5	18347 ± 4377	0.19 ± 0.05	19449
"all"	544.2 ± 2.5	11.0 ± 0.2	30712 ± 7505	0.12 ± 0.03	26534

Table 7.5: Obtained results from η reconstruction analysis using different particle identification approaches. Analysis is performed using combined invariant mass spectra corresponding to 100 million central Au+Au events.

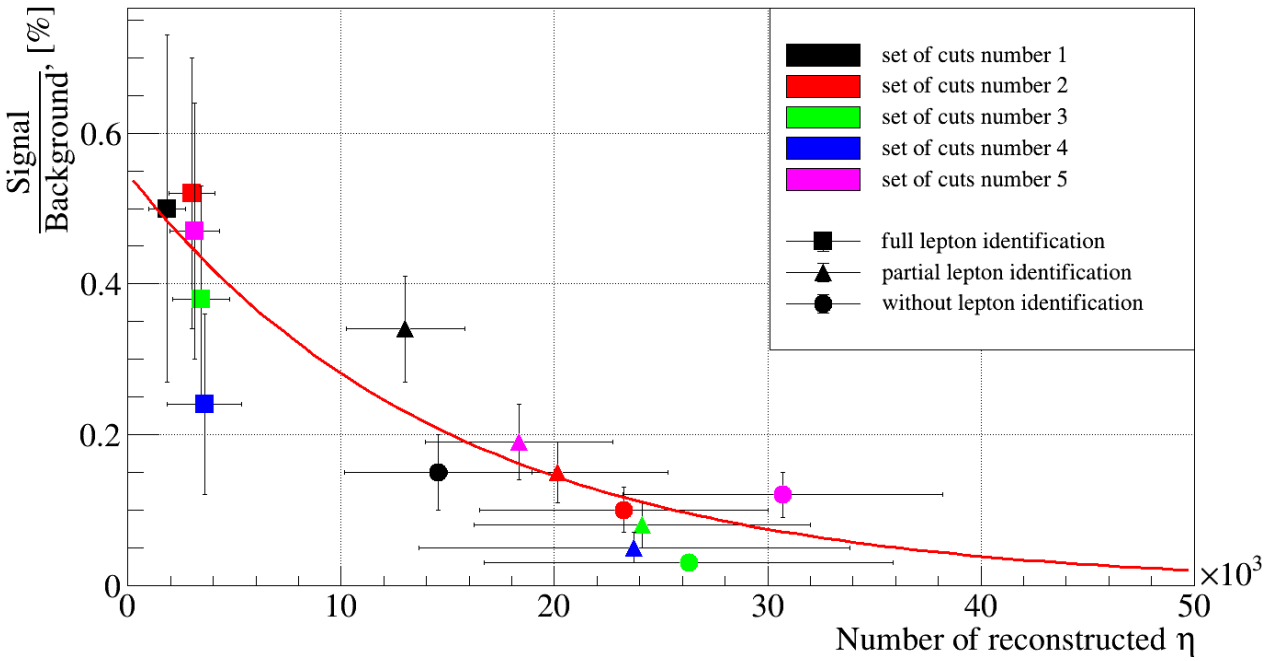

Figure 7.8: Correlation between reconstructed number of η and signal to background ratio. Different colors belong to different sets of cuts. The 3 different approaches on particle ID are shown with squares, triangles, and circles respectively.

amounts of computing power and time.

Using the flexibility of the first method, different set of cuts have been tested. The final results of the analysis for each of the three identification approaches using different sets of cuts are summarized in Table 7.5. It contains the results using different strict cut values, as well as an ANN cut used for the photon selection. In analogy to the π^0 analysis, the ANN cut for η analysis shows similar results as those obtained using strict cuts on invariant mass of photons $m_{inv}(e^+e^-) < 20$ MeV/c^2 and opening angle of photons $\Theta_{e^+e^-} < 2^\circ$.

There are no results for the case without identification approach using cut values $m_{inv}(e^+e^-) < 40$ MeV/c^2 and $\Theta_{e^+e^-} < 4^\circ$ due to the inability to distinguish η peak because of the poor signal to background ratio. The other two approaches do not have any problems with reconstruction of the η peak using same cuts.

The optimal cut values for η reconstruction are: "set 1" and "set 2" (see Table 7.5). Other higher cuts are not recommended for use, since by using them one might observe additional correlated background (as it was observed in π^0 reconstruction) which is absent in this high statistics analysis based on modeled invariant mass spectrum.

The graphical representation of Table 7.5 is shown in Figure 7.8. The correlation between points is assumed to have roughly exponential dependence as was the case in the analysis of π^0, therefore all points have been fit with an exponential function (red curvature in Figure 7.8). The exponential dependence is not as pronounced as for π^0, but this is mainly due to the relatively large errors for η estimation in comparison to π^0 estimation.

Overall, 100 million central Au+Au events are enough to properly reconstruct the η meson with rather moderate precision. To obtain this amount of events in CBM, one needs ~ 28 hours of data taking at interaction rate of 100 kHz. With such a sample one can count number of reconstructed η with an accuracy of ~ 30 %.

8

Use of conversion analysis method for temperature estimation of emitting source

All particles produced in a heavy ion collision have distinct properties predefined by the time when they are formed. Having these properties in hand, one can extract information about the time when these particles were formed, as well as the size and temperature of the system at that time. In this chapter, the ability of making use of the conversion analysis method, developed in previous chapters, to derive the temperature of the emitting source is estimated.

Due to the small reconstruction probability and the strong phase space dependence of the conversion method, a full efficiency and acceptance correction is needed in order to get a temperature estimation. This chapter starts with a brief explanation of the general analysis procedure for temperature estimation using any type of particle.

Later on, this procedure is described in detail in Section 8.2 and applied to derive a good estimation of the emitting source temperature using π^0 reconstructed from measured leptons. The obtained value is then compared to the MCtrue value in order to evaluate the performance of the approach.

The third section is dedicated to a first attempt to apply the conversion method in the CBM experiment to reconstruct the direct photon spectrum. The section describes the acceptance and efficiency corrections for the direct photon analysis, shows the different background contributions to the photon reconstruction, and the ability to use such an analysis for temperature estimation from direct photons.

8.1 Analysis strategy

The studies shown in this thesis are based on simulations mainly using the UrQMD event generator. This generator does not produce events according to a realistic temperature-momentum dependent distribution. However, generated the transverse momentum spectra from UrQMD have an exponential shape, and therefore, some temperature can be attributed. One can use such spectra to show whether the conversion analysis of particles can in principal be used for temperature estimation. Basically, if the extracted temperature from reconstruction is close to the temperature from MCtrue data, then it should be possible to apply the same analysis strategy later to exper-

imental data to get the temperature as well. In other words, the reconstructed slope parameter from a conversion analysis spectrum has to be the same as the slope parameter from the inputed sample.

All experiments have a limited geometric acceptance of where they can measure produced particles and the CBM experiment is no exception. It is able to reconstruct particles in a rapidity range of $y = 1.2 - 4.0$ and with transverse momentum $p_t = 0.0{-}3.0$ GeV/c. Due to this acceptance restriction, the derived slope parameter is strongly dependent on the precise phase space coverage. In order to be able to compare input and output temperatures, one needs to derive both input and reconstructed slope parameters for the same space range. Therefore, the MCtrue slope parameter will be based on the input data only from the acceptance range covered by the CBM detector.

Before deriving the source temperature from reconstructed data, one needs to take three important steps:

1. perform multidimensional reconstruction of particles
2. apply multidimensional acceptance correction
3. apply multidimensional efficiency correction

Multidimensional corrections depend on the data selection cuts, so the corrections are specific for the set of cuts used to derive them. Also, for each kind of reconstructed particle, separate acceptance and efficiency corrections are needed.

Multidimensional reconstruction of particle yield (or other observables) is performed in terms of the rapidity and transverse momentum of each particle. This is important for two reasons. First, one needs to have the amount of reconstructed particles as a function of p_t in order to extract temperature parameter from the fitting of Formula 2.3. Second, a multidimensional analysis is important for the subsequent steps of acceptance and efficiency correction needed in order to obtain a model independent analysis.

The reconstructed number of particles after multidimensional analysis is only a small fraction of particles produced within the available acceptance. The main reason why not all are reconstructed, is the limited conversion probability. Another important reason is the particle identification approach used in the analysis. A lot of low momentum leptons are bent out by the magnetic field and, hence not identified. Also the bremsstrahlung effect causes additional trouble in the reconstruction of photons by reducing lepton momenta.

A proper estimation of the p_t spectrum requires full corrections for all particles lost due to the limited reconstruction probability. These differential correction factors have to be applied to the reconstructed particle yield in order to recover the produced particle yields. This full correction is separated into two steps: acceptance correction and efficiency correction. Applying these corrections, one can estimate the amount of all generated particles based on the reconstruction results.

The acceptance correction is the main correction. The multidimensional acceptance correction, as used in this context, is defined as the probability that a single particle, emitted within the geometrical detector acceptance, is reconstructed. It takes into account the large loss of particles due to conversion probability and particle identification approach. The correction heavily depends on the geometry of the experiment. In particular it depends on the amount of material where decayed photons can be converted. This includes the angle and position dependent conversion probability.

In order to obtain the acceptance correction, another type of simulation is required: in this particular case, instead of UrQMD generator, the simple box generator is used. The advantage of the box generator is that the user can generate simple particles (π, K, p, e, γ) in dedicated

phase space regions with a predefined momentum distribution. Later on, these generated particles are processed with the help of Geant in the same way as particles from UrQMD generator. By comparing the amount of generated particles against the amount of reconstructed particles, one can define acceptance correction factors for each multidimensional phase space bin. The difference between bins can reach factor $100 - 10000$.

The efficiency correction, applied on top of the acceptance correction, takes into account additional deficits connected to the high track multiplicity environment: this is includes the accuracy of the particle momentum reconstruction in STS, the ring reconstruction in RICH (including misidentifications), and the bremsstrahlung effect. It is known that track reconstruction in the STS detector, as well as electron identification in the RICH detector, are not perfect (efficiency $> 90\%$), hence, the efficiency correction is needed. In order to have proper efficiency correction factors, one needs to provide a data sample with realistic track multiplicity and hit density. Therefore, efficiency corrections are based on an additional sample of UrQMD events.

With this additional sample, one needs to perform a multidimensional analysis first, and then extract the number of reconstructed particles in each phase space bin (p_t vs rapidity). In the second step, one needs to apply acceptance correction on the extracted number of particles. Using Monte Carlo true information, one can get the number of generated particles from a UrQMD sample. The division of the quantity of generated particles by the reconstructed number of particles after acceptance correction gives the efficiency correction factor. The efficiency correction is a relatively small effect ($\sim 0 - 30\%$), in contrast to the acceptance correction (a factor of $\sim 100 - 10000$).

Using conversion analysis it is in principal possible to estimate temperature parameters from the following particles: π^0, η, direct γ. In this thesis, only π^0 and direct γ are considered as candidates for temperature estimation. This is due to the high multiplicity of π^0 per event and the high reconstruction efficiency of single γ. Due to the lack of statistics, one can not perform the same estimation from η mesons, and therefore they will not be discussed here.

8.2 Use of neutral pions for temperature estimation of emitting source

Pions are essential particles in the exploration of a nucleon-nucleon collision. They are emitted in the relatively late stages of the collision after chemical freeze-out, and therefore their analysis can give information about the kinetic freeze-out stage. One of the most important pieces of information from such analyses is the temperature parameter at this stage.

Generally, spectra of charged pions are more suited for this purpose than the spectrum of neutral pions because they are easier to detect. However, the temperature analysis of neutral pions is also feasible. Here, π^0 reconstruction is done using the double conversion method, and therefore high statistics are necessary since the reconstruction efficiency of π^0 with this method is relatively low. In this section only results and tables for the analysis with partial lepton identification within the RICH detector will be presented, since it gives a high efficiency reconstruction with a moderate background. Requiring full identification of all leptons in the RICH severely reduces the event statistics, as discussed in previous chapters and will therefore not presented.

Multidimensional pion analysis

The conversion analysis repeats all seven analysis steps mentioned in Section 6.1 of this thesis with following cuts: $\Theta_{e^+e^-} < 2^\circ$ and $m_{inv}(\mathrm{e^+e^-}) < 20$ MeV/c^2. All π^0 candidates from possible combinations of photons are separated depending on their rapidity and transverse momentum.

The separation in rapidity is in the range $y = 1.2 - 4.0$ with a step value 0.4, and for $p_t = 0.0 - 3.0$ GeV/c with a step value 0.1 GeV/c. For each phase space bin, the combinatorial background is simulated separately with the help of the event mixing technique. The resulting EMT background spectrum for every phase space bin is scaled to its reconstructed spectrum in the range between 0.2 GeV/c^2 and 1.0 GeV/c^2, where only background is present. The remaining peak in each phase space bin after background subtraction is fitted with a Gaussian function.

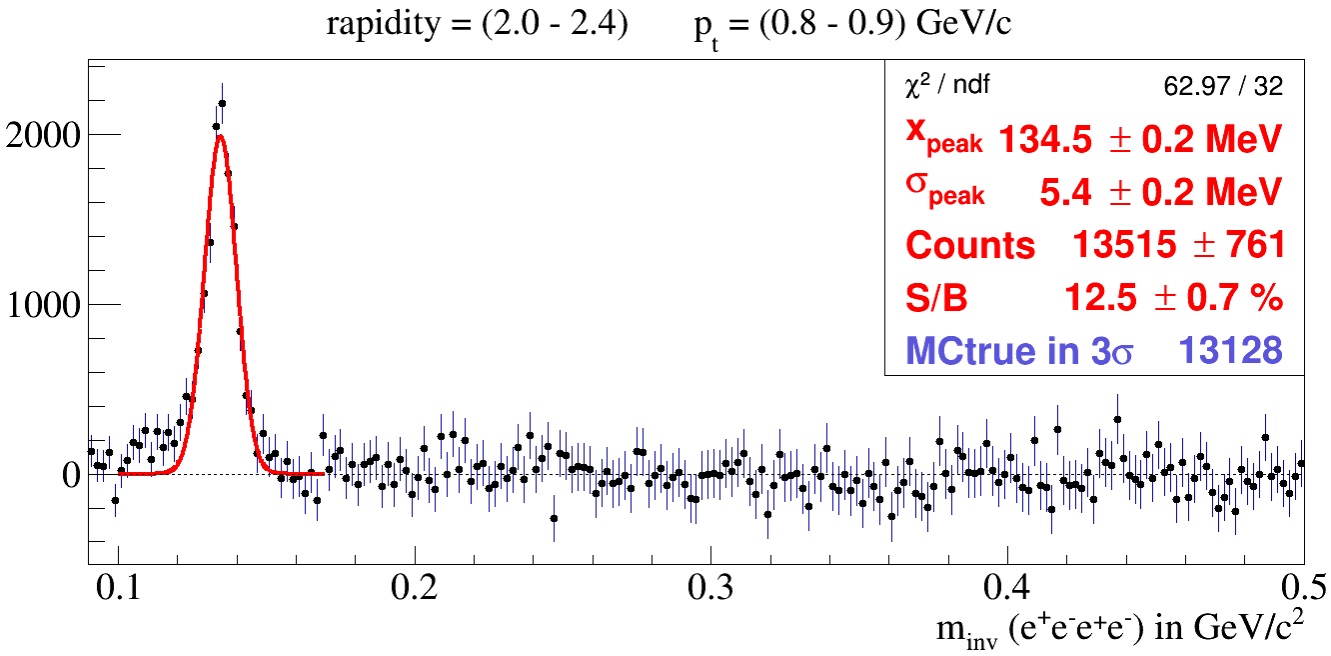

Figure 8.1: Background-subtracted π^0 invariant mass spectrum with cuts on photon candidates $\Theta_{e^+e^-} < 2°$ and $m_{inv}(e^+e^-) < 20$ MeV/c^2 for a case with partial lepton identification within the RICH detector. The spectrum covers one particular phase space bin with rapidity $y = 2.0 - 2.4$ and transverse momentum $p_t = 0.8 - 0.9$ GeV/c.

The results in this subsection are based on 100 million UrQMD events of central Au+Au collisions at a beam energy of 8 AGeV (same as in Section 7.4). In Figure 8.1 one can see an example of the background-subtracted spectrum fitted with a Gaussian function within $y = 2.0 - 2.4$ and $p_t = 0.8 - 0.9$ GeV/c phase space. One can see that points outside the signal region in the background-subtracted spectrum lie around zero, which verifies a good agreement between EMT spectrum and combinatorial background.

The graphical representation of the multidimensional analysis results is shown in Figure 8.2. One can see from Figure 8.2 that the σ parameters for most of the peaks are similar and have a value around 5.5 MeV/c^2. The peak position varies slightly from bin to bin, but overall has a value close to the theoretical value of 134.97 MeV/c^2. One can also notice that the number of reconstructed pions strongly depends on the phase space. Most of reconstructed pions are in the middle of available acceptance. On the other hand, the high momentum bins show relatively big signal to background ratio due to the low amount of background there, although most of these bins have a small number of reconstructed pions. This effect is caused by the magnetic field which deflects very low momenta particles, and therefore leads to a better lepton reconstruction efficiency at high momenta. The lower the momentum of the π^0, the lower the momenta of electrons and positrons from the resulting gamma conversion. Hence, the reconstructability of neutral pions with low transverse momentum is relatively small.

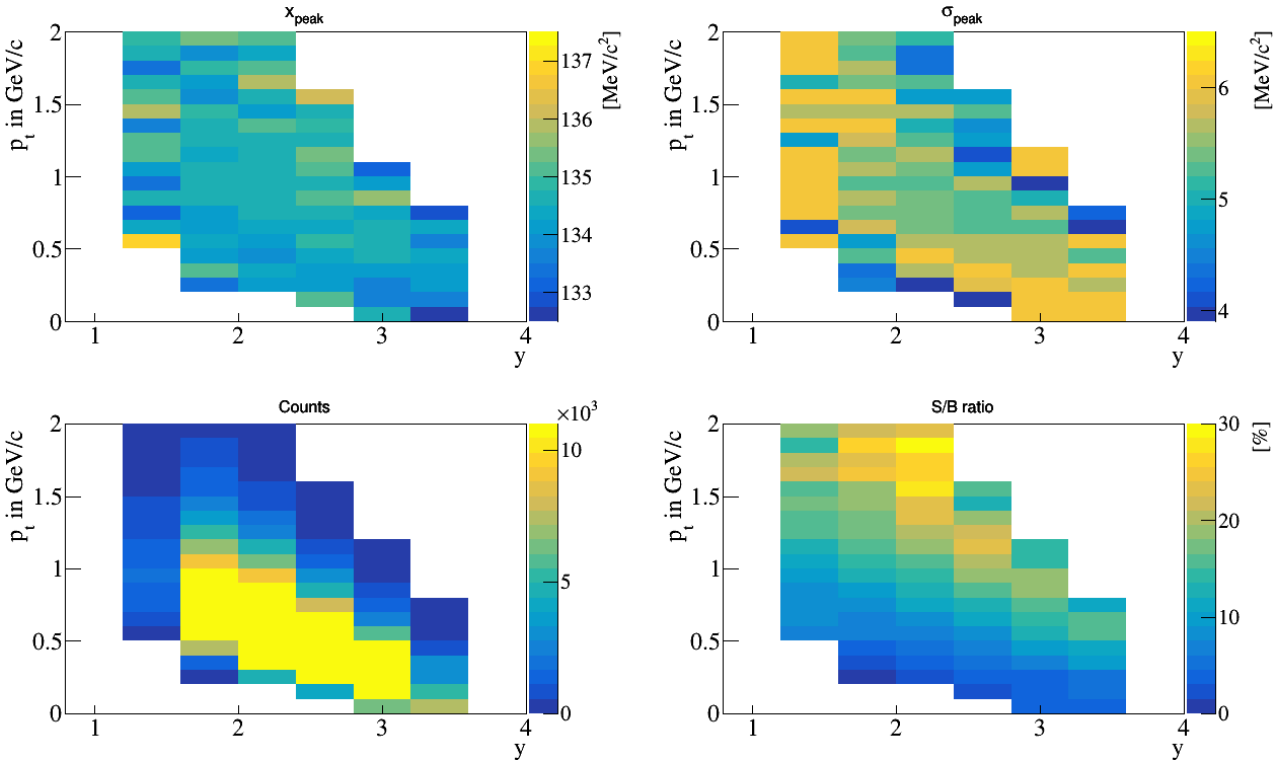

Figure 8.2: Reconstructed observables obtained from multidimensional π^0 analysis: peak position (left-top), σ value (right-top), number of reconstructed π^0 (left-bottom), and π^0 signal to background ratio (right-bottom) for every phase space bin.

Determination of pion acceptance correction

In order to determine the acceptance correction factors, simulation with the box generator is performed using 1 π^0 per event. These pions are distributed homogeneously over the full possible acceptance of the CBM experiment. This simulation provides the proper dependence of conversion probability along their travel direction for all photons from the pion decays. The simulated pions cover an acceptance range of rapidity $y = 0.8 - 4.0$ and transverse momentum $p_t = 0.0 - 2.5$ GeV/c.

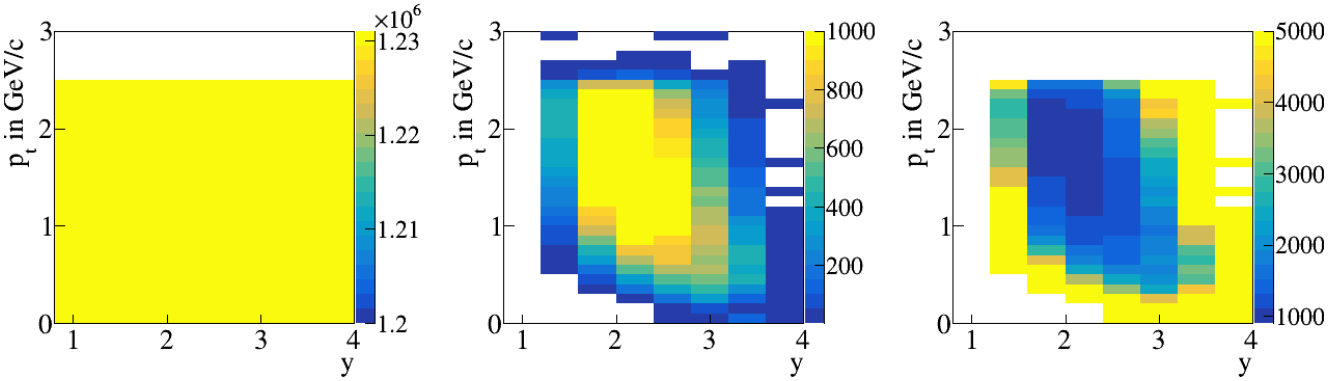

Figure 8.3: Acceptance correction factors (right plot) as function of transverse momentum p_t and rapidity y for the analysis with partial lepton identification approach. Obtained by dividing the number of generated π^0 in the simulated sample (left plot) by the corresponding number of correctly reconstructed π^0 (middle plot).

In Figure 8.3 one can see the number of all generated π^0 (from box generator) and the number of reconstructed π^0 on the left and middle picture correspondingly. The division of these two sets the acceptance correction matrix (right plot in Figure 8.3).

As can be seen from the left picture, the number of simulated pions per bin is $\sim 1.23 * 10^6$. Figure 8.3 shows that only a small amount of the generated pions is reconstructed. The bin with highest number of reconstructed pions has only 1362 π^0 out of 1235876 possible. Therefore, acceptance correction factors for the analysis with current conditions are larger than 1000 within each bin.

Determination of pion efficiency correction

For the efficiency determination, an additional sample of 15 million UrQMD events with central Au+Au collisions at a beam energy of 8 AGeV is simulated. With this sample, one needs to perform a multidimensional analysis first and extract the number of reconstructed pions in each bin. As a second step, one needs to apply acceptance correction factors (determined above) on the extracted number of pions. This corrected number of pions within every bin is already similar to the generated one, but slightly deviates from it. Such a deviation should be compensated for by the use of the efficiency correction.

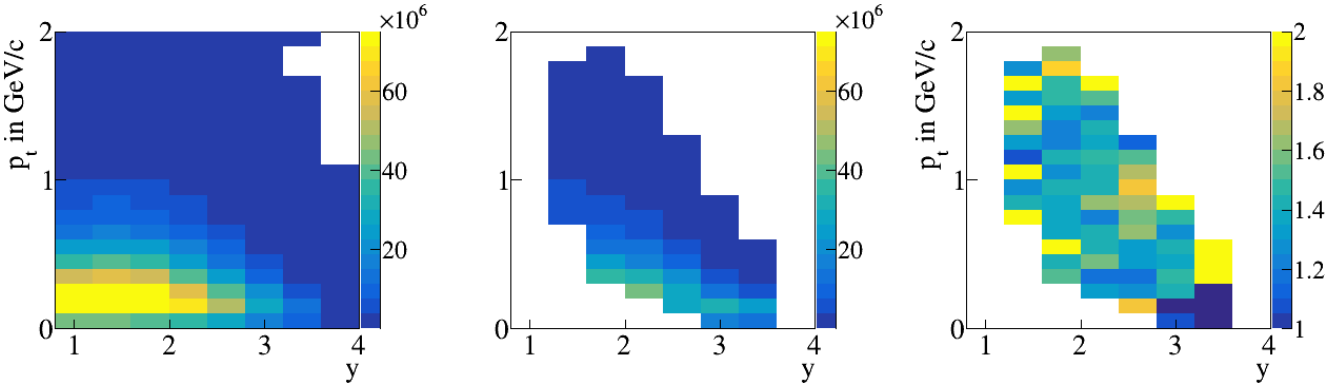

Figure 8.4: Efficiency correction factors (right plot) as function of transverse momentum p_t and rapidity y for the analysis with partial lepton identification approach. Obtained by dividing the corresponding number of correctly reconstructed π^0 after acceptance correction (middle plot) by generated π^0 in the simulated sample (left plot).

In Figure 8.4 one can see the number of all generated π^0 (left plot) within 15 million UrQMD sample and number of reconstructed pions after the acceptance correction (middle plot). By dividing number of all generated π^0 by number of pions after acceptance correction, one obtains the efficiency correction factors (right plot in Figure 8.4). Here, a efficiency correction factor equal to one would mean that no additional efficiency correction is needed. As can be seen from Figure 8.4, most of the efficiency correction factors have the value around 1.4, which shows the effect of high track density environment on reconstruction procedure.

The errors for the acceptance and efficiency correction factors are calculated with normal error propagation. Errors on acceptance and efficiency correction factors are not shown in this thesis, but are always applied in all further steps.

Temperature estimation from pions

Once one has determined the efficiency and acceptance matrices, one can start the temperature estimation from reconstructed particles. The results in this subsection are based on 100 million UrQMD events of central Au+Au collisions at a beam energy of 8 AGeV (the same sample as in Section 7.4). The resulting number of pions from the multidimensional analysis is shown in Figure 8.2 without corrections and indicate only the reconstructed pions within each bin of the phase space. These numbers must be corrected first using both: acceptance (coefficients from Figure 8.3) and efficiency (coefficients from Figure 8.4) corrections. It can be done via simple multiplication:

$$N_{out} = N_{reco} * F_{acc} * F_{eff}, \tag{8.1}$$

where N_{reco} is number of reconstructed pions within certain phase space bin, F_{acc} is acceptance correction factor for the same bin, F_{eff} is efficiency correction factor for this bin, and N_{out} is an estimated number of produced pions. Ideally, this number should be the same as the number of generated pions from MCtrue information N_{mc}.

In order to estimate the temperature parameter of reconstructed particles one needs to use Formula 2.3, mentioned in Section 2.3. This formula can be used for different particles by varying parameter m_0 (the particle mass). For π^0, this parameter is $m_0 = 134.97$ MeV/c^2. The fitting Formula 2.3 can be applied only to 1-D spectra, and therefore an integration over rapidity is needed. After integration of all rapidity bins for a fix p_t, the resulting transverse momentum spectrum can be fit and the resulting slope parameter can be extracted. The resulting temperature value, the so-called "output" (or T_{reco}) slope parameter, should now be compared to the "input" (or T_{mc}) slope parameter. If these two parameters are close to each other in the range of errors, then this proves the accuracy of both correction matrices since they are applied on statistically independent data samples.

The comparison requires the T_{mc} temperature, and therefore MCtrue data is used. To have a proper comparison, one needs to take pions from the same phase space covered by detector acceptance used for T_{reco} estimation. In other words, if for a certain bin $N_{reco} = 0$, then the MCtrue events from this phase space bin should not be used for the temperature estimation. After the integration over rapidity, the resulting transverse momentum spectrum can be fit with Formula 2.3 and the resulting true temperature can be extracted (T_{mc}).

The two resulting 1-D spectra with their fits can be seen in Figure 8.5. The obtained slope parameters are shown in the legend of the figure. For the reconstructed temperature using double conversion method is $T_{reco} = 188.8 \pm 4.5$ MeV and Monte Carlo true temperature for the same phase space is $T_{mc} = 189.6 \pm 3.2$ MeV. A good agreement between two values in the range of errors can be seen, which proves internal consistency of the approach using separate acceptance and efficiency corrections.

As additional consistency test, one needs to compare directly MC data points with reconstructed data, since the small difference between two spectra can not be seen by eye in Figure 8.5 due to logarithmic scale of Y-axis. For this purpose, the division of both spectra is done. If two samples would be the same the resulting value after division would be for all points = 1. the division of MC data (full circles in Figure 8.5) by the reconstructed data (empty circles in Figure 8.5) with relevant errors is shown in Figure 8.6. The dotted black line in Figure shows the place of theoretical perfect agreement between two spectra. Most of points in the graph are located around value 1 and deviate from it by around ± 10 %. Overall, all point are well compatible with 1 within errors, what also shows a good agreement between two spectra. The more detailed analysis of corresponding errors shows, that main contribution comes from the low statistics in some bins during the multidimensional π^0 reconstruction. The precision might be increased by increasing

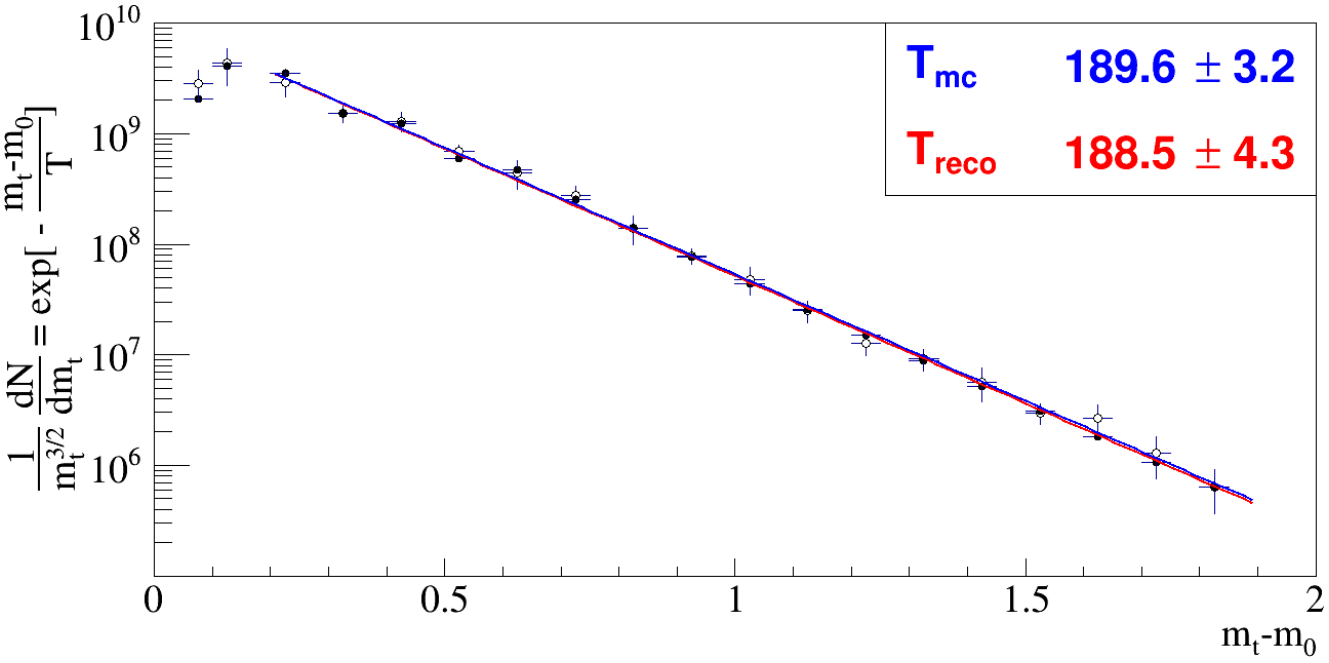

Figure 8.5: Amount of generated π^0 within the CBM acceptance obtained from MCtrue data bank (full circles) and from reconstructed pions after applying efficiency and acceptance corrections (empty circles). The blue and red lines show correspondingly a fit of full and empty circles using Formula 2.3.

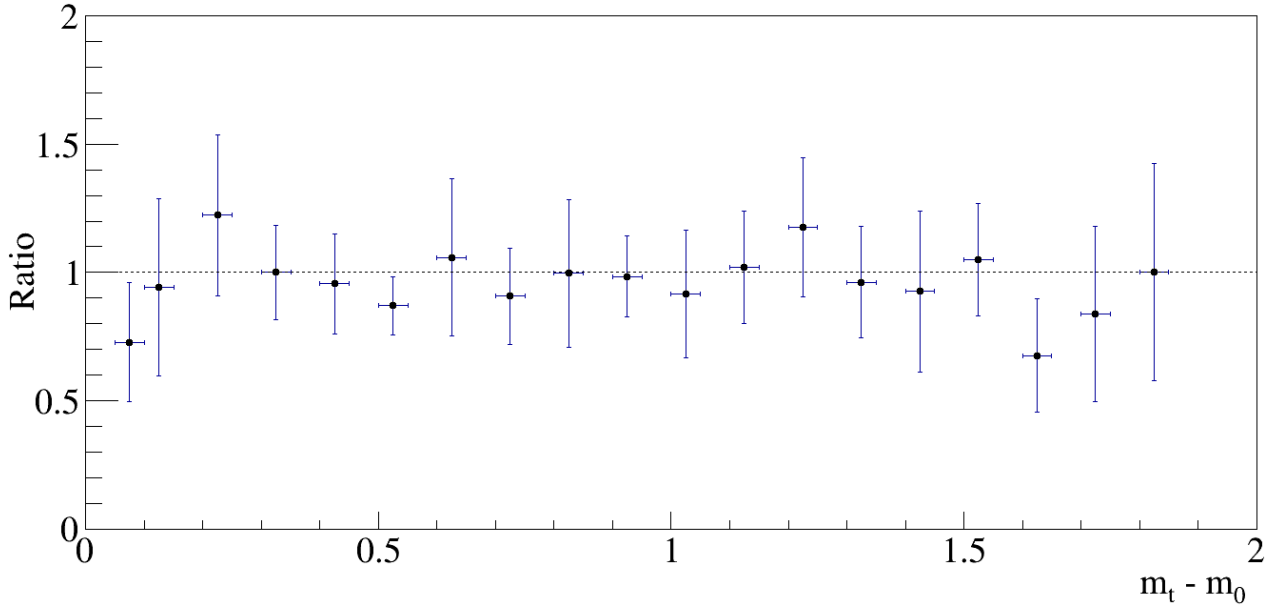

Figure 8.6: Ratio between all generated π^0 taken from MCtrue data bank, and all generated π^0 estimated from reconstructed data via double conversion method after efficiency and acceptance corrections.

the bin step in transverse momentum (i.e. instead of 0.1 GeV/c use for example 0.4 GeV/c) or increase number of simulated events.

However, in order to use the π^0 spectrum after acceptance and efficiency corrections for the estimation of freeze-out temperature, one needs to test the approach with other event generators, which produce a simulated data according to a different temperature slope, in order to check

model dependence of the approach. Such test for π^0 reconstruction has not been done in this thesis.

8.3 Temperature estimation from reconstruction of direct photons

Measurements of *direct* photons are particularly important, since these photons are produced at the earliest stage of the collision. The difficulty of *direct* photon analysis lies in the inability to distinguish between *direct* photons and *decay* photons experimentally since one measures a time-integrated snapshot of particles from all sources. In the current analysis, all photons not originating from hadron decays are derived as *direct* photons.

When analyzing *direct* photons, the main result is normally represented in terms of transverse momentum instead of invariant mass (as is the case for π^0 and η), since all photons by definition have no mass. Such a p_t spectrum is called an "inclusive photon spectrum".

Theoretical predictions show that *direct* photons from Au+Au collision at CBM energies should have transverse momenta in the range from 0 GeV/c to 3 GeV/c. At the same time, photons with momenta up to 3 GeV/c also come from decays of π^0 and η mesons as well as from ρ, ω, a_1 decays. There are no cuts which could help to distinguish *direct* photons from *decay* photons on event-by-event basis. Therefore, the only way to get the *direct* photon yield from the experimental data at CBM is to subtract the contribution of photons from meson decays from the inclusive photon spectrum in order to extract the remaining contributions. Because of this, the temperature analysis for *direct* photons differs slightly from the pion analysis (or any other particle with mass) and consists of the following steps:

1. The reconstruction procedure for the photon spectrum consists of analysis steps 1-6 described in Section 6.1.

2. For each photon candidate, p_t and y are calculated and, depending on rapidity and transverse momentum values, every photon candidate is placed into the 1-D p_t histogram after applying the corresponding acceptance correction factors.

3. The all background p_t spectra coming from decay photons are normalized and subtracted, leaving only the 1-dimensional p_t spectrum of *direct* photons.

4. The 1-D p_t spectrum from previous step is corrected using the 1-D efficiency correction factors as function of p_t.

5. The spectrum after the efficiency correction is fit with Formula 2.3 and the slope parameter is extracted.

A more detailed description of these steps is given below.

The analysis presented here is based on partial lepton identification within the RICH detector. The cases with full identification and without identification were also considered, but their detailed analysis will not be discussed here, however, the final table in this section includes results for all three different lepton identification cases. Since there is no distinctive difference between *decay* photons and *direct* photons, the following cuts are used in order to reconstruct photon candidates: $\Theta_{e^+e^-} < 1^\circ$ and $m_{inv}(e^+e^-) < 10$ MeV/c^2. Stricter cuts as compared to those previously used are chosen in order to reduce the combinatorial background as much as possible due to the relatively weak signal.

Source of direct photons in simulation

The studies presented here are based on nucleon-nucleon collisions simulated using the UrQMD event generator. Therefore as a first step, all possible photon sources implemented in UrQMD were studied. This information was obtained using only MCtrue information of produced particles from MCTrack array. In UrQMD only photons from decays of π^0, η mesons are included. This means, that UrQMD does not generate some particles such as ρ, ω as well as *direct* photons.

The CbmRoot framework is able to work with two different generators at the same time. To have a realistic simulation, one can use the above mentioned UrQMD as a background generator and embed additional individual photons following a thermal photon distribution. The advantage of this method is that the user can control all parameters of the embedded photon spectrum. The p_t distribution of embedded photons is modeled according to Formula 2.3. The theoretical predictions for CBM energies give the number of expected direct photons to be about ~ 5 photons per central Au+Au collision, therefore, this number was chosen in simulations.

The generated thermal spectrum has 5 million events with following parameters (see Figure 8.7): 5 photons per event, temperature of the emitted source $T = 400$ MeV, range of transverse momentum is $p_t = 0.0 - 4.0$ GeV/c, rapidity range is $y =$ -2.0 $-$ 5.0, and photons are boosted according to a fixed target experiment with a beam energy $E = 8$ AGeV for central Au+Au collisions. In the following text, photons generated within thermal spectrum will be called "*direct* photons".

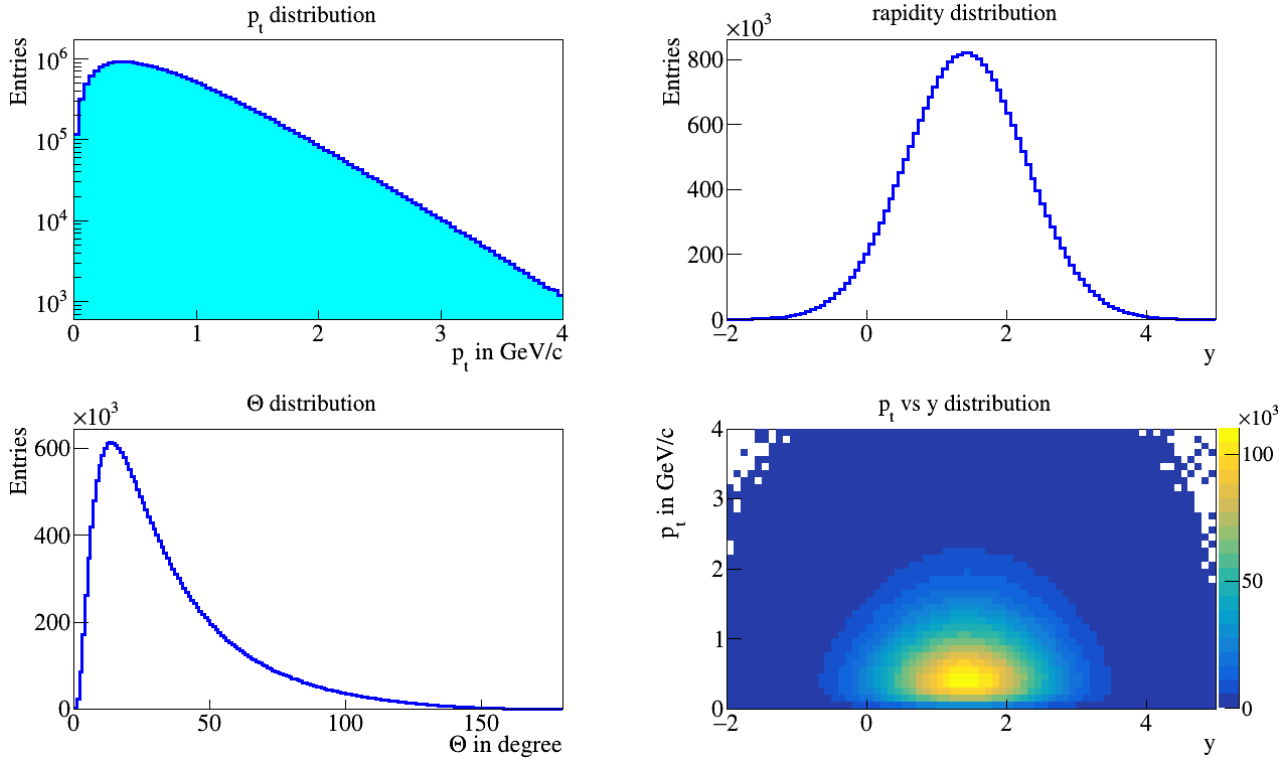

Figure 8.7: Parameter distributions of modeled photons embedded into the simulated data sample as *direct* photons.

The generated transverse momentum spectrum of such photons has an exponential shape, but the extracted temperature parameter is not physical, because the value was chosen artificially. Here, in a similar way to the with neutral pions case, T_{reco} and T_{mc} will be compared in order to prove feasibility of the applied method.

Inclusive photon spectrum

The resulting spectrum after the conversion analysis of photons is shown in Figure 8.8 with blue. This spectrum has many different contributions apart from *direct* photons. With the help of MCtrue data, one can pick out every contribution separately. In Figure 8.8, different contributions are shown with different colors: the green dashed line shows *direct* photons, in magenta photons from $\pi^0 \to \gamma + \gamma$ and $\pi^0 \to e^+ + e^- + \gamma$ decay channels are shown, black are imaginary photons ($\gamma^* \to e^+ + e^-$) from Dalitz decay channel $\pi^0/\eta \to e^+ + e^- + \gamma$, the solid green line are photons from two η decay channels $\eta \to \gamma + \gamma$ and $\eta \to \pi^+ + \pi^- + \gamma$, red is the combinatorial background, and light blue is the combination of $\pi^+\pi^-$ (one pion misidentified as electron within the RICH and second pion is outside the RICH acceptance, both pions come from nucleon-nucleon collision).

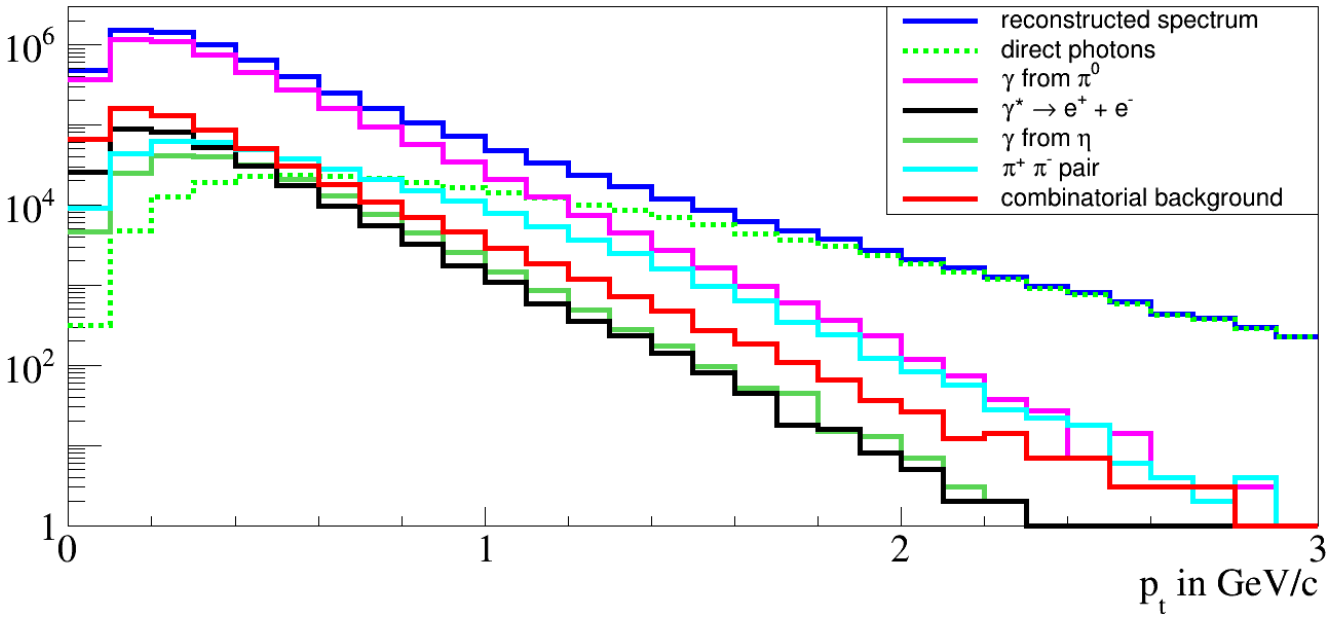

Figure 8.8: Decomposition of various different contributions to the inclusive photon spectrum based on the analysis using partial lepton identification approach with cuts $\Theta_{e^+e^-} < 1^\circ$ and $m_{inv}(e^+e^-) < 10$ MeV/c^2.

As can be seen from the list above, the biggest sources of photons is the π^0 channel, which gives $\sim$ 73 % of all background. The second biggest contribution ($\sim$ 9 %) comes from wrong combinations of e^+ and e^- which stem from different mother particles (combinatorial background). Almost the same fraction ($\sim$ 6 %) corresponds to misidentified combinations of $\pi^+\pi^-$. Slightly more than $\sim$ 5 % in the final spectrum come from decays of imaginary photons, mostly from π^0. Photons from η make another $\sim$ 3 % contribution to the final photon spectrum. Only the remaining $\sim$ 3 % belong to the source of events of interest: *direct* photons.

As can be seen from Figure 8.8, all background contributions have the same p_t range and similar spectral shapes as the *direct* photon spectrum of interest. Therefore, there is no way to use additional cuts to extract only the *direct* photon spectrum.

Determination of decay photon contributions

By considering the current 5 million UrQMD simulation sample with embedded thermal photon spectrum as a "reference sample", one can define the shape of each background contribution and use this information as reference. One assumes here, that the statistics are large enough to produce

spectra almost free of statistical deviations. Now, if one would have another sample of data, one would need to only normalize these background contributions and subtract them from new the resulting photon spectrum. The question is: "how to do the normalization?".

One can define the contribution from π^0 as a standard and then define the deposit of all other contributions as a percentage of the π^0 background contribution. Because the number of produced neutral pions in nucleon-nucleon collision is well defined, one can make a normalization based on the number of reconstructed π^0. The idea is to compare the amount of reconstructed pions from two samples under the same reconstruction conditions. If the number of reconstructed pions in the "working data sample", for example, is 10 times bigger than in "reference sample", then all background contributions from the reference sample should be normalized by the same factor of 10. Later on, one can subtract these scaled background contributions from the final reconstructed spectrum and presumably receive only spectrum of reconstructed direct photons at the end.

Determination of photon acceptance correction

In order to determine acceptance correction factors for photons, the simulation with the box generator is performed using 1 γ per event. These photons are distributed homogeneously over the range of rapidity $y = 0.8 - 4.0$ and transverse momentum $p_t = 0.0 - 2.5$ GeV/c.

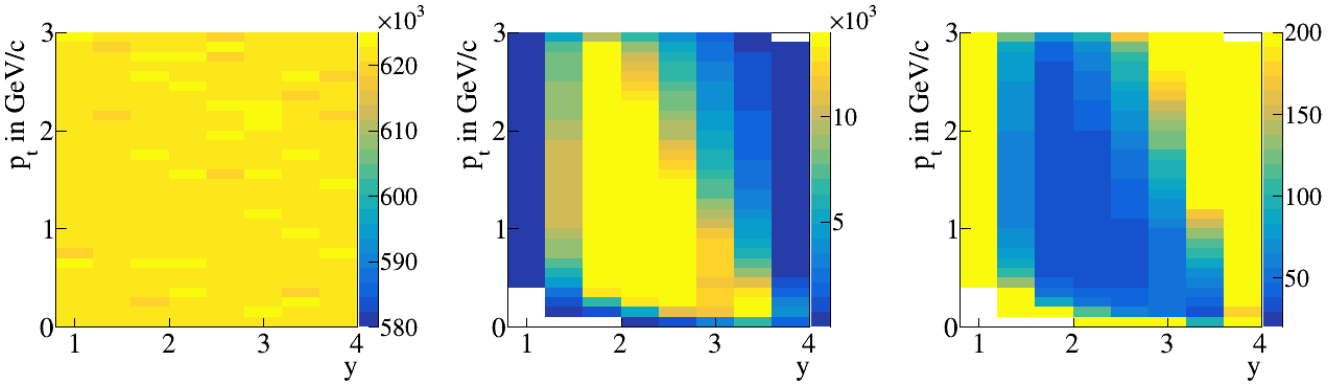

Figure 8.9: Acceptance correction factors (right plot) as function of transverse momentum p_t and rapidity y for the analysis with partial identification approach. Obtained by dividing generated γ in the simulated sample (left plot) by the corresponding number of correctly reconstructed γ (middle plot).

In Figure 8.9, one can see the number of all generated photons for the acceptance correction (left plot), and the number of reconstructed photons (middle plot), as well as the acceptance correction matrix (right plot) gained by the division of these two.

During the acceptance determination, about $6.2 * 10^5$ photons per bin were generated. The highest number of reconstructed photons within one bin is 14035 for $p_t = 1.0 - 1.1$ GeV/c and $y = 1.6 - 2.0$, corresponding to ~ 2.2 % of the photon reconstruction efficiency.

These 2-D acceptance correction factors are used as weight factors in the photon reconstruction analysis during the filling of the 1-D inclusive photon spectrum. This is done in order to have a higher accuracy in the final results, and hence, to have smaller errors.

Determination of photon efficiency correction

The efficiency determination for direct photons can be done in similar way to what was done for neutral pions. First, one needs to simulate first an additional sample with 5 million UrQMD

events including individually added thermal photons following a p_t distribution corresponding to $T = 400$ MeV. Then one needs to run the full reconstruction chain, apply acceptance corrections, subtract normalized background contributions from decay photons mentioned in Figure 8.8, and then compare the obtained results with generated spectra of direct photons obtained from MCtrue data bank. Unlike for π^0, the corrections for γ can be done only in terms of p_t (i.e. 1 dimensional) because the decay contributions are defined only in terms of p_t. One might define them in terms of y and p_t as well, but that would lead to huge uncertainties due to requirement of much larger statistics.

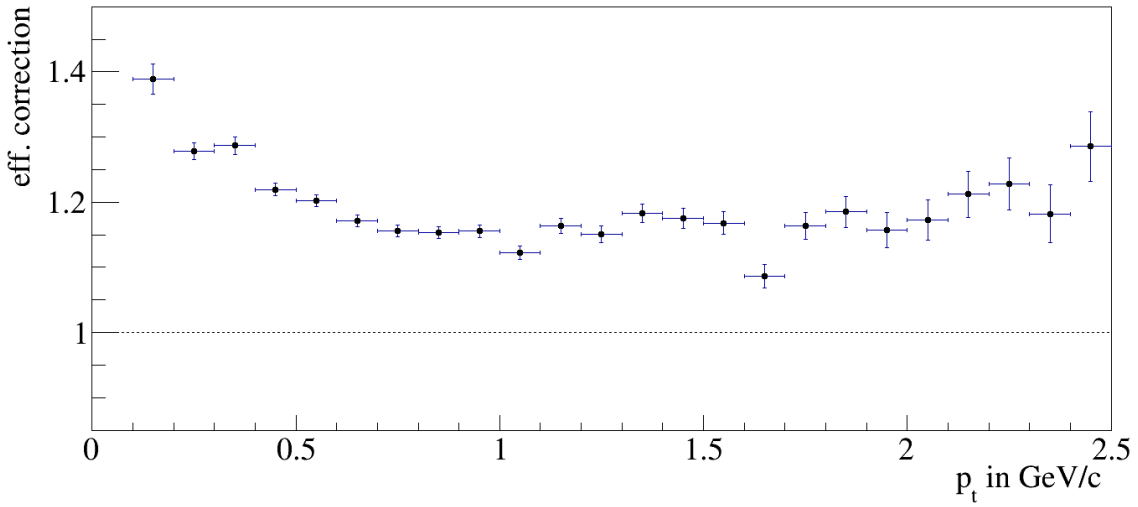

Figure 8.10: Efficiency correction factors as function of transverse momentum p_t for direct photon reconstruction.

The result of the efficiency correction factors as dependence from transverse momentum can be seen in Figure 8.10. The Figure shows that the efficiency factors for direct photons are mostly on the level of 1.2 (i.e. 20 %). This number is much smaller than the correction factors for π^0 due to the requirement of only one photon to be reconstructed instead of two photons to form pions as previously discussed.

Temperature estimation from photons

Having all the information at hand, one can perform the temperature determination from the *direct* photon spectrum. The analysis will be performed using a statistically independent second sample of 5 million simulated events from UrQMD generator. The main concern in the reconstruction of *direct* photons is that the analysis will be model dependent. In order to test for model dependence, the newly generated thermal photon spectrum is produced according to a different source temperature, $T = 240$ MeV, while keeping all other parameters the same as before.

The results of the complete analysis procedure are shown in Figure 8.11 for the three different lepton identification approaches. Obtained results can be also found in Table 8.1.

case	two: $\gamma \rightarrow (e^{\mp} + e^{\pm})$	onetwo: $\gamma \rightarrow (e^{\mp} + ?^{\pm})$	all: $\gamma \rightarrow (?^{\mp} + ?^{\pm})$
T_{mc} in MeV	269.8 ± 0.2	294.5 ± 0.2	295.8 ± 0.2
T_{reco} in MeV	258.9 ± 5.0	286.9 ± 4.2	289.8 ± 5.1

Table 8.1: Temperature results from direct photons analysis using three different cases of lepton identification (full, partial, without).

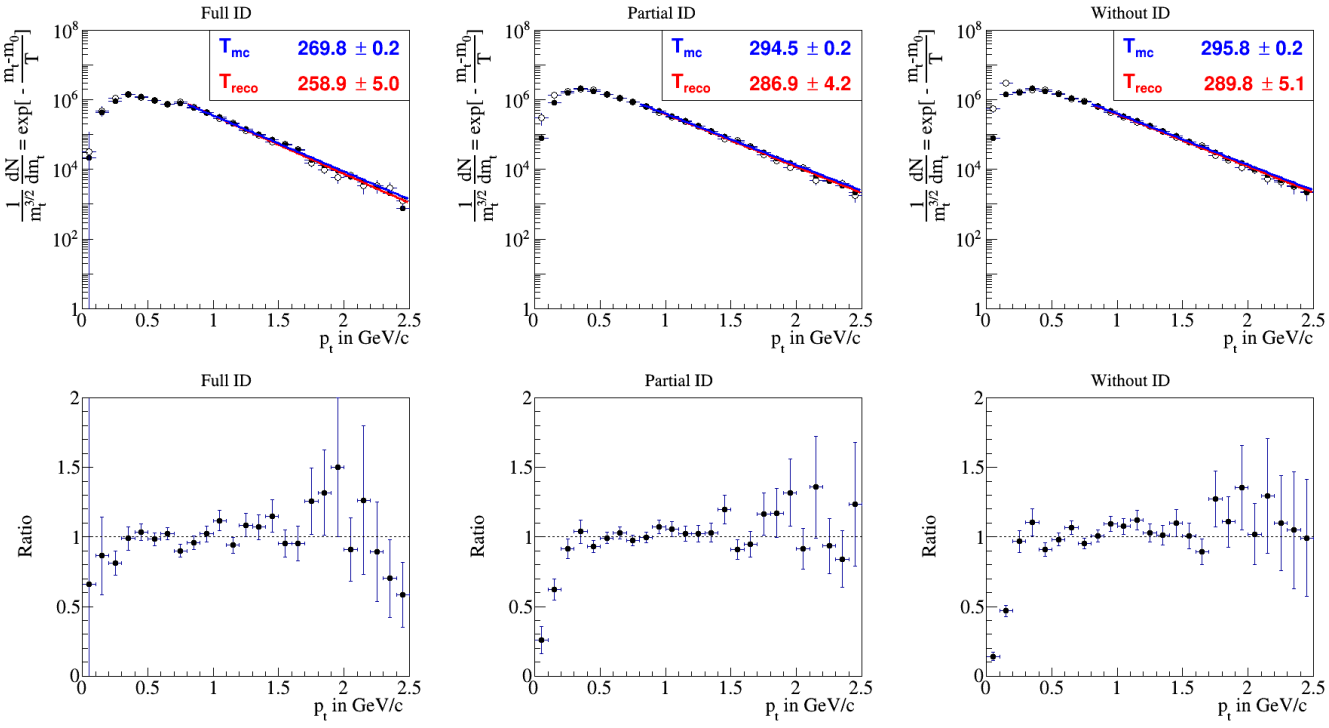

Figure 8.11: The amount of generated direct γ within the CBM acceptance obtained from MCtrue data bank (full circles) and from full reconstruction applying efficiency and acceptance corrections (empty circles) using three lepton identification approaches: full (first column), partial (second column), and without (third column). The second row shows the ratio between MCtrue and reconstructed distributions. The blue and red lines show a fit of the full and empty circles with Formula 2.3.

As one can see from Figure 8.11, the MCtrue spectrum (full circles) is in good agreement with the reconstructed spectrum after acceptance and efficiency corrections (empty circles) for all three lepton identification approaches. As a result, the extracted slope parameters are also quite close one to each other. In Table 8.1 one can notice a difference in MCtrue slope parameters between the three approaches. The reason for that is the slightly different acceptance range for every analysis case.

The obtained slope parameters from the reconstruction and the MCtrue data, for example from the partial lepton identification analysis, are: $T_{reco} = 286.9 \pm 4.2$ MeV and $T_{mc} = 294.5 \pm 0.2$ MeV. These values are slightly higher than the value used in the generator for modeling the Monte Carlo sample ($T = 240$ MeV). The limited acceptance of the CBM experiment reduces the possibility of obtaining the temperature slope parameter after the reconstruction to only photons with $p_t = 0.0 - 3.0$ GeV/c and $y = 0.8 - 4.0$. On the other hand, as can be seen from Figure 8.7, in the thermal photon generator, the acceptance coverage is $p_t = 0.0 - 4.0$ GeV/c and $y = $ -2.0 $- 5.0$. One can not compensate for region outside the detector acceptance, and therefore the reconstructed slope parameter differs from the expected slope parameter from the generator.

In spite of the above arguments, the conversion analysis including acceptance and efficiency corrections shows the ability to reconstruct the slope parameter from the reconstructed *direct* photon spectrum within the available acceptance of the experiment. The obtained results for the temperature parameter of MCtrue data and reconstructed data are in good agreement if one considers the same acceptance range.

8.4 Summary

In this chapter, the possibility of applying the reconstruction of photons via conversion in order to extract the effective temperature of the emitting source was investigated. This is strongly depends on the reconstruction efficiency of each particle. For this purpose, π^0 meson and *direct* γ were considered as possible candidates. The third possible candidate, the η meson, was not considered since its analysis would require very large statistics. The two analyzed particles are produced at different collision stages, and therefore provide different temperature information. However, all generators used for the simulations do not provide realistic temperature momentum distributions, and therefore, only the internal consistency of the approach has been investigated in this thesis.

In general, the approach is based on a multidimensional particle analysis using acceptance and efficiency corrections in order to obtain the number of generated particles after conversion reconstruction analysis. The obtained p_t-dependent particle yield is then used for temperature estimation, and is compared to the MCtrue temperature in the same acceptance region.

There is a small difference in the approach for π^0 and *direct* γ reconstructions due to the absence of mass in the photon case. The comparison between slope parameters obtained from reconstruction and MCtrue data shows good agreement for both particles.

Due to the requirement of two photons being converted for π^0 and only one photon for *direct* γ analysis, the reconstruction efficiency of pions is about 100 times smaller. Therefore, π^0 analysis requires a much larger data sample. Here, different central Au+Au data samples were used for each analysis: 100 million events for π^0 and 5 million events for *direct* γ. The obtained results have shown that within such samples the accuracy of the temperature estimation from π^0 and *direct* γ correspondingly is about 2 % when taking into account only statistical errors. The systematical error of the analysis has not been studied.

The model dependency of the approach has been considered only in application to *direct* γ. The dependency has been checked using two different *direct* γ momentum distributions produced with different temperature slope parameters. The obtained results did not show any model dependency of the approach so far.

As a final conclusion, it can be stated that these studies showed a successful application of the conversion method for the temperature estimation based on π^0 and γ particles within realistic UrQMD simulations for the CBM setup.

Summary and outlook

In the first part of this work, a new geometry layout for the PMT plane of the CBM-RICH detector has been developed, motivated by the need for additional space for electronic modules behind the MAPMT photon sensors. The optimization procedure of the photon detector mechanical design has shown that a cylindrical geometry of the PMT camera is the preferable geometry in the context of technical realization for the future CBM experiment. A new approach has been applied in order to derive the effective 3-dimensional contour of the RICH focal plane, and based on these simulations, the design has been optimized in terms of the geometrical parameters: radius, tilting angle, and position of the cylindrical camera.

In order to prove good performance of this new geometry configuration, a direct comparison between default wing-shaped and new cylindrical geometry was done. The comparison was performed using the simulation of signal events coming from dilepton channels of $\omega \rightarrow e^+ + e^-$ and $\rho \rightarrow e^+ + e^-$, as well as simulations of main background sources for dilepton reconstruction, mainly $\pi^0 \rightarrow \gamma + \gamma$ and $\pi^0 \rightarrow e^+ + e^- + \gamma$. The studies revealed, that the new cylindrical geometry of the PMT-plane using the RICH detector shows slightly better performance for the physics analysis, and its layout allows to have enough space in order to accommodate the readout electronics. The new RICH geometry was implemented into the simulation framework (CbmRoot) of the CBM experiment.

In the second part, the conversion method for the reconstruction of π^0 and η mesons using the new geometry layout has been studied. A full reconstruction chain based on conversion has been developed, which includes conversion happening inside the detector material, as well as in the target. The reconstruction of conversion outside the target material is managed with the help of a secondary vertex finder implemented in KFParticle package. Particle reconstruction has been considered using different lepton identification approaches in the RICH detector, where, for example, only 2 out of 4 leptons are identified in the RICH detector and 2 other particles have only tracks in STS. The cut values applied in the reconstruction have been optimized with respect to reconstruction efficiency and signal to background ratio.

The conversion analysis studies showed the ability of the CBM experiment to reconstruct π^0 via decay channels $\pi^0 \rightarrow \gamma + \gamma$ and $\pi^0 \rightarrow e^+ + e^- + \gamma$, where photons are reconstructed after their conversion within the target or in the detector material of MVD/STS. Different possible cut values were considered for each of the three identification approaches. The conversion studies revealed that reconstruction analysis with requirement of only partial lepton identification in the RICH detector provides high pion reconstruction efficiency with moderate background. Therefore, such approach is highly recommended to use for the pion estimation from the experimental data in future.

Different decay channels of η were tested on their possibility to be reconstructed using conversion method. The studies showed that in the CBM experiment it is possible to reconstruct η using nothing but information from MVD/STS/RICH detectors only via $\eta \rightarrow \gamma + \gamma/\gamma^*$ decay channel. Other decay channels have very small signal to background ratios. In order to see a peak

of η meson from the double conversion method in CBM, one needs to have relatively big amount of data. It is hard to store such big samples of simulated events necessary for the analysis due to the limited disk storage space, therefore two alternative methods to handle simulation were developed. Both methods have different advantages and disadvantages, which were discussed in details.

In the third part, the possibility to use the conversion method for the estimation of an effective temperature of the emitting source has been investigated. The detailed analysis procedure including multidimensional reconstruction, and determination of acceptance and efficiency corrections has been demonstrated. Two different probes has been investigated for temperature estimation: π^0 and *direct* photons.

The multidimensional reconstruction of the π^0 using conversion method was performed in terms of transverse momentum and rapidity in order to see to what extend the reconstruction parameters like π^0 invariant mass peak width, signal to background ratio, or peak position are depending on the phase space. Results showed that the main π^0 peak parameters during the multidimensional analysis stay unchanged for all phase space bins. The main difference during the multidimensional reconstruction was observed in signal to background ratio and in reconstruction efficiency. Studies revealed that regions with high transverse momentum of pions have a bigger signal to background ratio than low momentum regions. The extracted information about number of reconstructed pions from the multidimensional analysis was used for the temperature estimation of the emitting source. It was found, that conversion analysis of π^0 is well suited for the temperature estimation of the emitting source in the CBM experiment using large statistics data samples.

Direct photons are the most attractive probe in the conversion analysis, since it requires only one photon to be converted in the material. On the other hand, this is also the more complicated analysis, because there are no cuts to distinguish *direct* photons from *decay* photons. Here the first attempts to reconstruct a *direct* photon spectrum were done. Taking into account the main sources of *decay* photons (π^0 and η mesons) a *direct* photon spectrum could be reconstructed. Other sources of *decay* photons were not considered since they are not implemented in the UrQMD generator. With help of acceptance and efficiency corrections the inverse slope parameter from this reconstructed spectrum was extracted and compared to the MCtrue one. The results show that conversion analysis in CBM is suitable to reconstruct a *direct* photon spectrum and derive a slope parameter for temperature estimation.

Outlook

The double conversion analysis of π^0 and η mesons show good results from the simulation of central Au+Au collisions at a beam energy of 8 AGeV. In order to have a full picture about particle reconstruction it is necessary to perform similar analysis for the full range of energies available in the CBM experiment at heavy ion synchrotron SIS100. The use of the TRD detector might additionally decrease combinatorial background during the conversion analysis and improve reconstruction.

The conversion analysis showed that the reconstruction of the direct photon slope parameter is feasible. To have more realistic expectations one needs to perform the analysis including additional photon sources apart from π^0 and η. There are several interesting particle decays, which should be considered in future direct photon analysis: 1) $\Delta \rightarrow N + \gamma$, 2) $\omega \rightarrow \pi^0 + \gamma$, 3) $\Sigma^0 \rightarrow \Lambda^0 + \gamma$. Also the use of TRD detector might be helpful in order to exclude high momentum pions coming directly from the primary heavy ion collision.

Some additional particles, for example $\omega \rightarrow \pi^0 + \gamma$, can be reconstructed using conversion

as well. Such decay might be hard to reconstruct only with MVD+STS+RICH detector setup due to low conversion probability. Therefore, as additional tool one can consider to use the electromagnetic calorimeter (ECAL) in order to perform a combined study of photons via direct + indirect measurements.

Bibliography

[1] M. Gell-Mann, "A Schematic Model of Baryons and Mesons", *Phys. Lett., Vol. 8, pp. 214-215* (1964).
https://doi.org/10.1016/S0031-9163(64)92001-3

[2] T. Morii, et al., "The physics of the standard model and beyond" (2004).
https://doi.org/10.1142/4655

[3] M. Tanabashi et al., "Review of Particle Physics", *Phys. Rev. D 98, 030001* (2018).
https://doi.org/10.1103/PhysRevD.98.030001

[4] R. Stock, "Relativistic nucleusnucleus collisions: from the BEVALAC to RHIC", *J. Phys. G: Nucl. Part. Phys. 30 S633* (2004).
https://doi.org/10.1088/0954-3899/30/8/001

[5] G. Agakishiev et al., "Measurement of charged pions in $C^{12} + C^{12}$ collisions at 1 AGeV and 2 AGeV with HADES", *Eur. Phys. J. A, pp. 40-45* (2009).
https://doi.org/10.1140/epja/i2008-10746-7

[6] The Relativistic Heavy Ion Collider complex.
https://www.bnl.gov/rhic/complex.asp

[7] The Large Hadron Collider.
https://home.cern/topics/large-hadron-collider

[8] I.C. Arsene et al., "Dynamical phase trajectories for relativistic nuclear collisions", *Phys. Rev. C75 24902* (2007).
https://doi.org/10.1103/PhysRevC.75.034902

[9] Facility for Antiproton and Ion Research in Europe.
https://fair-center.eu/public.html

[10] FAIR physics programm.
https://fair-center.eu/for-users/experiments.html

[11] FAIR Baseline Technical Report.
https://fair-center.eu/fileadmin/fair/publications_FAIR/FAIR_BTR_1.pdf

[12] B. Friman et al., "The CBM physics book: Compressed baryonic matter in laboratory experiments", *Lect. Notes Phys. Vol. 814* (2011).
https://doi.org/10.1007/978-3-642-13293-3

[13] S. Mrówczyński, "Quark-gluon plasma", *arxiv* (1999).
https://arxiv.org/abs/nucl-th/9905005

[14] Johann Rafelski, "Melting Hadrons, Boiling Quarks - From Hagedorn Temperature to Ultra-Relativistic Heavy-Ion Collisions at CERN" (2016).
https://doi.org/10.1007/978-3-319-17545-4_33

[15] Z. Fodor, S. D. Katz, "Critical point of QCD at finite T and μ, lattice results for physical quark masses", *Journal of High Energy Physics, JHEP04* (2004).
https://doi.org/10.1088/1126-6708/2004/04/050

[16] J. Randrup and J. Cleymans, "Exploring high-density baryonic matter: Maximum freeze-out density" *Eur. Phys. J. A, pp. 52-218* (2016).
https://doi.org/10.1140/epja/i2016-16218-7

[17] I. Montvay and G. Münster, "Quantum Fields on a Lattice", *Cambridge, pp. 231-317* (1997).
https://doi.org/10.1017/CBO9780511470783

[18] R. Rapp and H. van Hees, "Thermal dileptons as fireball thermometer and chronometer", *Phys. Lett. B 753, pp. 586-590* (2016).
https://doi.org/10.1016/j.physletb.2015.12.065

[19] P. Hohler and R. Rapp, "Is ρ-meson melting compatible with chiral restoration?", *Phys. Lett. B 731, pp. 103-109* (2014).
https://doi.org/10.1016/j.physletb.2014.02.021

[20] T. Ablyazimov et al., "Challenges in QCD matter physics - The scientific programme of the Compressed Baryonic Matter experiment at FAIR", *Eur. Phys. J. A., pp. 53-60* (2017).
https://doi.org/10.1140/epja/i2017-12248-y

[21] T. Matsui and H. Satz, "J/ψ suppression by quark-gluon plasma formation", *Phys. Lett. B 178, pp. 416-422* (1986).
https://doi.org/10.1016/0370-2693(86)91404-8

[22] Sourav Sarkar et al., "The Physics of the Quark-Gluon Plasma", (2010).
https://doi.org/10.1007/978-3-642-02286-9

[23] R. Bjorklund et al., "High Energy Photons from Proton-Nucleon Collisions", *Phys. Rev. 77, pp. 213* (1950).
https://doi.org/10.1103/PhysRev.77.213

[24] A. Pevsner et al., "Evidence for a three-pion resonance near 550 MeV", *Phys. Rev. Lett. 7, 421-423* (1961).
https://doi.org/10.1103/PhysRevLett.7.421

[25] P. L. Bastien et al., "Decay Modes and Width of the η Meson", *Phys. Rev. Lett. 8, 114* (1962).
https://doi.org/10.1103/PhysRevLett.8.114

[26] B. M. K. Nefkens and J. W. Price, "The Neutral Decay Modes of the Eta-Meson", *Physica Scripta. T99, pp. 114-122* (2002).
https://doi.org/10.1238/Physica.Topical.099a00114

[27] E. Shabalin, "Decays of η and η' Mesons Caused by the Weak", *Physica Scripta. T99, pp. 104-108* (2002).
https://doi.org/10.1238/Physica.Topical.099a00104

[28] J. Kapusta et al., "High-energy photons from quark-gluon plasma versus hot hadronic gas", *Phys. Rev. D 44, 2774 pp. 229-237* (1991).
https://doi.org/10.1103/PhysRevD.44.2774

[29] S. A. Bass et al., "Photon Interferometry of Au+Au Collisions at the BNL Relativistic Heavy-Ion Collider", *Phys. Rev. Lett. 93, 162301, pp. 259-260* (2004).
https://doi.org/10.1103/PhysRevLett.93.162301

[30] R. Chatterjee et al., "Elliptic Flow of Thermal Photons in Relativistic Nuclear Collisions", *Phys. Rev. Lett. 96, 202302, pp. 250-251* (2006).
https://doi.org/10.1103/PhysRevLett.96.202302

[31] R. Chatterjee and D. K. Srivastava, "Elliptic flow of thermal photons and formation time of quark gluon plasma at energies available at the BNL Relativistic Heavy Ion Collider (RHIC)", *Phys. Rev. C 79, 021901, pp. 220* (2009).
https://doi.org/10.1103/PhysRevC.79.021901

[32] K. Geiger, "Thermalization in ultrarelativistic nuclear collisions. I. Parton kinetics and quark-gluon plasma formation", *Phys. Rev. D 46, 4965* (1992).
https://doi.org/10.1103/PhysRevD.46.4965

[33] J. Bartke, "Introduction to Relativistic Heavy Ion Physics.", (2008).
https://doi.org/10.1142/1881

[34] I. G. Bearden et al. (The NA44 Collaboration), "Collective Expansion in High Energy Heavy Ion Collisions", *Phys. Rev. Lett. 78, 2080* (1997).
https://doi.org/10.1103/PhysRevLett.78.2080

[35] E. Schnedermann et al, "Thermal phenomenology of hadrons from 200A GeV S+S collisions", *Phys. Rev. C 48, 2462* (1993).
https://doi.org/10.1103/PhysRevC.48.2462

[36] T. Peitzmann, "Direct photon production in high-energy nuclear collisions", *AIP Conference Proceedings, Vol. 1701, 060016* (2016).
https://doi.org/10.1063/1.4938679

[37] A. Andronic, P. Braun-Munzinger, J. Stachel, "Hadron production in central nucleus-nucleus collisions at chemical freeze-out", *Nucl. Phys. A 772, pp. 167-199* (2006).
https://doi.org/10.1016/j.nuclphysa.2006.03.012

[38] C. Gale et al, "Event-by-event anisotropic flow in heavy-ion collisions from combined Yang-Mills and viscous fluid dynamics", *Phys. Rev. Lett. 110, 012302* (2013).
https://doi.org/10.1103/PhysRevLett.110.012302

[39] The Compressed Baryonic Matter Experiment.
https://fair-center.eu/for-users/experiments/nuclear-matter-physics/cbm/introduction.html

[40] "Technical Design Report for CBM - Superconducting Dipole Magnet".
http://repository.gsi.de/record/109025/files/CBM_magnet_TDR_31_10_2013-nc.pdf?version=1

[41] Micro Vertex Detector in the CBM experiment.
https://fair-center.eu/for-users/experiments/nuclear-matter-physics/cbm/projects/mvd.html

[42] P. Klaus, P. Sitzmann, M. Deveaux, J. Stroth, "Update on the CBM MVD Geometry", *CBM Progress Report 2017, pp. 135.*
http://repository.gsi.de/record/209729/files/CBMProgressReport2017.pdf?version=2

[43] "Technical Design Report for CBM - Silicon Tracking System (STS)".
http://repository.gsi.de/record/54798/files/GSI-Report-2013-4.pdf?version=2

[44] "Technical Design Report for CBM - Ring Imaging Cherenkov (RICH) Detector".
http://repository.gsi.de/record/65526/files/TDR-CBM-RICH.pdf?version=1

[45] "Technical Design Report for CBM - Muon Chambers (MuCh)".
http://repository.gsi.de/record/161297/files/much-tdr-final-for-gsi-report.pdf?version=1

[46] "Technical Design Report for CBM - Transition Radiation Detector (TRD)".
https://indico.gsi.de/event/5516/contribution/4/material/0/0.pdf

[47] "Technical Design Report for CBM - Time-ofoFlight System (TOF)".
http://repository.gsi.de/record/109024/files/tof-tdr-final_rev6036.pdf?version=1

[48] I. Korolko et al, "The CBM ECAL", *J. Phys.: Conf. Ser. 798 012164* (2017).
https://doi.org/10.1088/1742-6596/798/1/012164

[49] "Technical Design Report for the CBM experiment - Projectile spectator detector (PSD)".
http://repository.gsi.de/record/109059/files/20150720_CBM_TDR_PSD.pdf?version=1

[50] Supercomputer for FAIR.
https://fair-center.de/de/news-events/news-view/article/kooperation-von-fias-goethe-uni-und-gsi-auf-platz-1-der-green500.html

[51] P. A. Cherenkov, "Visible light from clear liquids under the action of gamma radiation", *C.R. (DokI.) Acad. Sci. URSS 2 451* (1934).

[52] I. Frank and I. Tamm, "Coherent Visible Radiation of Fast Electrons Passing Through Matter", *C.R. Ac. Sd. USSR. 14, 109* (1937).

[53] Yuri Ryabov, "CBM RICH mechanical design". Talk given on the 27th CBM collaboration meeting in Darmstadt (2016).
https://indico.gsi.de/event/3620/session/12/contribution/100/material/slides/1.pdf

[54] C. Pauly, "Status electronics development", Talk given on the 27th CBM collaboration meeting in Darmstadt (2016).
https://indico.gsi.de/event/3620/session/12/contribution/92/material/slides/0.pdf

[55] G. Battistoni et al., "The FLUKA code: description and benchmarking", *In: AIP Conf. Proc. 896, pp. 31-49* (2007).
https://doi.org/10.1063/1.2720455

[56] "GEANT Detector Description and Simulation Tool", CERN, Geneva (1993).
http://www.phys.sinica.edu.tw/~spring8/Documentation/CERN/GEANT.pdf

[57] I. Froehlich et al., "Design of the Pluto Event Generator", *J. Phys. Conf. Ser. Volume 219, Part 3* (2010).
https://doi.org/10.1088/1742-6596/219/3/032039

[58] FairRoot official homepage.
https://fairroot.gsi.de

[59] Rene Bruns and Fons Rademakers, "ROOT - An Object Oriented Data Analysis Framework", *Nucl. Inst. & Meth. in Phys. Res. A 389, pp. 81-86* (1997).
https://doi.org/10.1016/S0168-9002(97)00048-X

[60] M. Bleicher et al., "Relativistic hadron-hadron collisions in the ultra-relativistic quantum molecular dynamics model", *J. Phys. G: Nucl. Part. Phys. 25 1859* (1999).
https://doi.org/10.1088/0954-3899/25/9/308

[61] M. Zyzak, "Online selection of short-lived particles on many-core computer architectures in the CBM experiment at FAIR", Frankfurt am Main (2015).
http://publikationen.ub.uni-frankfurt.de/frontdoor/index/index/year/2016/docId/41428

[62] R. E. Kalman, "A new approach to linear filtering and prediction problems", *J. Basic Eng 82(1), pp. 35-45* (1960).
https://doi.org/10.1115/1.3662552

[63] R. Frühwirth, "Application of Kalman filtering to track and vertex fitting", *Nucl. Instrum. Meth. A 262, pp. 444-450* (1987).
https://doi.org/10.1016/0168-9002(87)90887-4

[64] Liliana Teodorescu, "Artificial neural networks in high-energy physics", *CERN, Geneva, Switzerland, pp.13-22* (2005).
https://doi.org/10.5170/CERN-2008-002.13

[65] Sankar K. Pal and Sushmita Mitra, "Multilayer Perceptron, Fuzzy Sets, and Classification", *IEEE Transactions on neutral networks, vol. 3, No. 5, pp. 683-697* (1992).
https://doi.org/10.1109/72.159058

[66] Melanie Klein-Bösing, "Development of a Transition Radiation Detector and Reconstruction of Photon Conversions in the CBM Experiment", *PhD thesis* (2009).
https://www.uni-muenster.de/imperia/md/content/physik_kp/agwessels/thesis_db/ag_wessels/klein-boesing_m_2009_dissertation.pdf

[67] Sascha Reinecke, "Characterisation of photon sensors for the CBM-RICH and its use for the reconstruction of neutral mesons via conversion", *PhD thesis* (2016).
http://elpub.bib.uni-wuppertal.de/servlets/DocumentServlet?id=6421&lang=en

[68] D. Drijard et al., "Study of event mixing and and its application to the extraction of resonance signals", *Nucl. Instrum. and Methods 225, pp. 367-377* (1984).
https://doi.org/10.1016/0167-5087(84)90275-8

[69] Y.-S. Tsai, "Pair production and bremsstrahlung of charged leptons", *Rev. Mod. Phys. 46, pp. 815* (1974).
https://doi.org/10.1103/RevModPhys.46.815

Acknowledgments

Finally, upon reaching this turning point of my life, I would like to thank all people who in one or another contributed to the presented work.

My utmost gratitude goes to Prof. Dr. Karl-Heinz Kampert who gave me the opportunity to be a part of his working group. I will never forget your call via Skype to inform me that I was chosen among all other candidates to perform physics analysis for the CBM experiment at University of Wuppertal. I remember how you supported me even before I got my PhD position. Many thanks to you also for your supervision during my stay in Wuppertal and for your support in writing this thesis.

I would like to give many thanks to Prof. Dr. Claudia Höhne for her interesting questions during our regular CBM-RICH meetings. Your useful hints helped to solve many incomprehensible problems which occurred during my studies. Also I would like to thank you for reviewing this thesis.

I would like to give Dr. Christian Pauly my huge gratitude for his enormous help in my studies. I am very thankful for his answering my endless questions, especially when they were extraordinary hard. Thank you for the regular motivation and support during last years, as well as for providing corrections for this thesis.

My gratitude also to Prof. Dr. Francesco Knechtli and Prof. Dr. Frank Goldenbaum for being part in my PhD committee.

Many thanks to my office colleagues Dr. Sascha Reinecke, Jörg Förtsch, Dennis Pfeifer, and Vivek Patel for the pleasant working atmosphere, your help in solving work-related questions, as well as for the various non-work-related discussions.

Furthermore I am thankful to:

- Prof. Dr. Tetyana Galatyuk for leading me in the right direction and for her support in dilepton studies during my study.
- Dr. Maksym Zyzak for his help in understanding of KFParticle package.
- Dr. Semen Lebedev for his help with the CbmRoot framework.
- Dr. Tariq Mahmoud and Dr. Egor Ovcharenko for your help and discussions related to the RICH geometry optimization.
- A big thanks go also to Ingrid Schaarwächter for helping me with the huge amount of administrative questions which arose during my first months in Germany.

Thanks to all my colleagues from the CBM collaboration and from the astroparticle physics group in Wuppertal. It was my pleasure to work with all of you.

Finally, many thanks to my parents for their support during the whole of my life.

My deep gratitude to my wife, Olena Kres, for your love and understanding every time, even when I was not around because of work.

Declaration of Authorship

English

I hereby declare that the thesis submitted is my own unaided work. All direct or indirect sources used are acknowledged as references.

This thesis was not previously presented to another examination board and has not been published.

Deutsch

Hiermit versichere ich, die vorliegende Arbeit selbstständig und unter ausschließlicher Verwendung der angegebenen Literatur und Hilfsmittel erstellt zu haben.

Die Arbeit wurde bisher in gleicher oder ähnlicher Form keiner anderen Prüfungsbehörde vorgelegt und auch nicht veröffentlicht.

Wuppertal, den _____ _____

(Ievgenii Kres)